UNIVERSITÀ DEGLI STUDI DI PADOVA

Università degli Studi di Padova
University College Dublin

# Thin films for soft X-ray optics: deposition, characterisation, optical and spectroscopic testing techniques

*Author:*
Antonela COMISSO

*Supervisors:*
Prof. Piergiorgio NICOLOSI
Prof. Gerry O'SULLIVAN
Dr. Fergal O'REILLY

*A thesis submitted in partial fulfilment of the requirements for the degree of Doctor of Philosophy in the*

Dipartamento di Ingenieria dell'Informazione (DEI), UNIPD Padova
UCD School of Physics College of Science, UCD Dublin

May, 2017

Sede Amministrativa: Università degli Studi di Padova.

Dipartimento di Ingegneria dell'Informazione Faculty of Mathematics, Computer Science and Natural Sciences.

SCUOLA DI DOTTORATO DI RICERCA IN: Ingegneria dell'Informazione
INDIRIZZO: Scienza e tecnologia dell'Informazione
CICLO: XXIX
TESI IN COTUTELA

# Thin films for soft x-ray optics: deposition, characterisation, optical and spectrosopic testing techniques

**Direttore della Scuola:** Ch.mo Prof. Matteo Bertocco
**Coordinatore d'indirizzo:** Ch.mo Prof. Carlo Ferrari
**Supervisore:** Ch.mo Prof. Piergiorgio Nicolosi
**Supervisore**: Ch.mo. Prof. Gerry O´Sullivan
**Supervisore**: Ch.mo. Dr. Fergal O´Reilly

**Dottoranda** : ANTONELA COMISSO

# Declaration of authorship

I, Antonela COMISSO, declare that this thesis titled," Thin films for soft X-ray optics: deposition, characterisation, optical and spectroscopic testing techniques." and the work presented in it are my own. I confirm that:

- This work was done wholly while in candidature for a joint PhD degree at Università degli studi di Padova (UNIPD) and University College Dublin (UCD).
- All e-beam depositions were performed by Antonela Comisso at LUXOR laboratory of the "Istituto di Fotonica e Nanotecnologie" (CNR-IFN).
- The materials analysis was performed in collaboration with Francesca Gerlin and Fengyuan Zhang (AFM), Laura Calvillo and Gaetano Granozzi (Chemical composition analysis) and Laura Brigo (Spectroscopic ellipsometry).
- The synchrotron measurements at ELETTRA were performed in collaboration with Marco Nardello and Angelo Giglia.
- The spectral reflectometer was designed and built by Niall Kennedy and tested and improved by Antonela Comisso.

# List of publications and conference presentations

## Publications

1. **A. Comisso**, M. Nardello, A. Giglia, P. Nicolosi, “Optical constants of e-beam evaporated titanium dioxide thin films in the 25.5- to 612-eV energy region”, Opt. Eng. 55(9),095102 (Sept. 2016)
2. **A. Comisso**, A. Giglia, M. Nardello, E. Tessarolo, L. Calvillo, M. G. Sertsu, G. Granozzi, F. Gerlin, L. Brigo, P. Nicolosi, "Characterization of TiO2 thin films in the EUV and soft X-ray region", Proc. SPIE 9510, EUV and X-ray Optics: Synergy between Laboratory and Space IV, 95100Z (May 12, 2015)
3. M. G. Sertsu, A. Giglia, S. Brose, **A. Comisso**, Z. S. Wang, L. Juschkin and P. Nicolosi "Optical and structural characterization of CeO2/B4C multilayers near the Boron absorption edge ", Proc. SPIE 9510, EUV and X-ray Optics: Synergy between Laboratory and Space IV, 95100T (May 12, 2015).

## Presentations at conferences

1. "Multilayer structure analysis based on EUV reflectivity measurements". COST Action Meeting: MP1203. Athens, Greece. Sept. 2016 - **Poster presentation**.
2. "Optical constants of $TiO_2$ thin films in the EUV and soft X-ray region. EXTATIC Welcome Week Workshop. Southampton (UK). January 2016 - **Oral presentation**.
3. "Characterization of $TiO_2$ thin films in the EUV and sof x-ray region". 5-6 November 2015,VUV and EUV Metrology seminars, PTB, Berlin, Germany - **Poster presentation**.
4. "Characterization of $TiO_2$ thin films in the EUV and soft X-ray region. SPIE Conference. Optics + Optoelectronics 2015. Prague (Cz. Rp). April 2015 - **Poster presentation**.
5. "$TiO_2$ thin films and novel $TiO_2$/Sc multilayers for the EUV and Soft X-ray region." EXTATIC Welcome Week Workshop. Warsaw (Poland). October 20th to 24th, 2014 - **Oral presentation**.

# *Abstract*


Dipartamento di Ingenieria dell'Informazione (DEI), UNIPD Padova
UCD School of Physics College of Science, UCD Dublin


Doctor of Philosophy

**Thin films for soft X-ray optics: deposition, characterisation, optical and spectroscopic testing techniques**


by Antonela COMISSO



This thesis deals with the deposition, characterisation and optical study of thin films coatings designed for Extreme Ultraviolet (EUV) and soft X-ray optics. Single and multilayer thin films are important both for scientific and industrial purposes, developing knowledge of optical properties of materials in the EUV and soft X-rays plays a major role in determining performances of optical elements used in this spectral range.
The optical constants of titanium dioxide ($TiO_2$) have been experimentally determined at energies in the extreme ultraviolet and soft X-ray spectral regions, from 25.5 to 612 eV (2 to 48.6 nm), measuring angle-dependent reflectance of amorphous $TiO_2$ thin films with synchrotron radiation at the BEAR beamline of Synchrotron ELETTRA. The experimental reflectance profiles were fitted to the Fresnel equations using a genetic algorithm applied to a least-square curve fitting method, obtaining values for $\delta$ and $\beta$. We compared our measurements with tabulated data. All samples were grown on Si (100) substrates by the electron-beam evaporation technique, with a substrate temperature of 150$^o$C and deposition rates of 0.3 to 0.5 Å/s. Complete films characterisation has been carried out with structural (XRD, ellipsometry, and profilometry), compositional (X-ray photoelectron spectroscopy), and morphological (atomic force microscopy) analyses. The reflectance performed at near edge energies is very sensitive to interlayers formation on the interfaces. A study of buried interlayers formed due to the growth process was carried on based on the optical response near the soft X-ray absorption edge of $TiO_2$.
The thesis also deals with the test and improvement of a table-top spectral reflectometer used as a thin film characterisation technique. The reflectometer is intended to be simple, relatively low cost and to provide reasonably fast and accurate reflectance measurements. Several bilayer samples were produced to test the reflectometer. The materials composing the samples were Cr, Ti, $TiO_2$ and Sc, chosen based on their relevance in the soft X-ray and EUV applications and their absorption edges accessible to the reflectometer. Chemical composition, depth probe and spatial scanning studies were performed on the samples.

Questa tesi presenta lo studio delle proprietà ottiche, la deposizione e la caratterizzazione di rivestimenti a film sottile per ottiche operanti nell' Estremo Ultravioletto (EUV) e nei raggi X Soffici. Film sottili a singolo e multi strato sono interessanti per applicazioni sia scientifiche che industriali, lo studio delle proprietà ottiche dei materiali nel EUV e nei raggi X soffici è fondamentale per determinare le prestazioni degli elementi ottici utilizzati in queste regioni spettrali. Le costanti ottiche del biossido di titanio ($TiO_2$) sono state determinate sperimentalmente nelle regioni EUV e raggi X soffici da 25.5 a 612 eV (2-48.6 nm) misurando la riflessione di film sottili di $TiO_2$ amorfo in funzione dell'angolo di incidenza con radiazione di sincrotrone presso la linea di luce BEAR del sincrotrone ELETTRA Trieste. I profili di riflettività sperimentali sono stati riprodotti approssimandoli utilizzando le equazioni di Fresnel ed un algoritmo genetico applicato a procedure di approssimazione ai minimi quadrati, in questo modo si sono derivati i valori delle costanti ottiche $\delta$ e $\beta$. I risultati sperimentali sono stati confrontati con i valori riportati in letteratura. Tutti i campioni sono stati depositati su wafer di Si (100) con la tecnica di evaporazione a fascio elettronico, il substrato è stato tenuto ad una temperatura di 150C e la velocità di deposizione è stata di 0.3 - 0.5 Å/s. La caratterizzazione strutturale dei film è stata fatta con tecniche XRD, ellissometriche e profilometriche, quella composizionale con spettroscopia X di fotoelettroni, e l'analisi morfologica con microscopia a forza atomica. Le misure in riflessione condotte ad energie prossime agli 'edge' di assorbimento sono molto sensibili alla formazione di 'interlayers' alle interfacce fra gli strati. Lo studio di 'interlayers' sommersi nella struttura del film dovuti al processo di crescita è stato condotto sulla base della risposta ottica in prossimità del 'edge' di assorbimento nei raggi X soffici del $TiO_2$.
Nella tesi si presenta anche il test ed il perfezionamento di un riflettometro spettrale compatto da laboratorio utilizzato per la caratterizzazione di film sottili. Il concetto del riflettometro è tale da costituire uno strumento semplice, di costo relativamente contenuto, capace di effettuare misure di riflettività accurate in tempi ragionevoli. Diversi campioni di film con struttura a doppio strato sono stati realizzati con i seguenti materiali: Cr, Ti, $TiO_2$ and Sc, per il test dello strumento. I materiali sono stati selezionati sulla base della loro significatività per applicazioni nelle regioni spettrali citate e per avere 'edge' di assorbimento nelle regioni operative del riflettometro. Sui campioni si sono condotti studi relativi alla composizione chimica, ed in scansione spaziale ed in profondità.

# *Acknowledgements*

Firstly, I would like to thank my supervisors Prof. Piergiorgio Nicolosi and Prof. Gerry O'Sullivan for their knowledge, guidance and advice during my PhD time. Also a special and huge thank to Dr. Fergal O'Reilly for his co-supervision of great part of this work, fruitful discussions and for restoring my interest in many moments of "PhD despair".
I would like to gratefully acknowledge the members and organizers of the EXTATIC program, thank you for accepting me as a PhD student. The funding that made this work possible by the Education, Audiovisual, and Culture Executive Agency Erasmus Mundus Joint Doctorate Programme "EXTATIC" under Framework Partnership Agreement No. 2012—0033.
Thank you to all the staff at the CNR-IFN Padova, DEI. Special thanks to Cristina Capuzzo, Stefania Schiavon, Enrico Soncin. Thank you to the Segreteria Didattica DEI staff of the PhD school, with special thanks to Alessandra Calore and Sara Fedel. I am also grateful for the constant support and help offered by the UCD School of Physics during my stage in Dublin. Special thanks to Bairbre Fox, John Brennan and Sarah McEvoy.
I want to acknowledge the important and indispensable work of the UCD School of Physics mechanical workshop team, Frank Heffernan, Enda Scally, Jose Lopez Escobar and Richie.
Thank you to all the great people I met in Padova and UCD during these years, with whom I shared not only interesting moments of research but also fun talks, coffee/tea and lunch breaks. Cheers to Mewael Sertsu, Marco Nardello, Francesca Gerlin, Enrico Tessarolo, Carmela, Dom, Niall, Oisin, Elgiva, Gladson, Taka and John.
Special thank you to Dr. Angelo Giglia from ELETTRA Synchrotron for the training and help with the reflectance measurements.
Last but not least, thanks to all my friends from back home for staying in touch and keeping it real even with a literal ocean between us. Gracias a Lala, Nani y Lucas, my always supportive family. And to Potati San, for all the love and moments shared on foreign lands.

# Contents


**Declaration of authorship** iii

**List of Publications** v

**Abstract** vii

**Acknowledgements** ix

**1 Introduction** 1

**2 Theoretical considerations** 7

2.1 Interaction of light with matter . . . . . . . . . . . . . . . . . . . . . . 7

2.2 Reflection and transmission of a multilayer structure . . . . . . . . . . . 10

2.2.1 Fresnel equations . . . . . . . . . . . . . . . . . . . . . . . . . . . 11

2.2.2 Reflection and transmission of a single layer . . . . . . . . . . . . 13

2.2.3 Reflectance and transmittance of a multilayer structure . . . . . . 14

**3 Thin film deposition** 17

3.1 Introduction . . . . . . . . . . . . . . . . . . . . . . . . . . . . . . . . . 17

3.2 Electron beam evaporation . . . . . . . . . . . . . . . . . . . . . . . . . 18

3.2.1 Deposition geometry . . . . . . . . . . . . . . . . . . . . . . . . . 20

3.2.2 Film thickness uniformity . . . . . . . . . . . . . . . . . . . . . . 22

3.3 The e-beam deposition system . . . . . . . . . . . . . . . . . . . . . . . 24

3.4 Sample preparation . . . . . . . . . . . . . . . . . . . . . . . . . . . . . 26

3.4.1 Substrates . . . . . . . . . . . . . . . . . . . . . . . . . . . . . . . 26

3.4.2 Titanium dioxide samples . . . . . . . . . . . . . . . . . . . . . . 27

3.4.3 Bilayer samples . . . . . . . . . . . . . . . . . . . . . . . . . . . . 28

**4 Thin films characterisation: instruments and methods** 31

4.1 Introduction . . . . . . . . . . . . . . . . . . . . . . . . . . . . . . . . . 31

4.2 Film thickness . . . . . . . . . . . . . . . . . . . . . . . . . . . . . . . . 32

4.2.1 Quartz Crystal Microbalance (QCM) . . . . . . . . . . . . . . . . 32

4.2.2 Profilometer . . . . . . . . . . . . . . . . . . . . . . . . . . . . . . 33

4.2.3 Spectral Ellipsometry . . . . . . . . . . . . . . . . . . . . . . . . . 34

4.3 Atomic Force Microscopy (AFM) . . . . . . . . . . . . . . . . . . . . . . 35

4.4 X-ray Photoelectron Spectroscopy (XPS) . . . . . . . . . . . . . . . . . . 37

4.5 Soft X-rays and Extreme Ultraviolet (EUV) reflectance . . . . . . . . . . 38

**5 Synchrotron reflectance measurements, $TiO_2$ optical constants determination and complementary film characterisation. 41**
5.1 Introduction . . . . . . . . 41
5.2 Sample characterisation . . . . . . . . 42
5.2.1 Thickness, surface roughness and structure. . . . . . . . . 42
5.2.2 Chemical composition . . . . . . . . 44
5.3 Reflectance measurements at BEAR . . . . . . . . 46
5.3.1 Instrument and specifications . . . . . . . . 46
5.4 Optical constants calculation . . . . . . . . 49
5.5 Results and discussion . . . . . . . . 51
5.5.1 Optical constants of titanium dioxide ($TiO_2$) . . . . . . . . 51
5.5.2 Optical response near the soft X-ray absorption edge of $TiO_2$ and study of buried interlayers . . . . . . . . 59

**6 Soft X-ray reflectometry with a laser produced plasma source 65**
6.1 Introduction . . . . . . . . 65
6.2 Basic concepts and parameters . . . . . . . . 65
6.2.1 Laser-produced plasma (LPP) . . . . . . . . 65
6.2.2 Transmission grating . . . . . . . . 68
6.3 Reflectometer set-up . . . . . . . . 72
6.4 Measurement acquisition . . . . . . . . 76
6.5 Wavelength calibration . . . . . . . . 77
6.6 Reflectometer spectral resolution . . . . . . . . 79
6.7 Reflectometer limitations and lessons learned . . . . . . . . 82
6.8 Target materials . . . . . . . . 84
6.9 Results and discussion . . . . . . . . 86
6.9.1 Reflectometer debris analysis and sensitivity to capping layer thickness change. . . . . . . . . 86
6.9.2 Debris mitigation . . . . . . . . 89
6.9.3 The importance of the reference spectra . . . . . . . . 93
6.9.4 Reflectometer spatial resolution . . . . . . . . 95
6.9.5 Testing the reflectometer: Bilayer samples. . . . . . . . . 100
Sample M1 . . . . . . . . 101
Sample M2 . . . . . . . . 103
6.9.6 Spatial sample scanning . . . . . . . . 104
Sample M3 . . . . . . . . 105
Sample M4 . . . . . . . . 107
Sample M5 . . . . . . . . 108
Sample M6 . . . . . . . . 109

**7 Concluding remarks 111**

**A Ion magnetic deflection** **113**

**B MATLAB code for spectra calibration and reflectance measurement** **115**

**C IMD Software for reflectance simulation** **119**

# List of Abbreviations

| | |
|---|---|
| **PVD** | **P**hysical **V**apour **D**eposition |
| **CVD** | **C**hemical **V**apour **D**eposition |
| **SXR** | **S**oft **x-** **R**ay |
| **EUV** | **E**xtreme **U**ltra **V**iolet |
| **IR** | **I**nfra **R**ed |
| **E-beam** | **E**lectron **b**eam |
| **QCM** | **Q**uartz **C**rystal **M**icrobalance |
| **BEAR** | **B**ending magnet for **E**mission, **A**bsorption and **R**eflectivity |
| **XPS** | **x**-ray **P**hotoelectron **S**pectroscopy |
| **SE** | **S**pectral **E**llipsometry |
| **AFM** | **A**tomic **F**orce **M**icroscopy |
| **UHV** | **U**ltra **H**igh **V**acuum |
| **LPP** | **L**aser **P**roduced **P**lasma |
| **Nd:YAG** | **N**eodymium-doped Yttrium Aluminium Garnet |
| **EM** | **E**lectromagnetic |
| **RMS** | **R**oot **M**ean **S**quare |
| **CCD** | **C**harge **C**oupled **D**evice |
| **FWHM** | **F**ull **W**idth **H**alf **M**aximum |
| **RBSN** | **R**eaction **B**onded **S**ilicon **N**itride |
| **FEL** | **F**ree **E**lectron **L**aser |

# Chapter 1

# Introduction

### The soft X-ray and Extreme Ultraviolet regions of the electromagnetic spectrum

The electromagnetic spectrum between ultraviolet and X-ray radiation (shown in Figure 1.1) was one of the last regions to be investigated. In this region there are a great number of atomic resonances that lead to absorption of radiation in very short distances (nm-$\mu$m) in all materials. This peculiarity sets difficulties in the exploration of this region, but at the same time these resonances open the possibility of both elemental (C, N, O, etc.) and chemical (Ti, $TiO_2$, $TiSi_2$) identification and generates opportunities in both science and technology. Moreover, the relatively short wavelength potentially allows imaging of smaller structures as in X-ray microscopy and to write smaller features as in EUV lithography. To develop all these possibilities, advances in relevant technologies, such as material science and nanofabrication (e.g. thin films multilayer coatings), are needed. These will eventually lead to new scientific understandings generating feedback to the enabling technologies. Extreme ultraviolet (EUV) 5 nm $< \lambda <$ 40 nm and soft X-ray (SXR) 0.1 nm $< \lambda <$ 5 nm spectral regions are currently in a period of great development, growth and interchange between science and technology.
Furthermore, the "water window" consists of the SXR range between the K-absorption edge of oxygen (at $\lambda$=2.43 nm) and the K-absorption edge of carbon (at $\lambda$=4.4 nm). Water has a satisfactory transparency to these X-rays and a natural contrast with other elements found in biological specimens, creating opportunities to develop X-ray microscopy and spectroscopy in the life and environmental sciences [1].

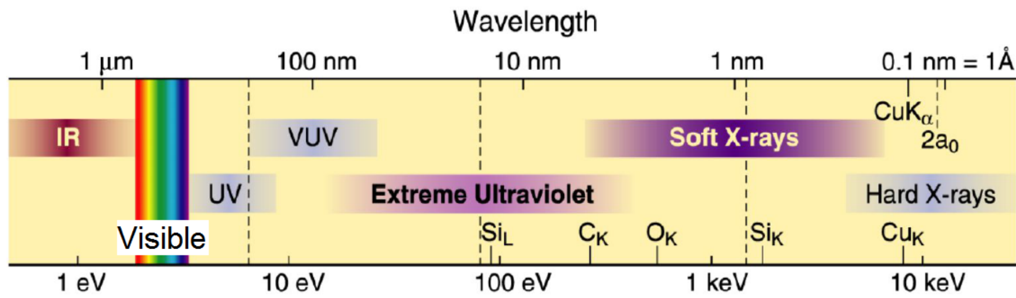


**Figure 1.1:** The electromagnetic spectrum shown from the infrared (IR) to the X-ray regions [1].

### Thin films

Thin film applications in optics were really born in the mid 1930's, when vacuum technology began to grow and advance within the framework of the electronics industry. It was then realized that the vacuum evaporation process with an adequate pumping system was the best method to produce an interference layer with specified optical properties. Subsequently it was discovered that it is possible to evaporate a succession of different layers. This led to the development of the first multilayer theories to pursue optical systems with anti-reflecting and reflecting characteristics, and filters for monochromatic interference [2]. The technology of thin film engineering has advanced in a dramatic way during the past decades, driven mostly by the need of new and enhanced products in the electronic and optical areas, not only with industrial but also with academic interests. For instance, the accelerated progress in solid-state electronic devices was made possible due to the development of new thin film technology, deposition and characterisation, leading to superior film quality and characteristics. Thin film deposition technology processes are still under development and rapidly changing, converging to even more advanced and complex electronic and optical devices in the future [3].

When light propagates through a medium with uniform refractive index, there is no scattered radiation. Scattering occurs when the index of refraction changes, within the same material or at the boundary between two different materials (or vacuum). Optical thin films coatings are used to modify the way optical devices reflect and transmit radiation in order to suit certain demands. Usually, these coatings are composed of one or multiple thin films deposited on the surface of the optical instrument (mirror, lens, etc.) to be tailored. Light propagating through a coated surface undergoes scattering and the devices generally operate under constructive or destructive interference, depending on what needs to be achieved. Thus, film thickness and radiation wavelength must be of the same order of magnitude. The parameters to be considered at the moment of designing optical coatings are usually film thickness of the layers involved, arrangement of the layers, their material, density and index of refraction [1]. Optical

coatings are considered an essential part of optical components and generally they represent the critical sector of entire optical systems, thus effort and dedication are paid to improve their performance. Applications can be found in a variety of areas: lasers, telecomunications, astronomy, aerospace, displays and lighting, are only a few examples of a long list [4].

### Thin films for soft X-rays optics

Since the discovery of X-rays (1895), this important research field, going from areas like X-ray source development to X-ray imaging and spectroscopy instrumentation, has been growing and developing non-stop [5].
X-ray source technology, that originally relied on small vacuum tubes in the laboratory, has now expanded to large scales such as synchrotron radiation facilities [6]. In terms of state-of-the-art X-rays sources, there are the X-ray free electron lasers (FELs), which are coherent sources of electromagnetic radiation, covering most of the electromagnetic spectrum making them appealing for different spectroscopic applications [7]. In the past recent years, there has been considerable research activity concerning table-top incoherent X-ray sources based on laser produced plasma (LPP) [8] [9] and even table-top FEL sources [10]. The advancements in X-ray source technologies are generally adapted to build a variety of instruments that can ultimately function with appropriate X-ray optical devices that serve for optical collection, collimation and convergence of the generated X-rays. These optical elements are, for instance, essential in the development of instruments such as soft X-ray microscopes, spectrometers, polarimeters or polarizers, EUV lithography tools that play a major role in the electronic industry, soft X-ray diagnostics of high temperature plasmas, and in cosmology and astronomy by X-ray solar imaging instruments [1] [6] [11] [12]
Due to the high absorption and low refractive index of all materials in the soft X-ray and EUV wavelength range, classical lenses or single reflection mirrors can not be successfully applied as optical elements. This peculiarity has prompted academia and industry to rethink reflection based optics to enhance performance through interference coatings. Stacks of multiple thin films layers (multilayers mirrors) of few nanometer thicknesses started to be considered as vital devices for normal and grazing incidence reflections [13]. Multilayer mirrors are produced by depositing several alternating layers of at least two materials with contrasting indices of refraction that generates positive interference of reflected waves [14]. Single and multilayer thin films are important both for scientific and industrial purposes; developing knowledge of optical properties of materials in the EUV and soft X-rays plays a major role in determining performances of optical elements used in this spectral range.
Currently, the major challenge in the production of single and multilayer films is to find optically and chemically compatible materials to be deposited on a nano-metric scale,

with sharp boundaries, especially when stacked in several layers. Furthermore, the different techniques for producing thin films, with varied deposition conditions, tailor the resultant design and properties of single and multilayers elements. Thus, along with the development, understanding and optimizing of the deposition techniques there exists a demand for production control and characterisation of these materials [15]. The majority of these matters are addressed and analysed in this thesis to some extent.

### Summary of the thesis

The thesis is arranged into six chapters. Each chapter has its own brief theoretical introduction accounting for the concepts embraced more specifically in each chapter.
Followed by this general introduction, relevant theoretical considerations are given in Chapter 2 concerning the interaction of light with matter and the general description of reflection and transmission of a single and multilayer structure.
In Chapter 3, we describe and present the thin film deposition technique used in this work to produce the samples under study.
In Chapter 4, we present a brief description of the characterisation tools and techniques that were implemented to determine the properties of the fabricated samples.
In Chapter 5, we investigate the compound $TiO_2$ which is considered to be a very promising and important material for EUV and soft X-ray applications. This is demonstrated by its competitive use as effective capping layers for Mo/Si multilayer (ML) mirrors [16] [17]], beam splitter (BS) for high-order harmonics [18] and as a component in novel MLs for "water window" wavelength [19] [20], just to name a few examples. The interest in developing optical coatings with high efficiency in the extreme ultraviolet and soft X-ray spectral region, is induced by activities such as synchrotron-based research, EUV X-ray lithography, X-ray astronomy, and plasma application [1]. For these reasons, we have considered it valuable to experimentally measure the index of refraction of $TiO_2$ thin films in this spectral region, along with a full physical characterisation. We present experimental values of both optical constants ($\delta$ and $\beta$) for $TiO_2$ in this wavelength range. The optical constants were determined by measuring angle-dependent reflectance of amorphous $TiO_2$ thin films with synchrotron radiation at the BEAR beamline of Synchrotron ELETTRA [21].
Performing measurements at a synchrotron facility like ELETTRA has both great advantages and limitations. Access to large scale facilities is usually expensive and beamtime availability is not always guaranteed. Thus, the advantages of performing characterisations on a compact table-top laboratory reflectometer can sometimes become prioritized.
In Chapter 6, we test and improve a spectral reflectometer used as a thin film characterisation technique. This part of the research is focused on producing a self-referencing grazing incidence reflectometer that works in the soft X-ray spectral range, based on a

laser produced plasma (LPP) source. The reflectometer is intended to be simple, relatively low cost and to provide reasonably fast and accurate reflectance measurements. The purpose of the work was initially to implement the spectral reflectometer as a characterisation tool on the multilayer samples we have produced, to demonstrate function and provide a proof of concept demonstration. For this, we produced several bilayer samples. The materials composing the samples were Cr, Ti, $TiO_2$ and Sc, chosen based on their relevance for soft X-ray and EUV applications. They are widely used as coating materials for optic devices, such as multilayer mirrors with high reflectance output [17] [16] [20] [22] [23]. They also present absorption edges in the soft X-ray region accessible to the reflectometer.

# Chapter 2

# Theoretical considerations

In this chapter a general theoretical introduction is given, that provides a background to the physics involved in the development of this work. We will briefly describe how light interacts with matter and provide the theoretical background to understand reflection and transmission of a single layer and a multilayer structure.

## 2.1 Interaction of light with matter

The processes involved in radiation-matter interaction are dependent on the energy range under study. Radiation with photon energy $\hbar\omega$ or wavelength $\lambda = 2\pi c/\omega$, will interact with the medium in which it is being propagated. For energies up to 20 keV, the predominant process is photon-electron electromagnetic coupling. In this energy range, the momentum associated with a photon is transferred to the atom by either photoelectric absorption, where a bond electron receives all the photon energy, or by Rayleigh and Thompson coherent scattering, where a bound-electron or a free-electron oscillates in the presence of an incident electromagnetic field, respectively.
For photon energies greater than the K-shell characteristic energy of the medium, photoelectric absorption becomes less probable and Rayleigh scattering turns into Thompson scattering, i.e. it becomes free-electron like. Furthermore, Compton incoherent scattering occurs for photon energies greater than 30 - 50 keV, this is when only a portion of the photon momentum is transferred to the electron [24]. When the initial photon energy exceeds 1 MeV, the photon interactions with the Coulomb field of the nucleus become the predominant absorption process. Pair production is possible if the photon energy is of the order of or greater than the rest mass of two electrons (1.022 MeV), where the photon is converted into an electron-positron pair sharing the initial photon energy [25]. For even higher energies, the probability of photon-interactions with the nucleus increases.
The EUV and soft X-ray energy ranges are included in the range where photoelectric absorption and Rayleigh scattering are the most probable interaction processes. At this stage, the behaviour of the constituent electrons in the atom of a material can be approximated as a collection of negatively charged oscillators bounded to the nuclei by Coulomb forces. When an incident electric field $\mathbf{E}(\mathbf{r}, t) = \mathbf{E}_o \exp[-i(\omega t - \mathbf{k} \cdot \mathbf{r})]$ propagates through the medium, these oscillators undergo harmonic motion, each of them having

a characteristic frequency $\omega_j$, resulting in a complex dielectric function for the material as shown in Equation 2.1:

$$\epsilon(\omega) = \epsilon_1(\omega) + i\epsilon_2(\omega) = 1 - \frac{4\pi r_o n_a c^2}{\omega^2} f(\omega) \tag{2.1}$$

where $n_a$ is the atomic density of the material, $r_o = e^2/4\pi\epsilon_o mc^2$ =2.818 x $10^{-13}$ cm represents the classical electron radius, m is the electron mass, while $f(\omega)$ is defined as the forward atomic scattering factor, and is given by Equation 2.2:

$$f(\omega) = f_1(\omega) - if_2(\omega) = \sum_j \frac{g_j\omega^2}{\omega^2 - \omega_j^2 + i\gamma\omega} \tag{2.2}$$

where $\gamma$ is a coefficient that accounts for the energy loss during the harmonic motion of the electrons, $g_j$ is the amount of electrons with resonant frequency $\omega_j$ and is defined as the *oscillator strength* associated with that frequency [24].
The forward atomic scattering factor is a multiplying factor that compares the electric field scattered by a single Thompson free-electron with a multi-electron atom.
Quantum mechanical theoretical calculations can provide a more accurate description of these interactions, however, the simplified semi-classical atomic scattering model gives similar results meaningful in the EUV and soft X-rays energy ranges [1].
For the classical limit, $g_j$ is an integer number and the sum of the oscillator strengths over all the characteristic frequencies in the atom results in the atomic number (Z),

$$\sum_j g_j = Z \tag{2.3}$$

In the quantum mechanical limit, after the electromagnetic field interacts with the atom, if we integrate over all the possible final states a similar result is obtained,

$$\int_0^\infty g_\omega d\omega = Z \tag{2.4}$$

where $g_\omega$ represents the oscillator strength. This relation is known as the Thomas Reiche-Kuhn rule.
The simple semi-classical model yields a solution for the scattered radiation by a multi-electron atom, which is identical to that derived by a quantum mechanical model (even if the interpretations of oscillator strengths are different). These results agree within certain limitations: the wavelength must be large compared to the atomic dimensions ($a_o/\lambda \ll 1$, $a_o$ is the Bohr radius) or the scattering has to be considered in the forward direction ($\theta \ll 1$), and the photon energy should not be near an atomic resonance, since the semi-classical model does not address lifetime (damping coefficient $\gamma$) and these energies require an understanding of this behaviour [1].
The definition of atomic scattering factor is meaningful only for energies where the atoms can be approximated as independent, under the assumption that individual

atoms scatter independently and the total coherently scattered field amplitude is the vector sum of these individualities.
The semi-classical model will not work well for low energies (E<50eV), where the optical properties are ruled by the electronic structure of the outer shells. At energies near an absorption edge, the chemical configuration of the atoms will strongly influence the optical properties of the material and the semi-classical model will also fail to accurately describe the actual interactions.
Within the previously mention constraints, the atoms scatter as dipoles,i.e. generating constructive interference only in the forward and backward directions. In this way the atomic scattering factor (f) becomes independent of the scattering angle and tends to be equal to the forward atomic scattering factor given by Equation 2.2.
The concept of atomic scattering factor can also be use to describe compound materials scattering. To do this, we express the atomic density $n_a$ as the sum of the atomic densities of all the constituent groups of atoms,

$$n_a = \sum_k n_k \tag{2.5}$$

where $n_k$ is the atomic density for atoms "type k" in the material. For incident photon energy values ($\hbar\omega$) between absorption edges but far from them, the contribution to the atomic scattering factor $f(\omega)$ is mainly from electrons with binding energies lower than the incident photon energy, $\hbar\omega_j < \hbar\omega$. These electrons respond to the incident radiation as free-electrons. The contribution from electrons with $\hbar\omega_j > \hbar\omega$ is negligible, responding as bound-electrons. When the incident photon energy well exceeds the K-shell binding energy of the material (highest binding energy), all the electrons in the atom act equally, as a system of free electrons. Thus, from Equations 2.2 and 2.3 the forward atomic scattering factor in the limit of high energies approaches the atomic number:

$$f(\omega) = \sum_j g_j = Z \tag{2.6}$$

when $\omega_j \ll \omega$ for all j.
This theoretical approach that explains radiation-matter interactions at a microscopic level is necessary to understand the macroscopic optical phenomenon that also accounts for effects of the fine structure.
The phase difference between the incident electromagnetic wave and the forward scattered wave in the medium results in a change in the velocity and amplitude of the transmitted wave from the material. These processes are described macroscopically by the complex index of refraction given by Equation 2.7:

$$n(\omega) = 1 - \delta(\omega) + i\beta(\omega) \tag{2.7}$$

where $\delta$ and $\beta$ are the *optical constants* of the material and they are energy (or wavelength) dependent. The complex index of refraction is defined by means of the dielectric function $\epsilon(\omega)$ as shown in Equation 2.8:

$$n^2(\omega) \equiv \epsilon(\omega) \Rightarrow \begin{Bmatrix} Re\{\epsilon(\omega)\} = (1-\delta)^2 - \beta^2 \\ Im\{\epsilon(\omega)\} = 2(1-\delta)\beta \end{Bmatrix} \tag{2.8}$$

Substituting $\epsilon(\omega)$ from Equation 2.1,

$$n^2(\omega) = 1 - \frac{4\pi r_o n_a c^2}{\omega^2} f(\omega) \tag{2.9}$$

In the EUV and soft X-ray energy ranges, where 1-$\delta$ $\approx$1 and $\beta$ $\ll$1, Equation 2.7 approximates as $n^2 \approx 1\text{-}2\delta\text{+}2i\beta$, and using Equations 2.2, 2.7 and 2.9 the optical properties are related to the real and imaginary parts of the forward atomic scattering factor as follow:

$$\delta \approx \frac{2\pi r_o n_a c^2}{\omega^2} f_1 \tag{2.10}$$

$$\beta \approx \frac{2\pi r_o n_a c^2}{\omega^2} f_2 \tag{2.11}$$

Expressions 2.10 and 2.11 are only valid within the constraints previously mentioned for the forward atomic scattering factor (long wavelengths with respect to atomic dimension, small scattering angle and the independent atom approximation). For low energy region (E<50eV) and near absorption edges these expression are not meaningful. At low energies, interactions with conduction or valence electrons dominate the optical response of the material [24].
For incident photon energies near natural resonance frequencies of the core electrons (binding energies), scattering factors and optical constants are expected to change abruptly due to resonance absorption of the strongly bound-electrons. Thus, fine structure information can be obtained through near-edge absorption and reflection measurements in the EUV and soft X-ray energy ranges, enabling to identify chemical composition and being a sensitive tool to the chemical configuration of an atom in its local environment [13].

## 2.2 Reflection and transmission of a multilayer structure

A multilayer structure is an optical coating consisting of a series of alternating thin films deposited on top of each other. The layers may be of different materials following certain order and arrangement. We will suppose each of them as a homogeneous and isotropic medium and all the layers to be plane-parallel to each other. The multilayer structures studied in this work are meant to have optical applications in the EUV and soft X-ray spectral regions, thus, their thicknesses will be of the order of the wavelengths involved, i.e. approximately of 1 to 100 nm.

### 2.2.1 Fresnel equations

When a plane wave is incident on an interface between two media (or layered interface), additional plane waves are created, these are a transmitted (or refracted) and a reflected wave as shown in Figure 2.1. The transmitted wave propagates into the medium $\mathbf{n}_2$ and the reflected wave propagates back into the first medium $\mathbf{n}\ _1$. Both waves are modified in amplitude and phase.

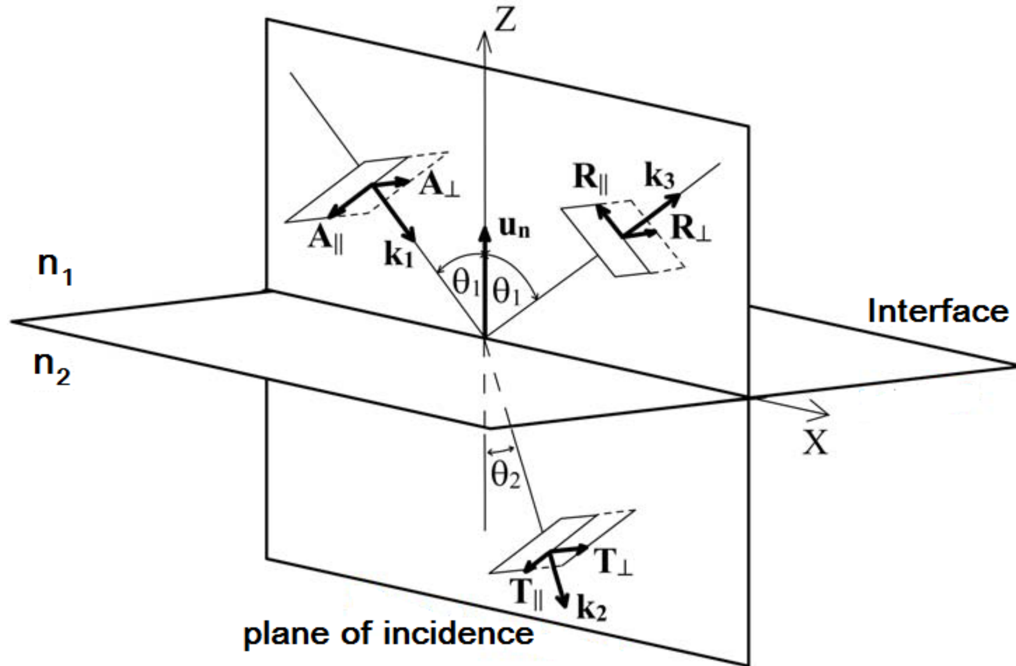


**Figure 2.1:** Incident plane wave in the interface between uniform and isotropic media $\mathbf{n}_1$ and $\mathbf{n}_2$ [26].

Fresnel equations define the complex amplitudes for the reflected and transmitted waves as a function of the complex amplitude of the incident wave, the complex index of refraction $\mathbf{n}_1$ and $\mathbf{n}_2$ of the media involved and the incident angle $\theta_1$, which is defined as the angle between the wave-vector of the incident wave ($\mathbf{k}_1$) and the normal to the interface $\mathbf{u}_n$. The plane of incidence contains the normal to the interface and the incident wave-vector. The boundary conditions of the electromagnetic fields state that the wave vectors of the reflected ($\mathbf{k}_2$) and transmitted ($\mathbf{k}_3$) waves are also contained in the plane of incidence. In Figure 2.1, $\mathbf{A}_{||}$ $\mathbf{A}\perp$, $\mathbf{R}_{||}$ $\mathbf{R}\perp$ and $\mathbf{T}_{||}$ $\mathbf{T}\perp$ are, respectively, the parallel and perpendicular (to the incident plane) vector components of the incident, reflected and transmitted field's amplitudes. At the same time the field amplitudes are perpendicular to their correspondent wave-vector. In order to satisfy the boundary conditions at all times and at all points in the interface, continuity conditions of the fields are also imposed, and from them we can deduce general properties of the reflected and transmitted waves. The wave-vector of the reflected wave is contained in the incidence plane, and the angle of incidence equals the angle of reflection ($\theta_1$). In a

same way, the law of refraction or *Snell's Law* states that the wave-vector of the transmitted wave is contained in the incidence plane and the relation between the angle of incidence and the angle of refraction is given by Equation 2.12 [26],

$$\mathbf{n}_1 \sin\theta_1 = \mathbf{n}_2 \sin\theta_2 \tag{2.12}$$

To fully describe the reflection and transmittance rules for electromagnetic waves, we must refer to the *Fresnel equations*, derived from Maxwell's equations by again applying the continuity conditions at a specific point in the interface [27]. These equations are meaningful in the interface of the two media and provide the parallel (p) and perpendicular (s) amplitude components of the reflected and transmitted wave.

$$r_{12}^{p} = |\frac{\mathbf{R}_{\parallel}}{\mathbf{A}_{\parallel}}| = \frac{\mathbf{n}_1 \cos\theta_2 - \mathbf{n}_2 \cos\theta_1}{\mathbf{n}_2 \cos\theta_1 + \mathbf{n}_1 \cos\theta_2} \tag{2.13}$$

$$r_{12}^{s} = |\frac{\mathbf{R}_{\perp}}{\mathbf{A}_{\perp}}| = \frac{\mathbf{n}_1 \cos\theta_1 - \mathbf{n}_2 \cos\theta_2}{\mathbf{n}_1 \cos\theta_1 + \mathbf{n}_2 \cos\theta_2} \tag{2.14}$$

$$t_{12}^{p} = |\frac{\mathbf{T}_{\parallel}}{\mathbf{A}_{\parallel}}| = \frac{2\mathbf{n}_1 \cos\theta_1}{\mathbf{n}_2 \cos\theta_1 + \mathbf{n}_1 \cos\theta_2} \tag{2.15}$$

$$t_{12}^{s} = |\frac{\mathbf{T}_{\perp}}{\mathbf{A}_{\perp}}| = \frac{2\mathbf{n}_1 \cos\theta_1}{\mathbf{n}_1 \cos\theta_1 + \mathbf{n}_2 \cos\theta_2} \tag{2.16}$$

It is important to note that $\mathbf{A}_{\parallel}$ $\mathbf{A}\perp$, $\mathbf{R}_{\parallel}$ $\mathbf{R}\perp$ and $\mathbf{T}_{\parallel}$ $\mathbf{T}\perp$ are complex quantities with amplitude and phase information of the fields, thus, the reflectance $r_{12}^{p,s}$ and transmittance $t_{12}^{p,s}$ are also complex quantities.

So far we have assumed ideally smooth interfaces to calculate reflection and transmission coefficients of plane incidence waves. In practice, the interface between two deposited layers is not ideally smooth, but with different morphologies and microstructure due to the different preparation conditions, growth methods and growth dynamics. This has a significant influence on the coating performance, generally reducing the ratio of the transmitted and reflected radiation in the specular direction. The roughness of a surface can be described by a function called the Power Spectral Density (PSD); this function is obtained as the square of the Fourier transform of the surface topography. The PSD is usually fitted by means of a Gaussian function, a Lorentzian function or a combination of both.

During theoretical calculation of the reflectance and transmission of an optical coating structure, the most commonly applied correction factors to account for roughness in a surface or interface are the Debye-Waller [28] [29] and the Nevot-Croce factors [30] [13]. The Nevot-Croce formalism is one of the most general theories found in the literature, since it accounts for any refraction index, angle of incidence and polarization of the

incident radiation. The only restriction in the formalism is that the surface or interface roughness or root mean square (RMS) values of the irregularities height must be considerably lower than the wavelength of the incident radiation [26].

### 2.2.2 Reflection and transmission of a single layer

In this section, it is shown how to calculate the reflectance (R) and transmittance (T) of a thin layer with index of refraction $\mathbf{n}_1$ laying between two other semi-infinite media with indices $\mathbf{n}_0$ and $\mathbf{n}_2$, respectively. The multiple reflections occurring when an incident plane wave goes trough a thin layer with smooth interfaces and thickness d, are schematically shown in Figure 2.2.

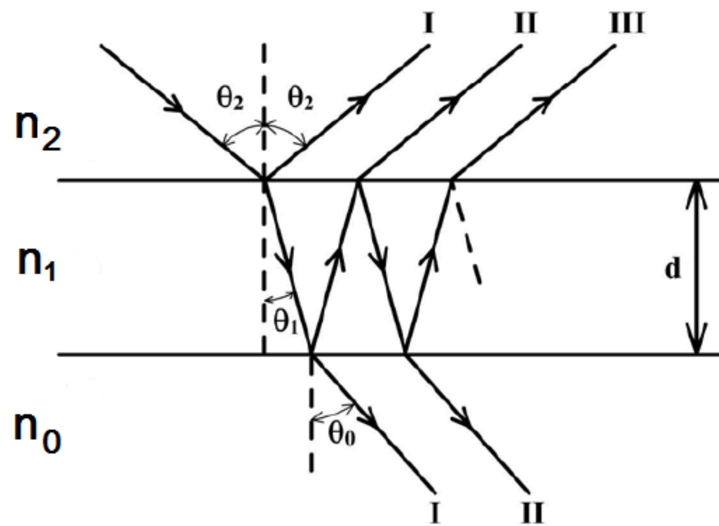


**Figure 2.2:** Multiple reflections in a thin layer of thickness d [26].

The angles of incidence, reflection and transmission are taken from the interface normal and are calculated using Snell's law as stated in the previous section. For every incident ray at an interface between media with indices $\mathbf{n}_i$ and $\mathbf{n}_j$ (with $j = i \pm 1; i, j = 0, 1, 2$), there is a reflected and transmitted one, with amplitude and phase given by the Fresnel equationss ($r_{ij}^{p,s}$, $t_{ij}^{p,s}$) [26]. Thus, we can define the resulting reflectivity $r_1$ (amplitude) of one thin layer ($\mathbf{n}_1$) as the sum of the multiple possible reflections causing interference $r_I$, $r_{II}$, $r_{III}$,..., as shown in Figure 2.2 and defined in Equation 2.17. We will refer to the total reflectance of one layer with the subscript "1", for two layers with "2" and so one; while when referring to the reflectance in an interface between two media we will use two subscripts, i.e. $r_{12}$ for the reflectance in the interface between medium 1 and 2.

$$\begin{aligned} r_1 &= r_I + r_{II} + r_{III} + \dots \\ &= r_{21} + t_{21} r_{10} t_{12} e^{i\beta_1} + t_{21} r_{10} t_{12} e^{i\beta_1} (r_{12} r_{10} e^{i\beta_1}) + \dots \\ &= r_{21} + r_{II} + r_{II} x + r_{II} x^2 + \dots \end{aligned} \tag{2.17}$$

where $x = r_{12} r_{10} e^{i\beta_1}$ and $\beta_1 = \frac{4\pi}{\lambda} \mathbf{n}_1 d_1 \cos\theta_1$. The real part of $\beta_1$ represent the phase change introduced between two consecutive waves due to the difference in the optical path, while the imaginary part represents the attenuation of the wave due to the medium's absorption. Knowing that for x<1 $\rightarrow \sum_{n=0}^{\infty} a x^n = \frac{a}{1-x}$, and $r_{21}$=-$r_{12}$, $t_{12}t_{21}$=1-$r_{12}^2$, we obtain Equation 2.18 for $r_1$,

$$r_1 = \frac{r_{21} + r_{10} e^{i\beta_1}}{1 + r_{10} r_{21} e^{i\beta_1}} \tag{2.18}$$

In a similar way, we can obtain an expression for the transmittance of a thin layer,

$$t_1 = \frac{t_{10} t_{21} e^{i\beta_1/2}}{1 + r_{10} r_{21} e^{i\beta_1}} \tag{2.19}$$

Furthermore, to account for the surface and interface roughness effects on the reflectance and transmittance, Equation 2.18 and 2.19 are multiplied by the Nevot-Croce [30] correction factor as stated in Section 2.2.1 to obtain the modified Fresnel equations:

$$r_1^* = r_1 exp(-2 q_1 q_2 \sigma^2) \tag{2.20}$$

where $\sigma$ is roughness, $q_i = 2\pi cos\theta_i/\lambda$ and $\lambda$ the wavelength of light. In a similar way transmittance is corrected.

### 2.2.3 Reflectance and transmittance of a multilayer structure

In this section, we generalize the concept previously presented, to calculate the reflectance and transmittance for multilayer structures. For a multilayer with M thin single layers, as shown in Figure 2.3(d), we first calculate $r_1$ and $t_1$ with Equation 2.18 and 2.19 for the single layer located at the lowest position ($n_1$), as shown in Figure 2.3(a). Next, we calculate $r_2$ and $t_2$ considering two layers ($n_1$, $n_2$), as shown in Figure 2.3(b), again using the Fresnel equations but replacing $r_1$ for $r_{10}$ and $t_1$ for $t_{10}$. The process is repeated again as schematized in Figure 2.3(c) until the M layers are considered, Figure 2.3(d). Finally, Equations 2.18 and 2.19 can be expressed in an iterative way for j=2...M:

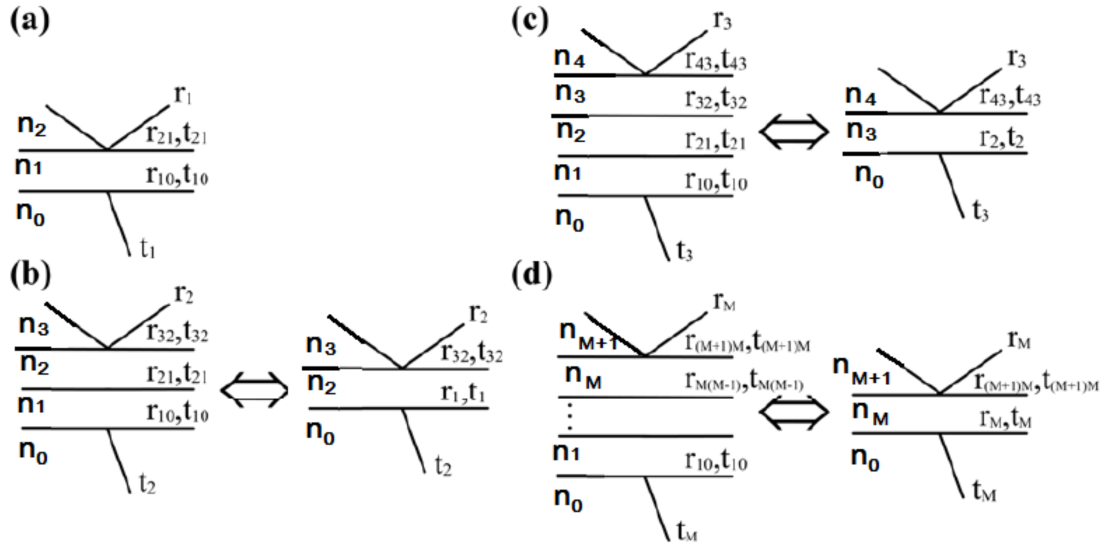


**Figure 2.3:** Schematic of the iterative process to obtain the reflectance and transmittance of multilayer structures [26].

$$r_j = \frac{r_{j+1,j} + r_{j-1}e^{i\beta_j}}{1 + r_{j-1}r_{j+1,j}e^{i\beta_j}} \tag{2.21}$$

$$t_j = \frac{t_{j-1}t_{j+1,j}e^{i\beta_j/2}}{1 + r_{j-1}r_{j+1,j}e^{i\beta_j}} \tag{2.22}$$

where $r_{j+1,j}$ and $t_{j+1,j)}$ are the Fresnel coefficients described in Equations 2.13 to 2.16, and $r_j$ and $t_j$ are the reflectance and transmittance coefficients for a multilayer with $j$ layers. $\beta_j = \frac{4\pi}{\lambda}\mathbf{n}_j d_j \cos\theta_j$. For absorbent materials, with complex index of refraction, the imaginary part accounts for the wave attenuation. The angle $\theta_j$ is calculated using Snell's law, Equation 2.12. The result for $\mathrm{r}_M$ and $\mathrm{t}_M$ are valid for the components $p$ and $s$ of the wave, by using the correspondent Fresnel coefficients. Once again, to account for roughness effects, the final equations must be multiplied by the Nevot-Croce corrector factor.

The reflectance $R$ and transmittance $T$ are given by the square of the Fresnel coefficients just obtained, as defined in Equation 2.23 and 2.24 [26]

$$R_{p,s} = |r_{p,s}|^2 \tag{2.23}$$

$$T_{p,s} = Re\{\frac{n_o cos\theta_o}{n_M cos\theta_M}\}|t_{p,s}|^2 \tag{2.24}$$

For experimental purposes, it is useful to express $R$ and $T$ as a function of the degree of polarization ($f$) of the incidence radiation,

$$f = \frac{I_p - I_s}{I_p + I_s} \tag{2.25}$$

where $I_p$ and $I_s$ are the incident intensities for s and p polarization. Thus we can express $R$ and $T$ as shown next [31]:

$$R = \frac{R_p I_p + R_s I_s}{I_p + I_s} \tag{2.26}$$

$$T = \frac{T_p I_p + T_s I_s}{I_p + I_s} \tag{2.27}$$

Or the equivalent expressions:

$$R = \frac{1+f}{2} R_p + \frac{1-f}{2} R_s \tag{2.28}$$

$$T = \frac{1+f}{2} T_p + \frac{1-f}{2} T_s \tag{2.29}$$

# Chapter 3

# Thin film deposition

In this chapter we outline the process and basics aspects of the deposition technique implemented in this work, we describe the experimental instruments used to carry on the depositions and we present how the samples were prepared. All depositions were performed by the author at LUXOR laboratory, of the "Istituto di Fotonica e Nanotecnologie" (CNR-IFN).

## 3.1 Introduction

The optical properties of a thin film depend on physical and micro structural properties, which in turn are the result of the preparation conditions and deposition method implemented to produce the film. Understanding the experimental technique chosen to produce the films helps in controlling and manufacturing a material with reproducible characteristics. It is then important to relate fabrication parameters with the film's final properties.
The material *transport* phase refers to the mechanism that allows the material to reach the surface of the substrate for the creation of the thin film, and the *adhesion* phase of the material refers to the chemical and/or physical process that allows the material to remain fixed on the substrate and then continue to form the thin film.
Regarding the material transport stage, the different deposition techniques can be categorized into two big groups known as *Physical Vapour Deposition (PVD)* and *Chemical Vapour Deposition (CVD)* [32]. In PVD the transport stage of a material is based on physical processes, where atoms are transferred from a solid material source to the substrate surface where they set and form the thin film. Thermal and electron beam evaporation, sputtering, pulsed ion beam evaporation and pulsed laser deposition (PLD) are, among others, the most used and important techniques of thin film deposition that belong to this category. In evaporation, the material is turned into a vapor by either boiling or subliming, while in sputtering the atoms are ejected when bombarding gaseous ions impact a solid disc target surface.
On the other hand, in CVD the transfer process is chemically achieved, where a volatile compound of the material we wish to deposit reacts with other gases and produces a non-volatile solid that condenses on the substrate surface [33]. Significant methods that

fall in this category are Spray pyrolysis, dip-coating, atomic layer deposition (ALD) and sol-gel synthesis. One main difference between PVD and CVD is that a high vacuum environment is needed for the first kind of process, while many of the CVD methods can be done in just low pressure or atmospheric conditions.
Other deposition processes may combine both physical and chemical reactions; these joint processes can be categorized as physical-chemical methods.
A survey with a detailed description of all the existent methods is beyond the scope of this work, but they can be found in references such as [33] [3] [32].
The technique used to fabricate or deposit the samples in this work is known as the *Electron Beam (E-beam) evaporation technique*, which because of its nature belongs to the general PVD category and it will be described in the following sections.

## 3.2 Electron beam evaporation

The e-beam evaporation deposition process is performed inside a chamber under high vacuum to assure a high purity on the deposited film, avoiding undesired oxidation of the materials and reducing the gas particle density to guarantee a long mean free path for collisions [34].
To obtain acceptable deposition rates during the fabrication process, each material must reach its characteristic vapor pressure, when the atoms will start to abandon the surface of the source material. The active and constant pumping of the chamber to maintain the vacuum, enables a constant deposition pressure that corresponds to the real vapor pressure of the material being evaporated. A rule of thumb is that a reasonable deposition rate is obtained in a typical vacuum system if the vapor pressure of the evaporant is in the range of $10^{-2}$ to $10^{-3}$ mbar. The temperature range at which the evaporant material must be heated to reach this vapor pressure is very wide (from 800$^{o}$C to 3000$^{o}$C) and depends on the source material selected. So for each deposition it is necessary to define the appropriate pressure and temperature conditions to accomplish the expected results. A too rapid film formation rate is usually avoided since rapidly deposited oxide layers are commonly optically absorbing due to the formation of sub-oxides, also the layer thickness is difficult to control wiht high rate film formation [32].

The energy source used for the evaporation must be able to heat the evaporant to the appropriate temperature for deposition, and should maintain certain basic performance standards; for example it should not chemically react with the evaporant material nor contaminate it nor release gases, while being able to repetitively reproduce deposition conditions.

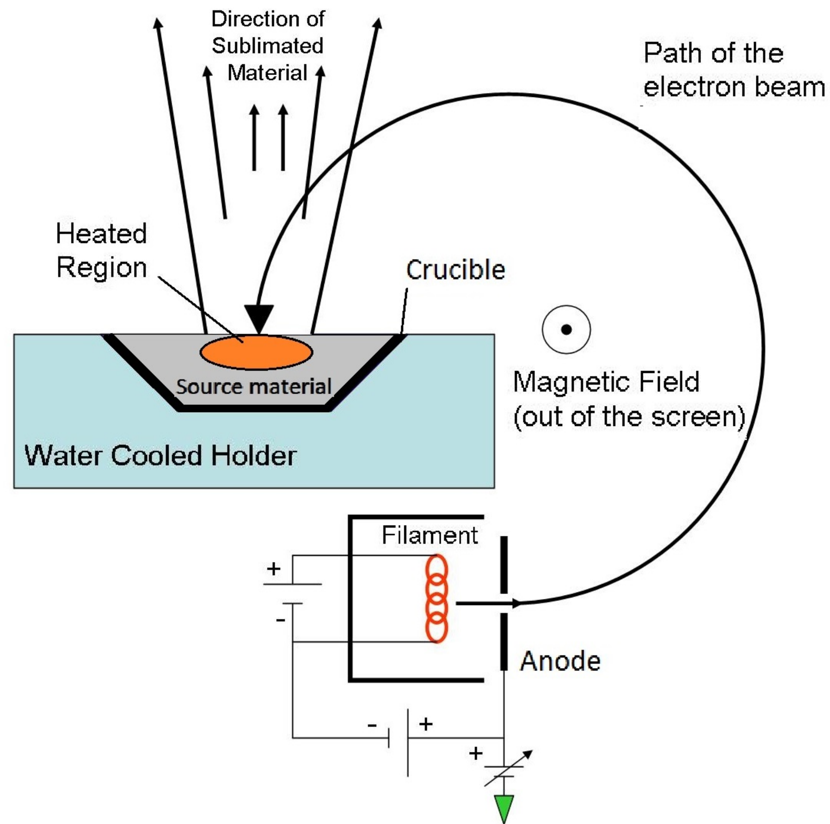


**Figure 3.1:** Schematic of the electron beam gun unit [35].

In the e-beam evaporation technique the energy source is an electron gun, schematically represented in Figure 3.1. A filament (cathode) is heated to thermionically emit electrons, the filament is biased with a negative potential with respect to a nearby grounded anode (from 4 to 20 kV) to produce an electric field and accelerate the electrons in the form of a beam. After that, magnetic fields are properly applied to focus and deflect the e-beam in a $270^o$ circular arc, impacting the target surface in a perpendicular way. As the electrons strike the evaporant they rapidly lose their kinetic energy to the surface atoms as thermal energy, thus increasing the target temperature [36], which eventually causes the evaporation of the material towards the substrate positioned above the target in the vacuum environment. Between the source and the substrate, there is a mechanical shutter which serves to control when the particles reach the substrate to begin and end the deposition. The entire process should be well regulated to obtain a uniform evaporation.
The evaporant material is usually placed in a crucible in forms of small sized pellets, and the crucible is inserted in a water cooled holder in the e-beam unit. Due to elevated temperatures, the material sometimes may sublime and melt. So the crucible must be properly chosen, making sure that it is thermally and chemically compatible with the specific material we want to evaporate.
The variation of the evaporation rate is related to the emission current of the e-beam

gun filament. For higher current, there is a higher e-beam flux and a higher rate of heat transfer to the target, this implies a higher evaporation rate. Ultimately, the current from the e-beam gun is the parameter we externally control during the deposition.
The advantages of using an e-beam gun as an energy source for evaporation are many. For instance, the heat is localized in a thin surface layer of the target material, making it very efficient over resistance heating, for example where the whole evaporant must be heated. It also allows to heat and evaporate a combination of materials at the same time with the aim to obtain films with modified index of refraction with respect to the deposition of each single material separately. Contamination from the filament or the crucible is avoided since the filament is isolated from the evaporant and the e-beam does not interact with the crucible.

### 3.2.1 Deposition geometry

Early ideas to understand and quantify the evaporation phenomena lead to basic expressions for the evaporation rate from both solid and liquid surfaces,

$$\Phi_{evap} = 3.513 \times 10^{22} \frac{P_{vap}}{\sqrt{MT}} \frac{molecules}{cm^2 sec} \tag{3.1}$$

where $\Phi_{evap}$ is the evaporation flux in number of atoms (or molecules) per unit area per unit time, T is the temperature in Kelvin ($^o$K), $P_{vap}$ the pressure in torr and $M$ is the dimensionless molecular weight of the evaporant. A useful alternative to this expression is:

$$\Gamma_{evap} = 5.834 \times 10^{-2} P_{vap} \sqrt{\frac{M}{T}} \frac{g}{cm^2 sec} \tag{3.2}$$

where $\Gamma_{evap}$ is the mass evaporation rate [33]. Evaporation from a point source is the simplest to model. As shown in Figure 3.2(a), the particles evaporated are assumed to emerge from an infinitesimally small area (d$A_e$) of a sphere of surface area $A_e$ with a uniform rate of mass evaporation. Thus, the total evaporated mass is given by:

$$M_e = \int_0^t \int_{A_e} \Gamma_e dA_e dt \tag{3.3}$$

From this total quantity, some amount d$M_s$ falls on the substrate of area d$A_s$. Considering the projected area d$A_c$ of d$A_s$ on the sphere to be d$A_c$=d$A_s$ $\cos\theta$, the proportionality d$M_s$:$M_e$=d$A_p$:$4\pi r^2$ holds, and we obtain the expression for the mass deposited per unit area assuming a point evaporant source:

$$\frac{dM_s}{dA_s} = \frac{M_e \cos\theta}{4\pi r^2} \tag{3.4}$$

On a "per unit time" basis we speak of deposition rate (atoms/cm$^2$sec).

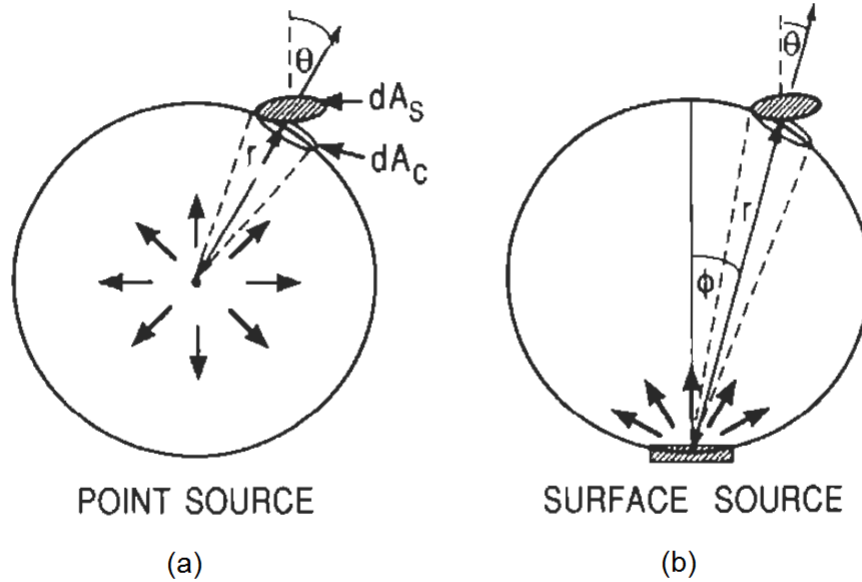


**Figure 3.2:** Schematic of the evaporation from (a) a point source and (b) a surface source [33].

The deposition rate depends on the geometric orientation of the substrate and the inverse square of the source-substrate distance. For instance, if the substrate is placed tangentially to the surface of the receiving sphere it implies that $\cos\theta = 1$ and the coating would be uniform.
The deposition process implemented in this work is based on evaporation from a small source area (not a point source), consequently we refer to the *Knudsen cell* model to represent the effusion [32]. This cell describes an isothermal enclosure at a temperature $T$ that contains a gaseous evaporant with a vapor pressure $P_{vap}$. Through a very small aperture on the cell, the molecules of the evaporant effuse into to the vacuum environment. The model assumes that the external pressure is lower than the vapor pressure inside the cell, so that the mean free path is greater than the dimensions of the cell and the vapor can expand towards the chamber.
The kinetic theory of gases predicts that the molecular flux of the vapor effusing from the small aperture is directed according to a cosine distribution law, and experiments corroborate this. The mass deposited per unit area by a Knudsen cell source is given by:

$$\frac{dM_s}{dA_s} = \frac{M_e \cos\ \phi \cos\theta}{\pi r^2} \tag{3.5}$$

which depends now on the emission and incidence angles, as defined in Figure 3.2(b). Evaporation from a small source area is equally modeled by Equation 3.5 [33].

Based on careful measurements of the angular distribution of film thickness, it has

been observed that rather than the cosine distribution as a Knudsen cell provides, a $cos^n\phi$ evaporation distribution law is more similar to reality under certain conditions. As shown in Figure 3.3, $n$ determines the geometry of the vapor cloud and the angular distribution of the flux. Physically, $n$ depends mostly on the source or crucible geometry [33]. For example, for a deep narrow crucible $n$ is large and the flux is very directed and confined. The Knudsen cell distribution corresponds to $n = 1$.

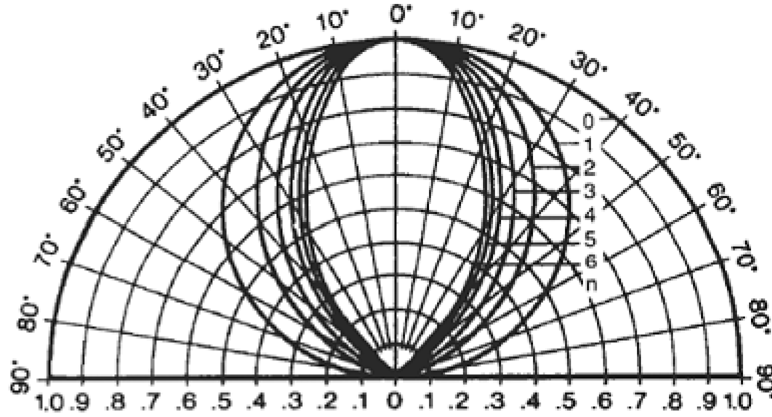


**Figure 3.3:** Calculated vapor clouds effusion from a source with different cosine exponents [33].

### 3.2.2 Film thickness uniformity

Maintaining the uniformity of the deposited thin film is essential for the fabrication of optical devices having high reflectance output. Using the equations presented in the previous section, the thickness distribution of important source-substrate geometries can be calculated. For instance, considering the evaporation both from the point and small surface source onto a parallel plane substrate as shown in the insert of Figure 3.4, the film thickness $d$ is given by $dM_s/\rho\ dA_s$, where $\rho$ is the density of the deposit. Hence, for the point source:

$$d = \frac{M_e \cos\theta}{4\pi\rho r^2} = \frac{M_e h}{4\pi\rho r^3} = \frac{M_e h}{4\pi\rho(h^2 + l^2)^{3/2}} \tag{3.6}$$

The thickest deposition ($d_o$) occurs when l=0, giving $d_o = M_e/4\pi\rho h^2$. Normalizing the thickness with respect to the thickest deposition we get:

$$\frac{d}{d_o} = \frac{1}{(1 + (l/h)^2)^{3/2}} \tag{3.7}$$

In a similar way, we express the film thickness for the small surface source:

$$d = \frac{M_e \cos\theta \cos\phi}{\pi\rho r^2} = \frac{M_e h.h}{\pi\rho r^2 r.r} = \frac{M_e h^2}{\pi\rho(h^2 + l^2)^2} \quad (3.8)$$

For this situation cos$\theta$=cos$\phi$=h/r, and the normalization to the thickest deposition $d_o$=$M_e/\pi\rho h^2$ is given by:

$$\frac{d}{d_o} = \frac{1}{(1 + (l/h)^2)^2} \quad (3.9)$$

In Figure 3.4 a comparison between Equation 3.7 and 3.9 is made, showing that less thickness uniformity will be produced with a surface source.

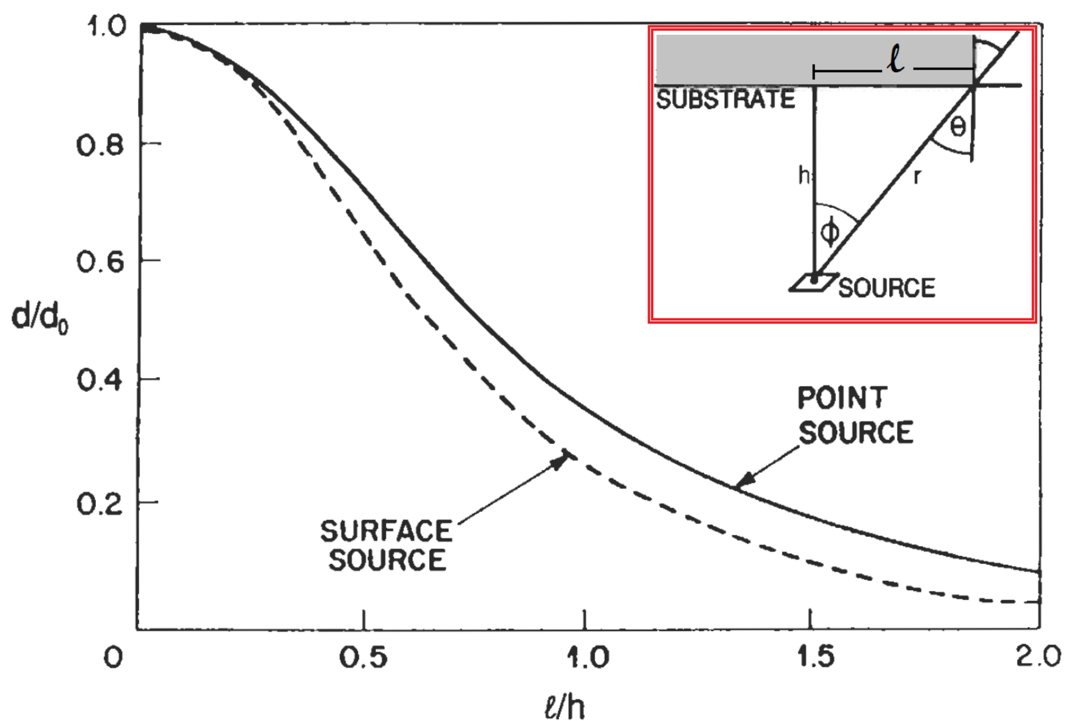


**Figure 3.4:** Film thickness uniformity for point and small surface sources. (Insert) Schematic of the geometry of evaporation onto a plane-parallel substrate [33].

The abrupt decrease in uniformity at greater $l/h$ becomes evident and affects the thickness uniformity of the depositions with a fixed substrate. However, it can be overcome with a rotating substrate holder further promoting uniformity with a planetary rotating substrate (revolution and rotation axes). Deposition uniformity is then achieved because source-substrate distances are compensated by emission rate and reception angles. The substrate collects the vapor at multiple positions above the source making it less sensitive to changes in the molecular intensity. Small sized samples and good quality vacuum will clearly contribute to film uniformity in e-beam deposition.
Thus, we can conclude that during the deposition process the location of the substrate

inside the chamber is not trivial. Its position relative to the source must be established by certain requirements, such as, restrictions on the incidence angle of the molecules upon the substrate surface, or whether the goal is to collect the maximum of the evaporant produced or if there is any prescription on the thickness of the films as a function of the substrate area, e.g. uniformity of the film. Depending on the conditions that apply, some trade-offs are required. For example, to achieve a uniform film thickness, only a small percentage of the evaporant is collected on the substrate while the rest ends up on the walls or other parts of the chamber. In other situations we may be more interested on the efficiency of the evaporation rather than the uniformity and so on.
Summarizing some of the previous observations, we can say that the quality and final characteristics of the deposited films will depend on parameters such as the substrate temperature, deposition rate, substrate-source distance, base pressure, etc. The homogeneity of the films will depend on the geometry of the evaporation source and again on the distance from this source to the substrate.

## 3.3 The e-beam deposition system

**Figure 3.5:** E-beam chamber system at LUXOR laboratory.

The Electron beam deposition facility used to produced the samples studied in this work, is located at the LUXOR laboratory, of the "Istituto di Fotonica e Nanotecnologie" (CNR-IFN) in Padova, Italy. The system is shown in Figure 3.5. It mainly consists of a deposition chamber where the process of film formation is carried on, the e-beam gun unit, the vacuum system and a control panel (the system was acquired from ION-VAC Process).

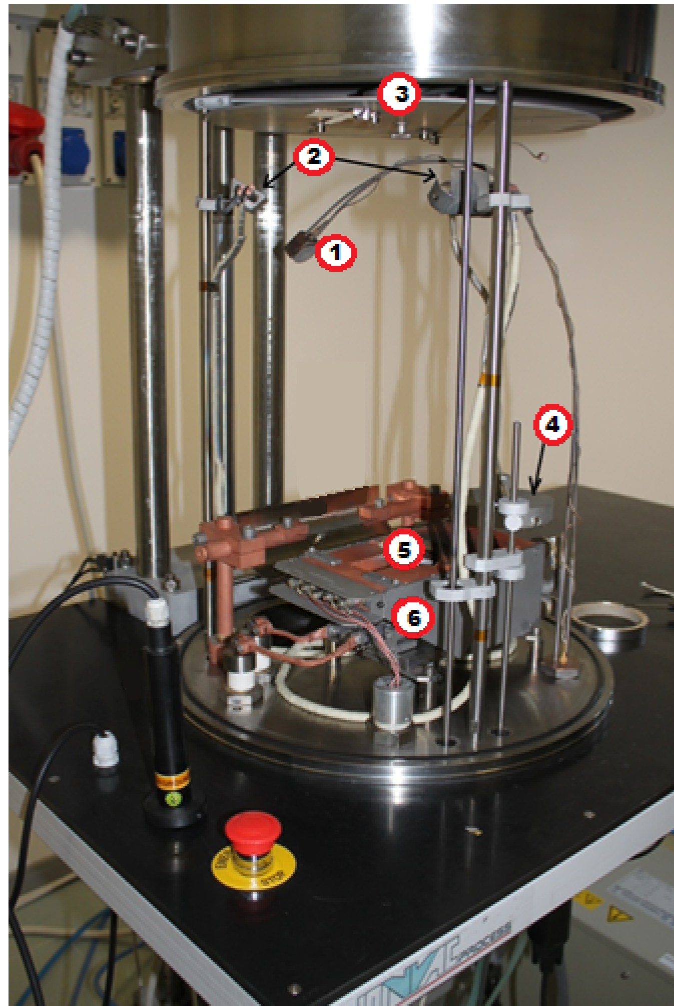


**Figure 3.6:** Tooling inside the e-beam chamber deposition. (1) QCM, (2) heater lamps, (3) rotating substrate holder, (4) shutter, (5) crucible holder and (6) e-beam gun unit.

The deposition chamber is a high vacuum stainless steel cylinder with a small frontal circular Pyrex window to visually monitor the evaporation process. The vacuum system consists of a primary scroll pump to achieve the initial vacuum, connected in series to a turbomolecular pump that can finally reach pressures of approximately $10^{-7} mbar$. The pressure in the chamber must be lower than $10^{-4} mbar$, to avoid discharges and damage of the e-beam gun filament [37], and a pressure of the order of at least $10^{-5} mbar$ is desirable to ensure purity in the deposited films. Inside the chamber

(Figure 3.6), in the top part, a rotating substrate holder is located, as well as two 1000 W quartz lamps which work as substrate heaters (reaching up to $300 - 400^oC$). To control the deposition rate and to monitor the thickness of the films in real time, a quartz crystal microbalance (QCM) is strategically installed to receive the evaporant without blocking the substrate, where the actual film is supposed to grow. The QCM registers a change in the frequency of the crystal due to a change in mass deposited on it. This change of mass is then converted into a thickness change of the deposited film, assuming a known acoustic impedance and density of the film.
In the evaporant path, between the crucible an the substrate holder, there is a mechanical shutter. After all the other necessary parameters are set (substrate temperature, vapor pressure, current emission, etc.), the shutter is controlled by the operator to define the initial and final moment of deposition. If a very precise thickness control is required, special attention must be paid to the time delay the shutter control may have between the command sending and the actual opening/closure.
The crucible holder is located in the bottom part of the chamber, and can be rotated to select up to four different materials without opening the chamber. Right below is the e-beam gun unit. This is a Temescal electron gun which operates at a 8kV acceleration voltage with a tunable filament current between 0 to 1.5 A. The e-beam is deflected in a 270$^o$ circular arc by means of electromagnetic fields, striking the target surface in a perpendicular way. To achieve a more uniform heating process of the surface target, these fields can be externally controlled with a unit called "$sweeper$". The e-beam sweeps the evaporant surface in a particular profile shape by selecting a waveform and, consequently, the longitudinal and latitudinal position of the beam.
Both the crucible holder and the chamber walls are cooled by a water running system.

## 3.4 Sample preparation

### 3.4.1 Substrates

For all samples we used Silicon (100) polished wafers as substrates for deposition. They were cut into sizes of approximately 2x2 cm. Prior to performing the deposition, the substrates were cleaned by sonication to remove oils, organic residues and foreign particles that may reduce the adherence and the performance of the coating. The substrates were dipped in acetone and isopropanol and rinsed in distilled water for at least 15 minutes each. Sometimes it was necessary to repeat the process several times until the substrate was visibly clean. We used pyrex bath containers and a Branson 2200 ultrasonic cleaner. Subsequently, the substrates were blown dry and gently heated to evaporate any remaining liquid. It is very important to make sure that no stain or drop is left on the substrate since this will greatly affect the film's structure and properties. Immediately after the cleaning process, the substrates were loaded into the deposition

chamber under vacuum in order to reduce possible oxidation and contamination due to contact with air. For every sample produced we also introduced in the deposition chamber a second substrate equally treated to generate a witness sample that we would eventually use for characterisation processes, in order to avoid contamination on the real sample, as much as possible.

### 3.4.2 Titanium dioxide samples

In this work, three amorphous $TiO_2$ thin films of different thicknesses were grown using the electron beam evaporation technique with the Temescal e-beam gun. We identified them as Eb1, Eb2 and Eb3, of thickness 22.7 nm, 48.5 nm and 102.9 nm, respectively. The substrate-target distance was set at 40 cm, and the substrate holder was rotating during the deposition process to obtain a uniform film thickness distribution. We used 3-6 mm sized pieces of $TiO_2$ with a purity of 99.9% as the evaporation material. Depositions were carried out at a working pressure of approximately $3x10^{-4}$ mbar by previously achieving a base pressure of $1.4 \times 10^{-5}$ mbar. Prior to every deposition, we performed pre-evaporation of the source material for several minutes with the shutter closed, in order to outgas the material and to eliminate any contamination on the source material.
The substrates were usually heated once inside the vacuum chamber and prior to deposition. This was done to improve the film-substrate adhesion and the mechanical hardness of the film [32]. Prior to the sample fabrication of $TiO_2$ thin films, we did a deposition test of this material to observe how the substrate temperature ($T^oC$) would affect the surface roughness. In the temperature range from ambient to $250^oC$, we reached an optimization of low superficial roughness by setting a substrate temperature of $150^oC$. The deposition rate controlled by the quartz crystal micro-balance, was of 0.3 - 0.5 Å/sec, with a current emission of 28 mA. With these parameters we were able to control the thickness of the samples fairly well. After the deposition processes, all samples were always handled with proper tools and kept in clean plastic containers.

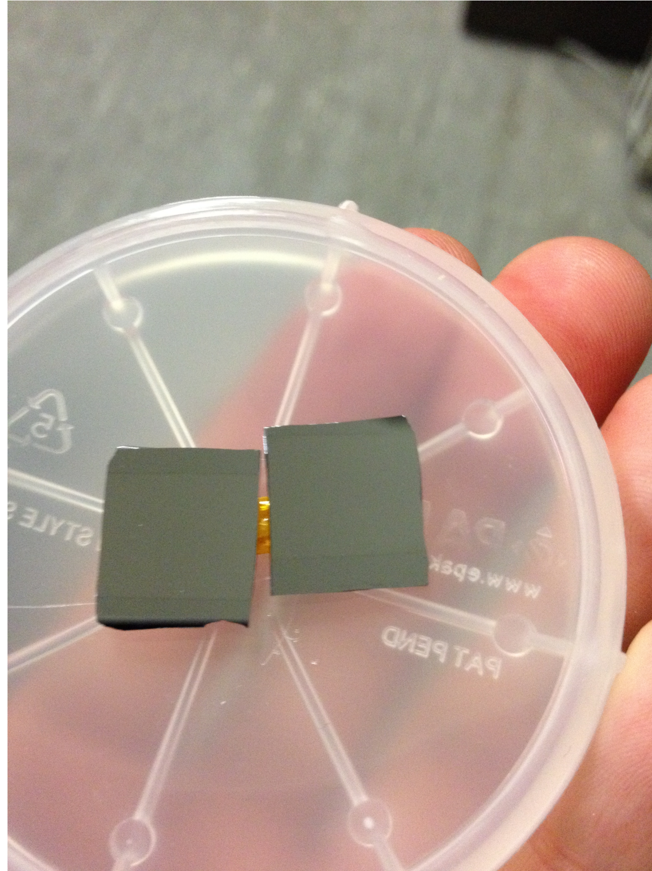

**Figure 3.7:** Samples of $TiO_2$ thin film deposited on Silicon (100) substrate

### 3.4.3 Bilayer samples

With the same technique we deposited two sets of bilayer samples of different materials on Si(100) substrates. The first set was formed by the combination of Ti over Cr, while the second set was made of $TiO_2$ over Sc, both sets with different thicknesses in each layer. The structure of the samples is represented in Table 3.1 for the first group and in Table 3.2 for the second. To clarify how to read the tables, we describe the structure of sample M3 as an example: sample M3 consists of a 5 nm Cr bottom layer deposited over the Si substrate, and a 3 nm Ti top layer.

| | Sample Id | | | |
|---|---|---|---|---|
| Material | M1 | M2 | M3 | M4 |
| Ti | 5 nm | 5 nm | 3 nm | 3 nm |
| Cr | 5 nm | 2 nm | 5 nm | 2 nm |
| Si substrate | | | | |

**Table 3.1:** Schematic of the Ti/Cr/Si bilayer samples structure

| | **Sample Id** | |
|---|---|---|
| Material | M5 | M6 |
| $TiO_2$ | 5 nm | 38 nm |
| Sc | 5 nm | 55 nm |
| Si substrate | | |

**Table 3.2:** Schematic of the $TiO_2$/Sc/Si bilayer samples structure

The substrate-source distance was 40 cm, with the substrate holder rotating during deposition. For these samples we used as evaporant materials: 1/8" x 1/8" Cr pieces with a purity of 99.995%, 1-6 mm sized Ti pieces with a purity of 99.998%, 0.5" x 0.5" Sc pieces with a purity of 99.9% and 3-6mm sized pieces of $TiO_2$ with a purity of 99.9%. The base pressure achieved before deposition of all the samples was of the order of $10^{-5}$mbar, with working pressures of the order of $10^{-4}$-$10^{-5}$mbar, which varied depending on the material being evaporated. The substrate were pre-heated to 150$^o$ but the deposition was performed with a substrate temperature of approximately 40-50$^o$C. Cr was deposited at a deposition rate of 0.4-0.6 Å/sec with a current emission of ∼25.5 mA. Ti was deposited at 0.7-0.9 Å/sec with a current emission of ∼26.5 mA. $TiO_2$ was deposited at 0.2 Å/sec with a current emission of ∼26.6 mA. Sc was deposited at 0.7 Å/sec with a current emission of ∼25 mA. After the deposition processes, all samples were always handled with proper tools and kept in clean plastic containers.

# Chapter 4

# Thin films characterisation: instruments and methods

This chapter presents a brief description of the characterisation tools and techniques that were implemented to ascertain the properties of the fabricated samples. We also introduce some of the specifications under which the measurements were done in this work.

## 4.1 Introduction

After the films were grown, a complete characterisation was carried out on the $TiO_2$ samples, with structural, compositional, morphological and optical analyses. This is necessary not only to have a better understanding of the film behaviour, but to relate the influence of the deposition parameters and conditions to the final properties of the deposited films. This in turn helps to optimize the growth conditions of the films. The $Sc/TiO_2$ and Cr/Ti bilayers were grown with a different aim so the characterisation performed on them was mainly optical.
Several techniques were implemented. In particular, a needle *profilometer* and *spectral ellipsometry* (SE) were used principally to measure the thickness of the films in two independent ways. The profilometer is located at LUXOR laboratory, while the spectral ellipsometer belongs to the Hybrid Materials Laboratory of the Industrial Engineering Department at the University of Padova (UNIPD). *Atomic Force Microscopy* (AFM) was implemented to analyse the surface conditions, mainly to measure the roughness of the samples surface. This was performed at the LUXOR laboratory (CNR-IFN). With *X-ray Photoelectron Spectroscopy* (XPS) we determined chemical composition, at the Department of Chemical Sciences (UNIPD). *X-ray Diffraction* (XRD) was also performed on the $TiO_2$ samples to detect their structure. Since all the samples resulted to be amorphous films, this did not open any further discussion and we did not consider a description of this technique necessary. *Reflectance* measurements were performed at two different facilities. For the $TiO_2$ thin film samples, the experiments were performed at the Bending magnet for Emission, Absorption and Reflectivity beamline (BEAR) of ELETTRA Synchrotron (Trieste, Italy). The bilayers were characterised using a table-top grazing incidence reflectometer in the water window region (2-5 nm), based on a

laser produced plasma source, at University College Dublin (UCD). In the following paragraphs we briefly introduce these techniques and the equipment and parameters used. Regarding the last two mentioned techniques (for reflectance measurements), complementary information and results will be given in the succeeding chapters.

## 4.2 Film thickness

To reproduce the properties of a thin film, it is necessary not only to control the deposition parameters of the film and keep them constant, but also to be able to reproduce its thickness. Thin film thickness is a very important parameter, it plays a significant role in the definition of the material properties and must be well characterised.
Thickness was monitored *in situ* using a QCM, as mentioned in Chapter 3, but generally this requires a very meticulous calibration, and so thet instrument was mainly used as a guide for the thickness in real time, rather than as a tool to measure final thickness. For a more accurate characterisation we used two independent tools after the film deposition, a stylus Profilometer and Spectroscopic Ellipsometer.

### 4.2.1 Quartz Crystal Microbalance (QCM)

This device is mainly constituted by a cooled thin quartz crystal, that is located inside the deposition chamber and works in a vacuum environment. Quartz is a piezoelectric material and is used as an oscillator. When a thin film is deposited on the quartz, the frequency of resonance at which the quartz is oscillating is modified. This modification is linearly proportional to the mass increase deposited on the crystal. The QCM is capable of precisely measure the mass added to the oscillating sensor [39]. The monitor of the microbalance makes a conversion of the mass information to thickness, by knowing the density and the Z-ratio of the material deposited. The Z-ratio is a parameter that relates the elastic properties or acoustic impedance of the material deposited with those of the quartz. In this work, we used an XTM/2 model QCM, fabricated by INFICON.
As we described in Chapter 3, the deposition rate over a certain surface depends on the distance between the evaporant source and the surface and on $cos\theta$, where $\theta$ is the angle between the normal to the surface and the symmetry axis of the source. This means that the spatial separation between the surface (or substrate) and the QCM will translate into different thickness depositions. This implies that the QCM should be as close as possible to the substrate during deposition, in order to reduce this mismatch. Nonetheless, a correction can be made to account for this difference in deposited thicknesses. This parameter is called the $tooling factor$, and is the ratio between the deposited thickness on the substrate and the deposited thickness on the quartz sensor surface. These corrections can be incorporated in the monitor set up, and after a first

calibration the read out on the monitor will fairly approximate the thickness being deposited on the substrate.
Since the deposition conditions may vary from one deposition to the other (vapor cloud distribution, temperature changes, ageing of the quartz, etc.) it is always recommended to use complementary techniques to determine the thickness of the deposited films. In our case, we implemented two independent techniques which are described below.

### 4.2.2 Profilometer

This technique is based on a diamond tipped stylus in contact with the surface of the sample. The profilometer takes measurements by electromechanically moving a stage where the sample rests with high precision. The operator sets the scan length, stylus force and scan speed. In this way, the tip is moved across the surface recording vertical displacements of the stylus due to changes in the surface topography. These are converted into height (z) values equivalent to the surface variations. A feedback system keeps the stylus force pressing against the surface constant and the z variations are used to reconstruct the surface topography [40]. A schematic of the technique is shown in Figure 4.1. To measure the thickness of a deposited film, we masked a section of the substrate prior to deposition, creating a step on the sample surface equivalent to the thickness of the film. When the stylus tip scans across the step, it accurately measures the height difference.
In our measurements we used a KLA Tencor P-16+ Profilometer. Several measurements were taken all along the step between the substrate and the deposited thin film. The step is done on the sides of the sample. To compute the thickness we took the mean value of all the measurements with its corresponding standard deviation as the uncertainty.

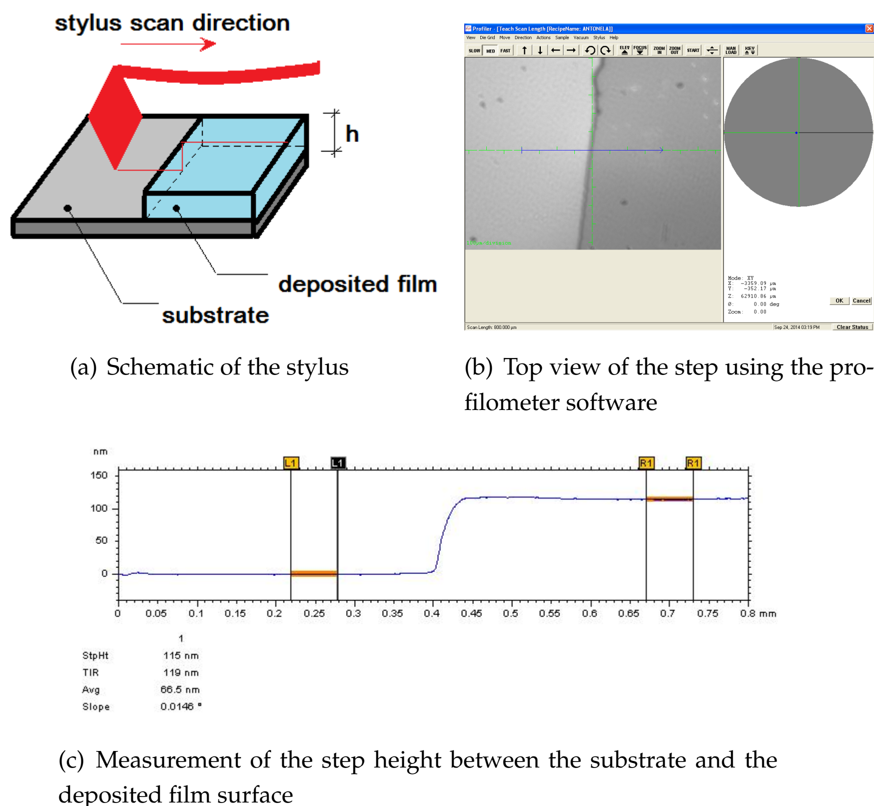


(a) Schematic of the stylus

(b) Top view of the step using the profilometer software

(c) Measurement of the step height between the substrate and the deposited film surface

**Figure 4.1:** Stylus profilometer technique to measure film thickness

### 4.2.3 Spectral Ellipsometry

Ellipsometry is an optical technique that characterises light reflected or transmitted from a sample. In particular, it measures the change in polarization of the light after interacting with the sample. Ellipsometry can measure simultaneously the amplitude ratio $\Psi$ and phase difference $\Delta$ of the polarization components of the light. The sensitivity in the phase difference measurements reflects an interferometric effect between the light reflected from the first and the second interface presented in a layer, allowing to determination of the thickness of the layer [41]. Spectral ellipsometry measures ($\Psi$, $\Delta$) spectra by changing the photon energy (or wavelength) of the incident light. In general, the measurements are carried out in the ultraviolet/visible spectral range, and thicknesses can be measured in the range of a few nanometers up to several microns with high sensitivity ( 0.1 Å) [42]. The angle of incidence is chosen to optimize the sensitivity during the measurements, and it varies depending on the optical constants of the material. To interpret and analyse the measured results of absolute ($\Psi$, $\Delta$) values, an optical model is required. From spectral ellipsometry data analysis, many physical properties can be deduced. The optical properties and the thickness of the sample can be determined. The technique is very sensitive, non-destructive, contactless and requires no sample preparation. In Figure 4.2 a schematic of the typical and main parts

of a spectroscopic ellipsometer is shown. These are a light source, a polarizer, a quarter wave plate, the detector and an analyzer.

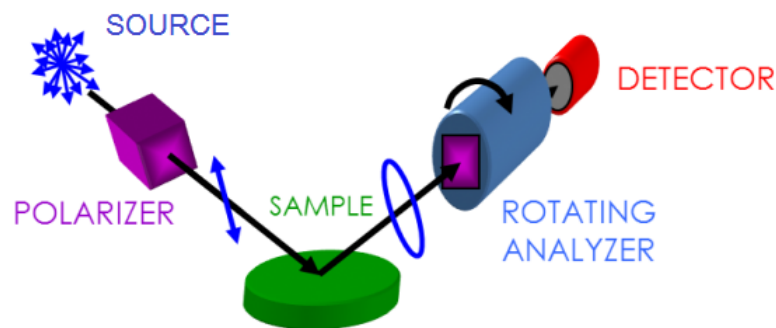


**Figure 4.2:** Schematic of the typical and main parts of a spectroscopic ellipsometer [43].

For these measurements we used a J. A. Woollam Co. VASE spectroscopic ellipsometer [44] acquiring ellipsometry quantities $\Psi$ and $\Delta$ at three different angles of incidence $65^o$, $70^o$, and $75^o$, in the wavelength range 250 to 1700 nm. The measurement is done in the center of the sample; the results from the simulations are meaningful in the area investigated by the instrument (a few square mm). The thickness results obtained with both techniques (profilometry and ellipsometry) agree within 1 nm for all the samples. This gives us an indication of a uniform deposition along the area of the films.

## 4.3 Atomic Force Microscopy (AFM)

The concepts of the Atomic Force Microscopy technique are essentially the same as in the profilometer, but with a great improvement in sensitivity and resolution. A critical part of the atomic force microscope is a micromachined cantilever, which is fixed on one side and with a sharp tip integrated on the other. The sharp tip is brought close to the sample's surface and rasters across a selected area. The flexible cantilever measures the forces between the the tip and the surface. The cantilever is able to convert the atomic attractive/repulsive forces between the atoms of the tip and the sample's surface into deflections of the cantilever. These deflections are monitored, quantified and converted into an electrical signal that reproduces the sample's topography as an image. The deflection of the cantilever is measured using a laser beam that is reflected from the back of the cantilever into a Position Sensitive Photo Detector (PSPD). In this way a small change in the bending angle of the cantilever is converted into a large change in the position of the reflected laser beam spot on the detector. The sample is located on a tube-shape scanner that moves it in both vertical (z) and horizontal (x-y) directions. Thus, the tip scans the sample while the PSPD signal is used as a feedback loop to

control the z motion of the scanner as the cantilever goes over the sample surface [45]. The basic configuration of an atomic force microscope is shown in Figure 4.3.

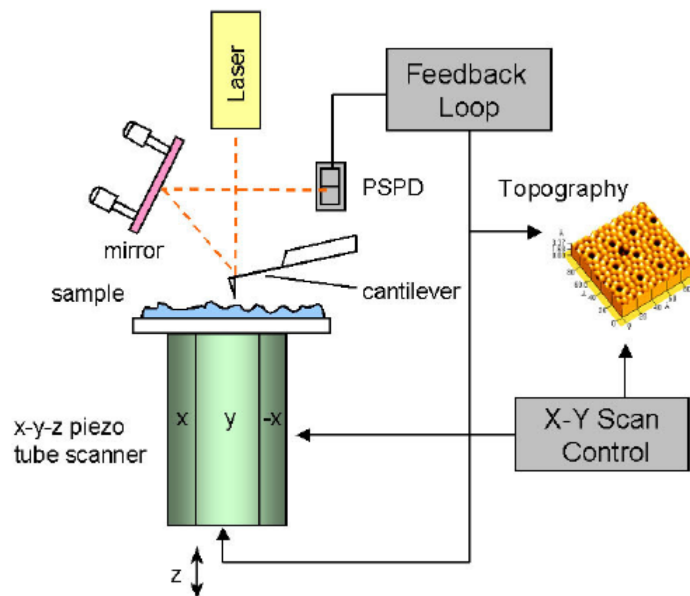


**Figure 4.3:** Basic configuration of an Atomic Force Microscope [45].

An atomic force microscope can work in different modes depending on the motion of the tip. These are contact mode, tapping mode and non-contact mode, schematically illustrated in Figure 4.4. In the contact mode the feedback signal is generated by a static tip deflection that rasters the sample in contact with its surface. In tapping mode, an external oscillation is applied to the cantilever, making it oscillate at its resonance frequency (or close to it). The amplitude, phase and resonance frequency of the cantilever are then modified by the interaction forces between the sample's surface and the tip. The changes in the oscillations are used to provide information of the topography of the surface. In non-contact mode the tip is oscillating as in tapping mode but does not touch the surface. Instead, oscillates a few nanometers above and the frequancy is modulated by van der Waals forces and other long range forces acting over the surface [46]. Non-contact mode extends the life of the tip avoiding degradation effects in both the tip and the sample. The atomic force microscope operates well in ambient air or in a liquid environment, making it an interesting technique to study biological systems, insulators, polymers and semiconductor materials.
In this research, the study of the surface morphology of each sample was carried out with a Park System XE-series Atomic Force Microscope. Measurements presented in this work were performed in a non-contact mode and in ambient air using a high resolution probe with a typical diamond-like 1 nm radius spike tip. The scanned area was of 2x2 $\mu$m$^2$ and the images were digitized into 256x256 pixels. The Root-Mean-Square (RMS) and average (Ra) surface roughness were determined using the XEI data

analysis software.

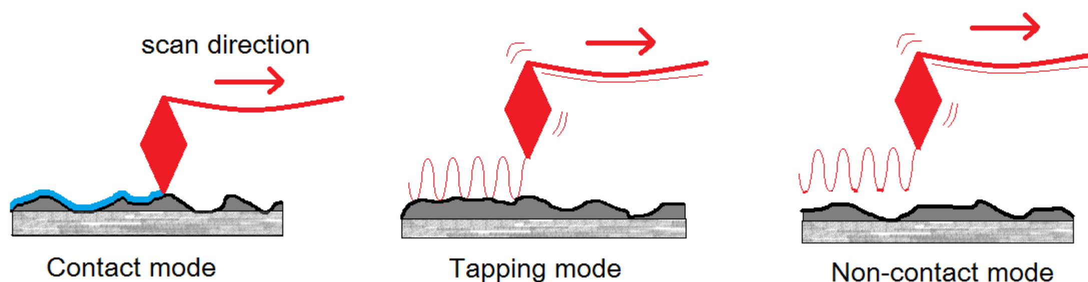


**Figure 4.4:** Atomic Force Microscope working modes

## 4.4 X-ray Photoelectron Spectroscopy (XPS)

The XPS technique is based on the bombarding of the sample surface with X-rays photons with energy $hv$, producing the ejection of electrons from a core level. This is known as the *photoelectric effect* and the emitted electrons are called *photoelectrons* [47]. The energy of these photoelectrons is received and analyzed by an electron spectrometer, presenting the data as an intensity (counts) *vs.* electron energy graph.
The spectrometer experimentally measures the kinetic energy ($E_K$) of the electrons emitted, which is dependent on the photon energy of the X-rays bombarding the sample. Thus, this is not a property of the material. On the other hand, the *binding energy* of the electrons ($E_B$) is the value that identifies the electrons in terms of the atomic level and parent element. These important parameters of the XPS technique are related by:

$$E_B = hv - E_K - W \tag{4.1}$$

where $E_K$ is the kinetic energy of the emitted electron, $hv$ is the energy of the incident photon and W is the spectrometer work function. The quantities on the right hand side of Equation 4.1 are already known or can be measured, and so it is possible to work out in a simple way the binding energy of the photoelectrons. In Figure 4.5 a schematic of the photoemission process is shown. Here, an electron located on the K shell is ejected from the atom, i.e. a 1s photoelectron.

In this manner, the electrons with $E_B$ lower than the X-ray photon energy that are excited and ejected without energy loss will manifest as peaks on the spectrum. Hence, the photoelectron spectrum reproduces the electronic structure of an element in a very accurate way. Some electrons will escape suffering energy loss (inelastic scattering) and will only contribute to the background noise of the spectrum. Once the atom is ionized undergoes a relaxation either by X-ray photon emission (X-ray fluorescence) or *Auger* electron emission. Generally the incident X-rays penetrate approximately 1$\mu$m into the sample, but only photoelectrons from the uppermost ≈10 nm of the sample

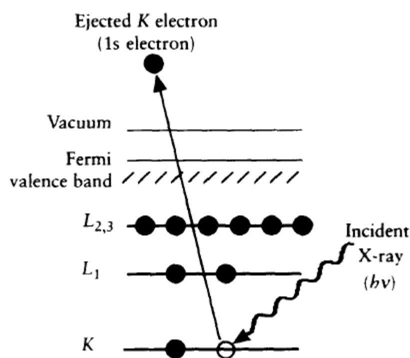


**Figure 4.5:** Schematic of the photoemission process that occurs on the XPS technique. The atom is photoionized after a 1s electron is ejected [47].

are able to elastically escape for XPS analysis [48], resulting in a very sensitive surface characterisation technique. The spectrometer works under ultra-high vacuum (UHV) to avoid contamination on the sample surface and collisions between gas molecules and low energy electrons. In this work, photoemission data were obtained in a custom designed UHV system equipped with a VG MK II Escalab electron analyzer, working at a base pressure of $10^{-9}$mbar, at room temperature, with a non monochromatized Mg K$\alpha$ X-ray source (1253.6 eV).
The XPS technique has the ability to identify the elements present on the sample and also their chemical state. To achieve a qualitative compositional analysis, a survey spectra (or wide scan) is taken over a wide range of binding energies. Usually, a low energy resolution is sufficient to record the photoelectron lines associated to each element present in the analysis. An example of this is shown in Figure 4.6$(a)$ for a carbon contaminated $TiO_2$ sample, where three major peaks are clearly distinguishable, associated to C1s, Ti 2p and O1s atomic transitions. The chemical composition can be derived from the relative intensities of the observed lines. Furthermore, to evaluate the chemical state of the sample, the survey is followed by a high resolution scan around each element peak of interest (Figure 4.6$(b)$). These high resolution acquisitions are analysed as a set of fitted peaks that are associated with different chemical shifts. The chemical environment of an atom affects its ground state energy and the binding energy of the electrons in the atom. The change generated in the electron's binding energy with respect to the pure element is what we refer to as a chemical shift.

## 4.5 Soft X-rays and Extreme Ultraviolet (EUV) reflectance

The optical characterisation of the thin film and bilayer samples was done by means of reflectance measurements. The reflectance was measured at two different facilities and applying different modes at each one. The first set of experiments was carried out at the Bending magnet for Emission, Absorption and Reflectivity beamline (BEAR)

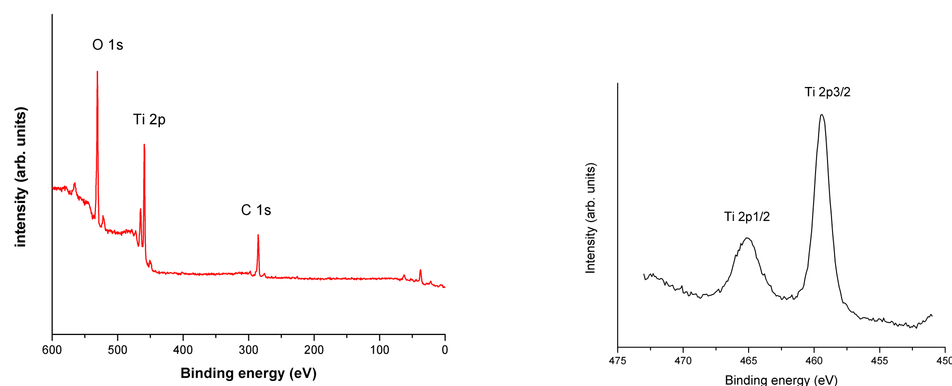


(a) Typical survey XPS spectrum of a carbon contaminated $TiO_2$ sample (b) Ti 2p region with a higher resolution energy scan

**Figure 4.6:** XPS electron spectra of a $TiO_2$ sample

of synchrotron ELETTRA located at Trieste, Italy. At this facility, we mainly performed measurements of reflectance *vs.* incidence angles at different photon energies in the soft X-ray and EUV spectral ranges, while the second set of experiments was performed on a compact self-referencing grazing incidence reflectometer, developed at the University College Dublin School of Physics laboratory. The reflectometer works in the water window spectral range (2-5 nm) and is based on a laser produced plasma source. With it, we took reflectance *vs.* energy measurements. These two facilities along with the applied technique, will be explained separately and in more depth in Chapters 5 and 6. As we will later describe, these experimental measurements allowed us to characterise the deposited coatings and to obtain the optical constants of the material under study. The reflectance of a surface is calculated by taking the ratio between the reflected intensity and the incident intensity. In this research, we will concentrate our study on the *specular reflection* rather than the possible scattered radiation reflected into a broad range of angles.

# Chapter 5

# Synchrotron reflectance measurements, $TiO_2$ optical constants determination and complementary film characterisation.

In this chapter we describe how the optical constants of titanium dioxide ($TiO_2$) were experimentally determined at energies in the EUV and soft X-ray spectral regions, from 25.5 to 612 eV. by measuring angle-dependent reflectance of amorphous $TiO_2$ thin films with synchrotron radiation at the BEAR beamline of Synchrotron ELETTRA. The experimental reflectance profiles were fitted to the Fresnel equations using a genetic algorithm applied to a least-square curve fitting method, obtaining values for $\delta$ and $\beta$. We compare our measurements with tabulated data. Complete films characterisation have been carried out with structural (XRD, ellipsometry and profilometry), compositional (XPS) and morphological (AFM) analyses.

## 5.1 Introduction

As discussed in Chapter 2, the optical properties of a material are described by its energy dependent complex index of refraction,

$$\mathbf{n} = 1 - \delta + i\beta \tag{5.1}$$

where $\delta$ and $\beta$ are known as the optical constants and they account for the dispersion and the absorption of the material, respectively [49]. To understand and estimate the optical response of a material when interacting with an incident electromagnetic wave it is necessary to have knowledge and accurate information on the refractive index, which ultimately opens the possibility of designing and improving optical devices. For many materials, there is still a great lack of experimental data for the optical

constants in the extreme ultraviolet (EUV) and soft X-ray wavelength spectral regions, therefore we must rely on calculated values. Henke *et al.* [50] has made available a semiempirical data base of optical constants that mostly rely on transmittance measurements and theoretical calculations for the absorption coefficient, while the dispersion coefficient or real part of the index of refraction is calculated using the Kramers-Kronig relations. Furthermore, when it comes to compound materials, the calculation is made by averaging the atomic scattering factors of each element present and weighting them depending on the stoichiometry of the compound. The calculation is based on a model where condensed matter is treated as a set of atoms not interacting with each other. This theoretical assumption is acceptable in energies far from absorption edges of the elements involved, but for energies surrounding these edges the chemical bonds have a strong influence on the behaviour of matter and frequently calculated values of the optical constants disagree with experimental responses [50] [51] [52].
We present here experimental values of both optical constants ($\delta$ and $\beta$) for $TiO_2$ in the EUV and soft X-ray, to our knowledge is the first such measurement realized.
We deposited $TiO_2$ thin films of different thicknesses on Si (100) polished wafers using the e-beam evaporation technique and characterised them measuring film thickness by spectroscopic ellipsometry and profilometry, film structure with XRD, thin film roughness *via* AFM and analyzing chemical composition with XPS.
Although various methods can be used to determine the optical constants ($\delta$ and $\beta$) of a material [53], in this work we chose the method known as "angle-dependent reflectance", because it allows us to measure experimentally both optical constants and also sample preparation was relatively simple compared to other methods, such as transmission measurements [54]. We have measured the reflectance as a function of the incident angle of the $TiO_2$ thin films, and derived $\delta$ and $\beta$ by fitting the experimental curves with calculated curves. The fitting procedure was carried out using a genetic algorithm applied to a least-square curve fitting method available on the IMD v5.0 software [31] [55]. Independently we have measured film thicknesses and film surface roughness, as mentioned before, to incorporate them as known fitting parameters and reduce uncertainty in the derivation of the optical constants. We describe a rigorous approach to improve the optical model, optimizing our calculations and fitting results significantly.

## 5.2 Sample characterisation

### 5.2.1 Thickness, surface roughness and structure.

The samples under study in this chapter are three amorphous $TiO_2$ thin films of different thicknesses, grown with electron-beam evaporation as described in Section 3.4.2. The thicknesses and surface roughness were measured and the values obtained are shown on Table 5.1.

| Sample ID | SE thickness (nm) | Profilometry thickness (nm) | RMS (nm) | Ra (nm) |
|---|---|---|---|---|
| Eb1 | $22.7 \pm 0.1$ | $21.7 \pm 2.2$ | $0.37 \pm 0.01$ | $0.29 \pm 0.01$ |
| Eb2 | $48.5 \pm 0.1$ | $48.0 \pm 3.7$ | $0.59 \pm 0.05$ | $0.43 \pm 0.02$ |
| Eb3 | $102.9 \pm 0.1$ | $102.0 \pm 0.8$ | $0.69 \pm 0.02$ | $0.54 \pm 0.02$ |

**Table 5.1:** Film thickness and surface roughness values (SE=Spectroscopic Ellipsometry).

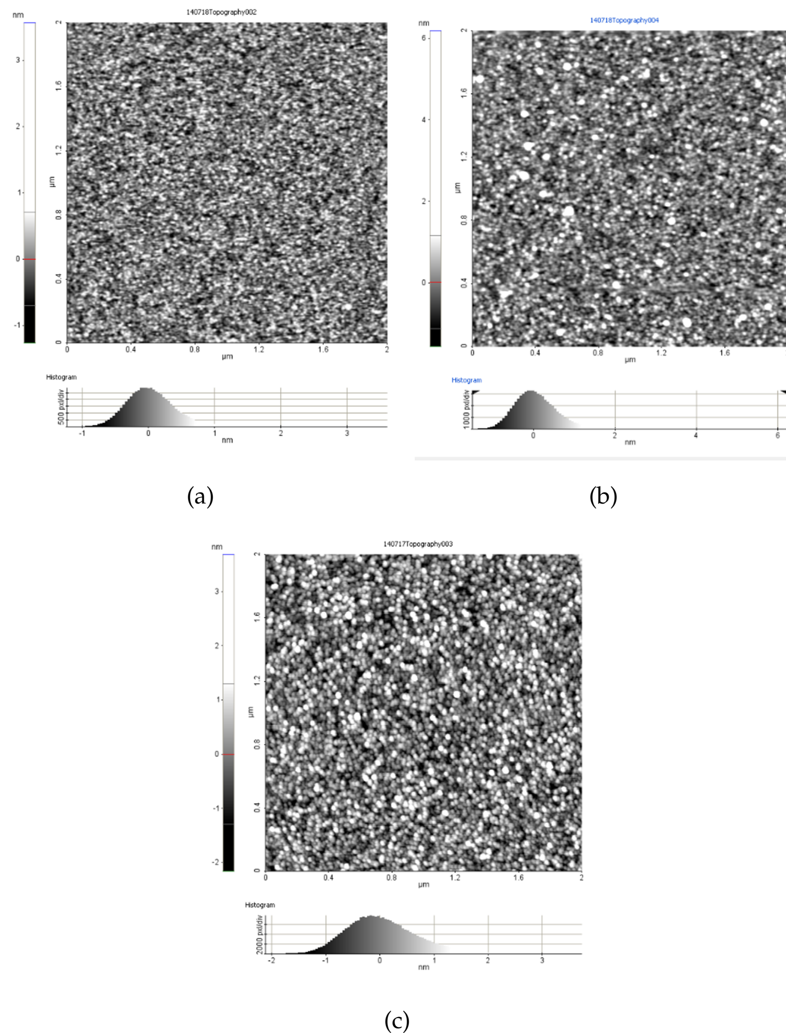

**Figure 5.1:** Two dimensional AFM images of the TiO2 thin film surfaces of (a) sample Eb1, (b) sample Eb2 and (c) sample Eb3.

The study of the surface morphology of each sample was carried out with an AFM in non-contact mode and in ambient air. The 2D images shown in Figure 5.1, represent a scanned area on each sample of 2x2 $\mu m^2$ and digitized into 256x256 pixels. The Root-Mean-Square (RMS) and average (Ra) surface roughness were determined, obtaining roughness values of less than 7 Å for all the samples. It is also observed that under these conditions of deposition, and for this range of thicknesses, the surface roughness

increased with increasing thickness of the deposited $TiO_2$ thin layer.
The thickness measurements (profilometry and SE) taken at two different points of the sample (edge and center, respectively) agree within 1 nm for all the samples. This suggests a uniform deposition.
Furthermore, XRD measurements were performed on the samples to analyse the film structure. Only broad curves and no peaks were shown on the XRD patters, revealing amorphous $TiO_2$ in all the three samples.

### 5.2.2 Chemical composition

The chemical composition of the films was investigated with X-ray photoelectron spectroscopy (XPS) measurements. Photoemission data was obtained in a custom designed UHV system equipped with a VG MK II Escalab electron analyzer, working at a base pressure of $10^{-9}$ mbar. Core level photoemission spectra (C 1s, Ti 2p and O 1s regions) were collected in a $90^o$ emission angle achieving an analysis depth of approximately 6 nm from the surface. Measurements were done at room temperature, with a non monochromatized Mg K X-ray source (1253.6 eV) and using 0.1 eV steps, 0.5 s collection time and 20 eV pass energy. The binding energies (BE) were referenced to the C 1s peak at 284.5 eV.
The survey scans were performed over a large range of binding energies to detect the elements present on the sample. As shown in Figure 5.2, the dominant signals are from titanium, oxygen and carbon.

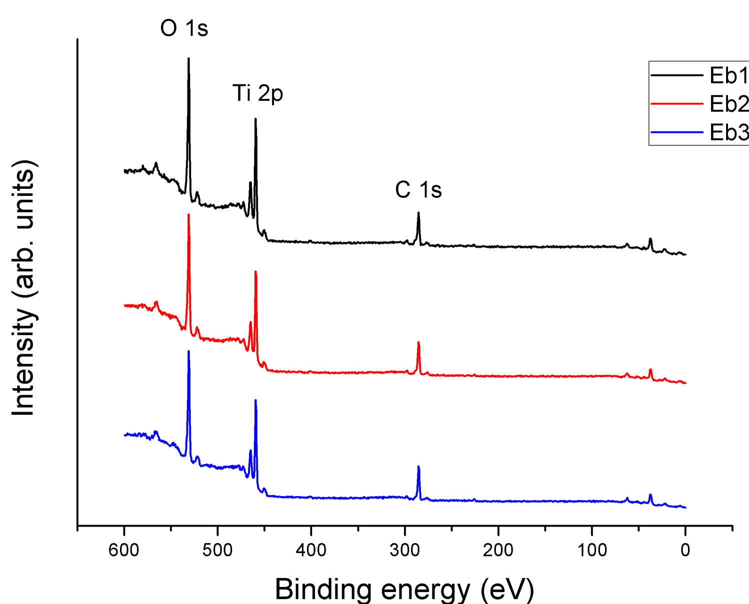


**Figure 5.2:** XPS survey spectra from the $TiO_2$ samples.

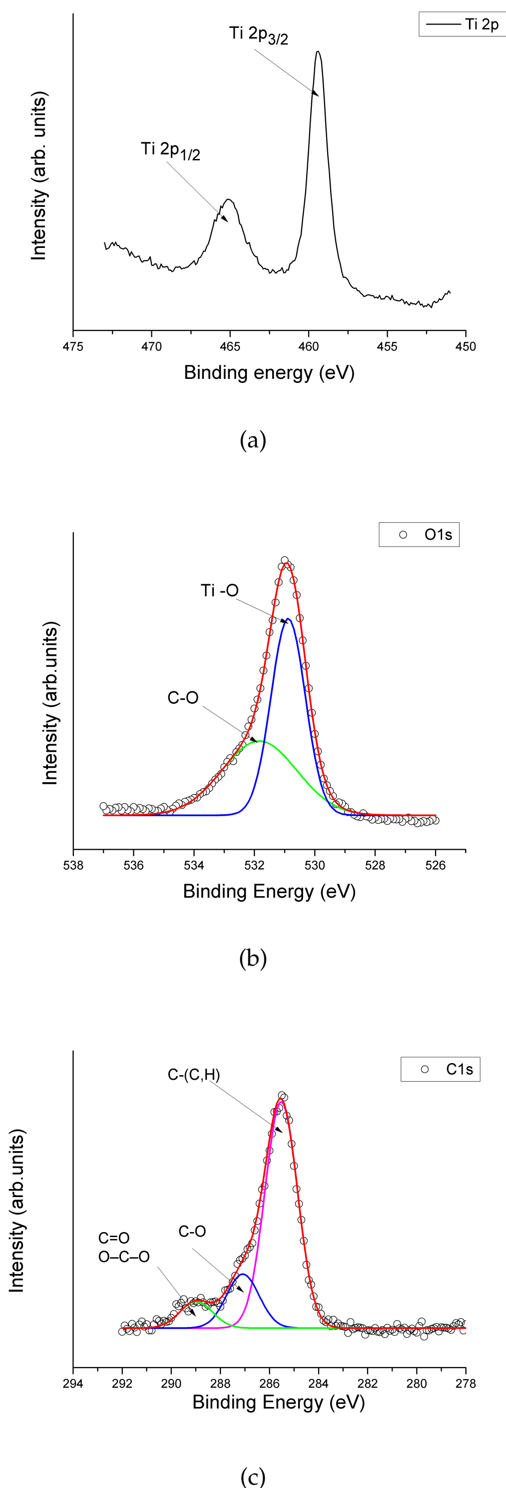


**Figure 5.3:** XPS high resolution energy scans of the samples on the (a) Ti 2p, (b) O 1s and (c) C 1s regions. The colored curves represent how the main peaks are deconvolved.

In Figure 5.3 the representative examples of the high resolution energy scans acquired over a narrow range of the C 1s, Ti 2p and O 1s regions of the spectra, on the

three samples, are shown. Figure 5.3(a) shows the two major peaks (doublet) of Ti $2p_{3/2}$ and Ti $2p_{1/2}$, found at binding energies of 459.4 and 465.1 eV, respectivly. The binding energy values and the separation between the peaks of 5.7eV are characteristics of $TiO_2$ [56] [57]. No suboxides were observed, confirming the formation of $TiO_2$.
The O 1s peak, shown in Figure 5.3(b), was deconvoluted into two peaks. The major peak centred at 530.9 eV was attributed to oxygen chemically bonded to Ti (Ti-O-Ti), while the second weaker peak may be attributed to oxygen chemically bonded to contamination carbon (C-O) [58]. The XPS high resolution scan around the C1s peak (Figure 5.3 (c)), can be deconvoluted into three peaks. The mean one, located at 285.5 eV, can be attributed to adventitious carbon and hydrocarbon (C-C, C-H) giving the main contribution to the C1s peak. A second and third small shoulder attributed to different oxidized forms of carbon, are centred at 287.1 eV and 288.9 eV, respectively [59]. The carbon may be attributed to surface contamination, which most probably originated when the samples were exposed to the atmosphere.
The titanium: oxygen (Ti:O) stoichiometry was calculated from the areas of the high-resolution scans using Igor Pro XPS software. The Ti:O atomic ratio calculated for all the samples is 1:2. There are no significant differences in chemical composition of the samples [60].

## 5.3 Reflectance measurements at BEAR

### 5.3.1 Instrument and specifications

Reflectance measurements were performed at the Bending magnet for Emission, Absorption and Reflectivity beamline (BEAR) of Synchrotron ELETTRA. It is a 2/2.4 GeV third generation synchrotron based on a bending magnet as a source, with an energy range of 2.8-1600 eV and a spectral resolution $\lambda/\Delta\lambda \geq 3000$ over the whole spectral range. It has a typical final beam spot size of the order of 30x100 $\mu m^2$ (vertical x horizontal), and elliptically polarized radiation with optional selection from linear to near circular polarization, all with good flux [61]. The beamline is mainly composed of an experimental chamber (or end chamber) were the reflectance measurements are performed, a preparation chamber suitable for *in situ* depositions and a transfer stage that allows to insert the samples and to move them from one chamber to the other. They are connected with each other and always work under UHV (base pressure $10^{-10}$ mbar).
Two of the three grating monochromators available at BEAR were selected depending on the energy region were the measurements were performed. The Grating of Normal Incidence Monochromator (GNIM) works at near normal incidence, it has 1200 lines/mm and was used to cover the energies included in the 2.8 - 45 eV range, with an exit vertical slit aperture set at 400 $\mu m$. The grazing incidence grating monochromator (G1200) has also 1200 lines/mm and it was used to cover the energies included in the 40 - 1600 eV energy range, with an exit vertical slit aperture set at 100 $\mu m$.

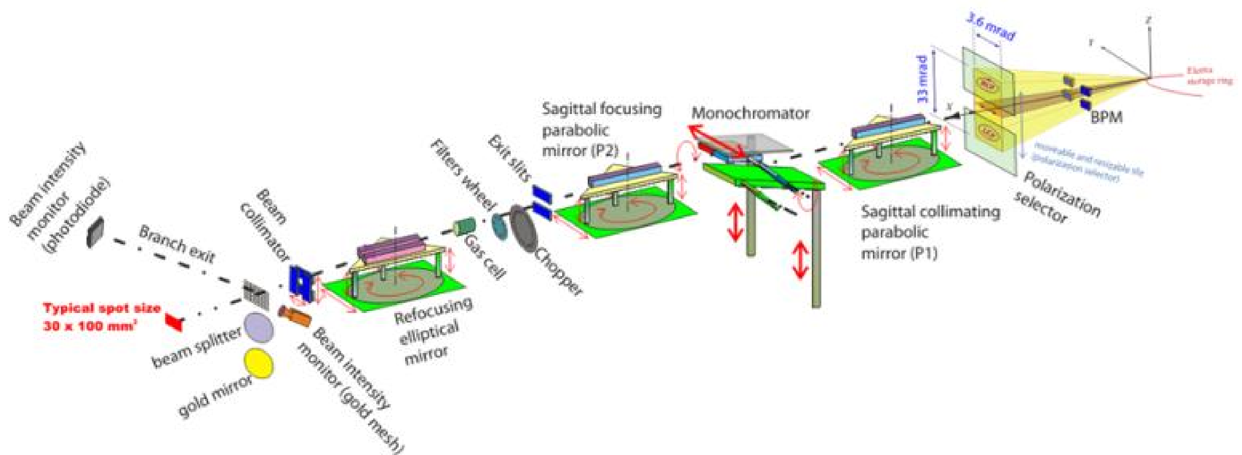


**Figure 5.4:** Schematic layout of the beamline and its optics [21]

In Figure 5.4 a schematic layout of the beamline is shown. A detailed description of its optical design will not be given here but it can be found in reference [61] and on the webpage of the facility [21]. To obtain high purity radiation, the higher diffraction order contribution is removed by alternatively selecting different filters (In, Al, Si, Ag, Sn) and proper monochromator deviation angles.
For our experiment, the experimental chamber was always set in the s-polarization orientation. The degree of polarization of light was set by the polarization selector, a variable aperture slit that we set at a standard aperture of $\pm$2mm, corresponding to $\pm$0.17 milliradians with respect to the synchrotron orbit plane. The degree of polarization of the radiation emitted from the BEAR beamline, in the energy range where all the measurements were performed, is known to be higher than 95% [21]. The polarization degree was experimentally measured at 100 eV, 285 eV and 650 eV for this configuration, obtaining values of 95%, 97% and 97%, the value 95% can be considered as a lower limit due to the properties of the bending magnet source. All the data were collected with a $\theta - 2\theta$ geometry using a photodiode as a detector. We performed s- polarized reflectance as a function of the grazing incidence angle on all the samples at fixed values of energies in the 25.5-612eV range, the grazing incidence angle ranges from $2^o$ to $85^o$ with a minimum step of $0.125^o$ and a maximum of $2^o$. For energies greater than 82.5eV, the maximum $\theta$ considered in the angle scans was between 12-$30^o$ grazing incidence angles, i.e. up to where the reflectance signal-to-noise ratio was significant.
Before entering the experimental chamber, the incident beam goes through a gold mesh that allows to monitor fluctuations in the photon flux and to register a reference signal (S). The absolute reflectance (R) of the samples was derived by calculating the ratio of the reflected to the incident beam intensity, both measured with the same detector, a silicon photodiode (model AXUV-100). To do so we first measured the radiation intensity of the direct beam arriving to the detector ($I_D$) and the reference signal of the direct beam ($I_{SD}$) in a period of 30 seconds. Then, we measured the reflected beam intensity

arriving to the detector ($I_R$) and the corresponding reference signal ($I_{SR}$) during the $\theta$ (or angle) scan.
A background noise (B) is determined for every step, always with all the valves of the chamber and the shutter closed (i.e. no beam radiation entering the chamber nor going through the mesh) we measured the radiation detected by the photodiode and the reference signal (mesh). The measurement process is shown in Figure 5.5, this is done for each photon energy selected. Finally R is determined by Equation 5.2 :

$$R = \frac{(I_R - B_R)/(I_{SR} - B_{SR})}{(I_D - B_D)/(I_{SD} - B_{SD})} \tag{5.2}$$

The experimental error in reflectance measurements is estimated to be of the order of 0.5%. Because the measurement process time is of the order of one half hour per energy position, only a single scan of energy *vs.* angle was performed.

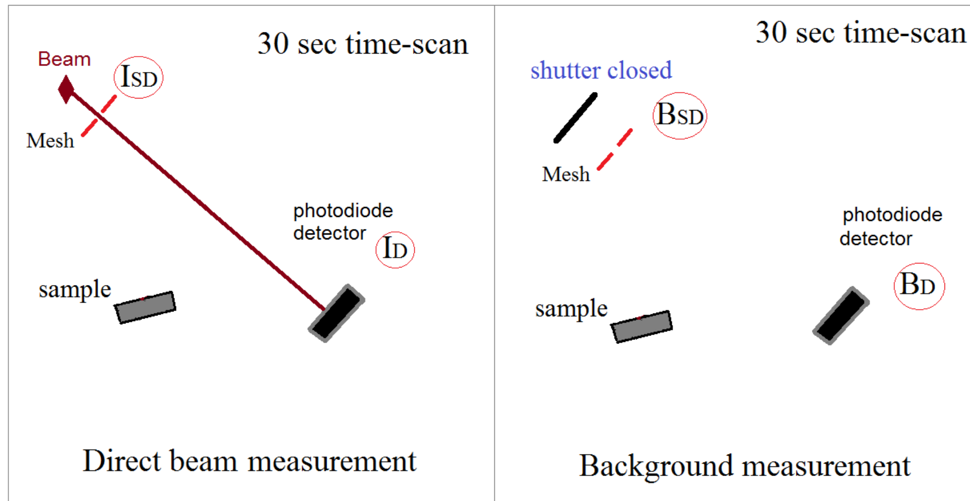


(a)

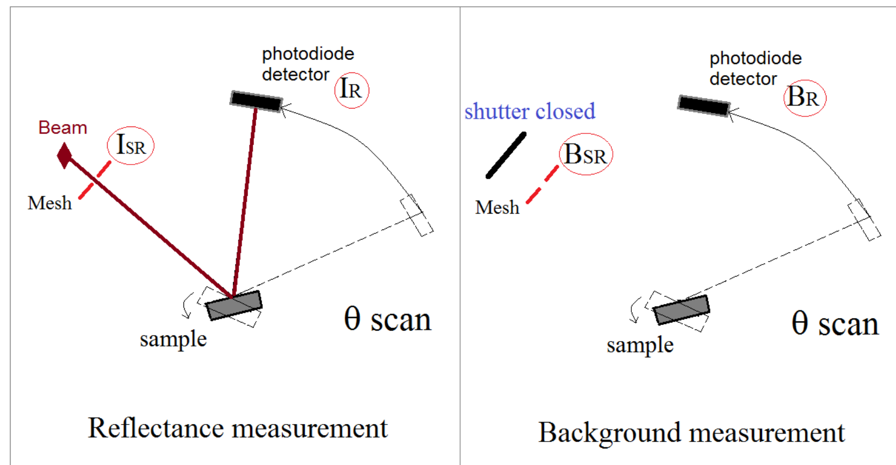


(b)

**Figure 5.5:** Measurement process at BEAR. Acquisition of (a)the direct beam and its background and (b) the reflected beam and its background.

## 5.4 Optical constants calculation

The behaviour of a plane electromagnetic wave incident at a perfectly smooth interface between two different materials is described by the Fresnel equations, where the amplitude reflection coefficient for s-polarization on an ideal interface ij is given by [62]:

$$r_{ij}^{s} = \frac{(\mathbf{n_i} cos\theta_i - \mathbf{n_j} cos\theta_j)}{(\mathbf{n_i} cos\theta_i + \mathbf{n_j} cos\theta_j)} \tag{5.3}$$

where $\mathbf{n}_i$ and $\mathbf{n}_j$ are the index of refraction of the two materials, $\theta_i$ is the incident angle and $\theta_j$ the refraction angle (determined from Snells law), both with respect to

the interface normal. The Fresnel equations assume a perfect boundary but in actual experience there is always, however minimal, surface roughness and interfacial roughness/diffuseness. Since we are working with photon energies in the soft X-ray and EUV range where these factors result in a significant reduction of the specular reflectance, we must include these effects in our analysis. In order to account for them, the reflection coefficient is multiplied by a correction factor where stochastic roughness is included with the so called *Névot-Croce* formalism described in Ref. [30]:

$$r_{ij}^{s*} = r_{ij}^{s} exp(-2q_i q_j \sigma^2) \tag{5.4}$$

where $\sigma$ is roughness, $q_i = 2\pi cos\theta_i/\lambda$ , j=i+1, and $\lambda$ the wavelength of light.

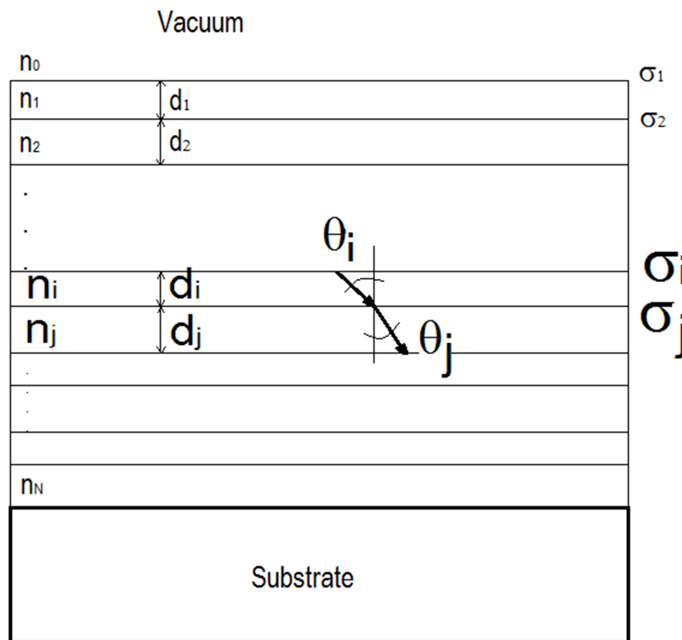


**Figure 5.6:** Schematic of a multilayer structure of N layers, where the ith layer has thickness $d_i$ , interfacial roughness/diffuseness $\sigma_i$, and index of refraction $\mathbf{n}_i$.

In our approach we considered more than one layer in our optical model. Figure 5.6 shows the general schematic for a multilayer structure of N layers of different materials. For a series of N layers with thickness $d_i$ , interfacial roughness/diffuseness $\sigma_i$, and index of refraction $\mathbf{n}_i$ for the ith layer, we calculate the net reflection coefficient of the ith layer, given by:

$$r_i = \frac{r_{ij} + r_j exp(2i\beta_i)}{1 + r_{ij} r_j exp(2i\beta_i)} \tag{5.5}$$

where $\beta_i = 2\pi/\lambda d_i \mathbf{n_i} cos\theta_i$, the reflection coefficients $r_{ij}$ are calculated from Equation 5.4, and $r_j$ is the net reflection coefficient of the jth interface. Thus, to calculate the total amplitude reflection coefficient (r) of the structure we apply Equation 5.5 recursively [31] as detailed in Section 2.2. We used tabulated optical constants for the Si substrate and we assumed vacuum as the ambient medium ($\mathbf{n}_0$=1). The reflectance R is simply $R=|r|^2$. We have measured the reflectance of the samples as a function of the angle of incidence, obtaining in this way experimental reflectance curves $R_s(\theta)$ for the different fixed photon energies. The approach to obtain the optical constants was done by fitting the experimental curves to calculated curves based on a defined optical model, using IMDs genetic algorithm [55] applied to a least-square curve fitting method where a figure-of-merit (FOM) is minimized:

$$FOM = \frac{\Sigma_{i=1}^{N} w(i) |lnR_i^{calc} - lnR_i^{meas}|^2}{\Sigma_{i=1}^{N} w(i)} \tag{5.6}$$

Here N refers to the number of measured data points, $R_i^{calc}$ is the calculated reflectance, $R_i^{meas}$ is the measured reflectance and w(i) represents a statistical weighting factor for each point.

## 5.5 Results and discussion

### 5.5.1 Optical constants of titanium dioxide ($TiO_2$)

When evaluating optical properties of a sample, we must first define an optical model on which we will base our simulations. In this work we started out considering the simplest one-layer model and progressively adding refinements in order to obtain the model that best described our problem. To represent this, we show in Figure 5.7 and 5.8 fitting results of the reflectance curve of sample Eb2 for energies of 612 eV and 310 eV. The first approximation was done by considering the sample as just a layer of $TiO_2$ on Si (one-layer model, $TiO_2$/Si), the next one takes into account a native oxide layer usually formed on the Si substrate of $SiO_2$ plus the $TiO_2$ layer (two-layer model, $TiO_2$/ $SiO_2$/Si) [63], and finally we included a contamination layer C formed when exposed to the ambient (three-layer model, C/ $TiO_2$/ $SiO_2$/Si). Figures 5.7 and 5.8 show that while introducing the native oxide may not affect the reflectance in a major way for E=310eV, it does significantly for E=612 eV. Moreover, the refinement introduced by the more complex model of three layers significantly improves the fittings at all energies; the effect of the substrate and the oxide layer is obviously more evident for samples

Eb1 and Eb2 than for the thicker sample Eb3. Thus, the three-layer model describes best our reflectance curves and we use it in our analysis.

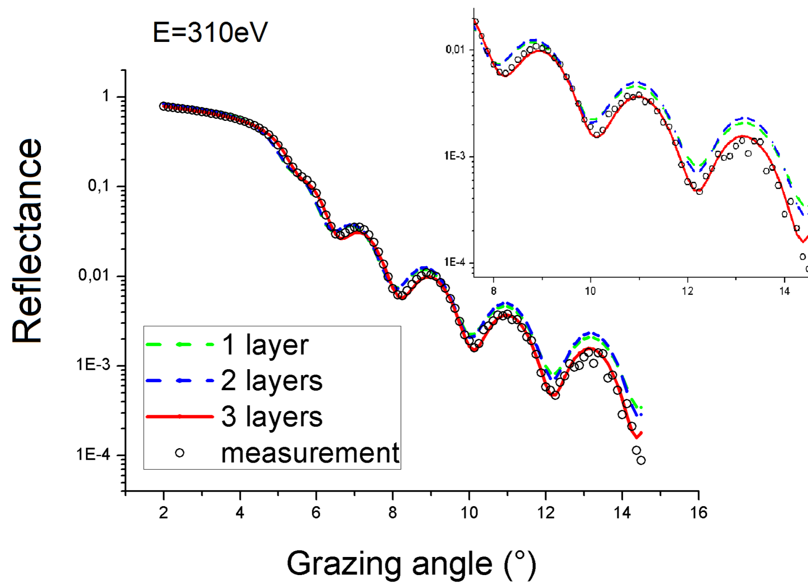


**Figure 5.7:** Reflectance measurement of sample Eb2 at E=310 eV with curve fittings considering a one-layer ($TiO_2$/Si), a two-layer ($TiO_2$/$SiO_2$/Si) and a three-layer model (C/$TiO_2$/$SiO_2$/Si). In the inset, the grazing angle range 8-14$^o$ is enhanced.

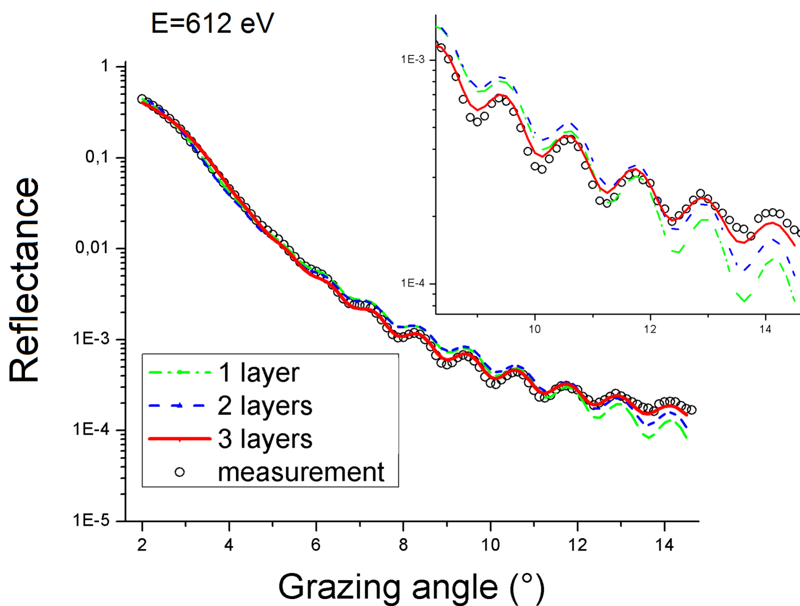


**Figure 5.8:** Reflectance measurement of sample Eb2 at E=612 eV with curve fittings considering a one-layer ($TiO_2$/Si), a two-layer ($TiO_2$/$SiO_2$/Si) and a three-layer model (C/$TiO_2$/$SiO_2$/Si). In the inset, the grazing angle range 8-14$^o$ is enhanced.

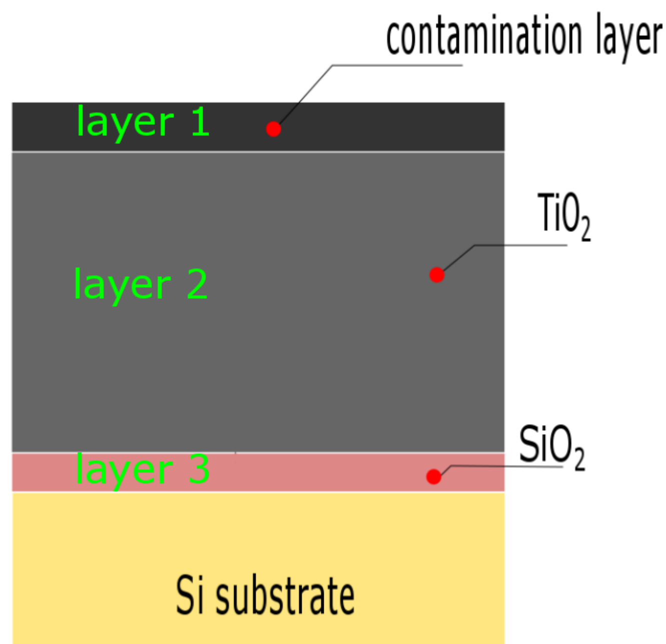


**Figure 5.9:** Schematic of the three-layer optical model (not in scale).

In Figure 5.9 a schematic of the three-layer optical model is shown.
Given that the reflectance-*vs.*-angle method is very sensitive to the state of the surface [53], it is absolutely essential to have as much information as possible on the surface to correctly model it. In our work, the surface roughness was measured on every sample and we have incorporated a contamination layer into the optical model after confirming its existence with XPS measurements. The fitting parameters in this first stage of the analysis were the thickness $d_i$ and roughness/diffuseness $\sigma_i$ of each layer, and the optical constants of the $TiO_2$ layer. (Note that in this work the value $\sigma_i$ represents the indistinguishable contribution of roughness and diffuseness at the interfaces, and we refer to it as "roughness/diffuseness" or just $\sigma_i$).
In a second stage, and to completely define our optical model, we performed a calculation of the $d_i$ and $\sigma_i$ of all layers. These parameters are not energy dependent [64]. We have first evaluated the smallest range of $d_i$ and $\sigma_i$ values that allow convergence of the fittings, accounting for the results at all energies. Then, we fixed these parameters at the average values. The number of adjustable parameters in the fitting is thus reduced, since the optical constants $\delta$ and $\beta$ of the $TiO_2$ layer and of the contamination layer are the only free parameters in the final analysis.
On all the samples the thickness of the $SiO_2$ oxide layer formed over the substrate was estimated to be ≈2 nm and the contamination layer to be ≈0.6 nm. The thicknesses obtained for the $TiO_2$ layer of each sample were in agreement with ellipsometry and

profilometer measurements. The roughness of the polished wafers we used as the substrates is specified to be approximately 0.25 nm, this value was incorporated into the optical model during the simulations.

Some of the measurements were carried out around the L and K edges of the elements present in the samples to observe their optical response. In general, we were able to obtain satisfactory fittings at all energies. Figure 5.10 and 5.11 are representative examples of the reflectance curves measured for all the samples, they respectively show the profiles obtained for samples Eb2 and Eb3 versus the grazing incidence angle along with the best fits, for some of the photon energies measured from 25.5 eV to 612 eV. Fittings were performed with the three-layer model, and the two sets of optical constants as the only adjustable parameters.

Uncertainties in derived fitting values have been estimated by checking how the 0.5% experimental error on the reflectance measurements can affect the fitting convergence. To do so, we added 0.5% to each experimental data point to generate a "higher" reflectance curve. This new curve is then fitted to determine new "higher" $\delta$ and $\beta$ values. The same process is performed to generate a "lower" curve by subtracting 0.5% to each reflectance data point, and is also fitted to determine new $\delta$ and $\beta$ values. The excursion of $\delta$ and $\beta$ from the original data fit is used as the uncertainty or error bar for each value [53].

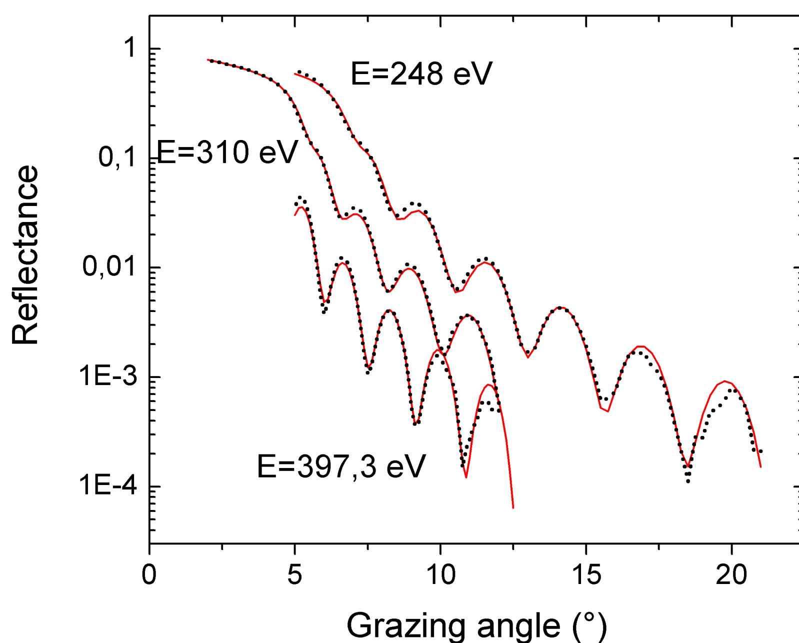


**Figure 5.10:** Reflectance curves (dotted lines) measured at energies E=248 eV, 310 eV and 397.3eV, and their respective best fit curves (continuous lines) for sample Eb2.

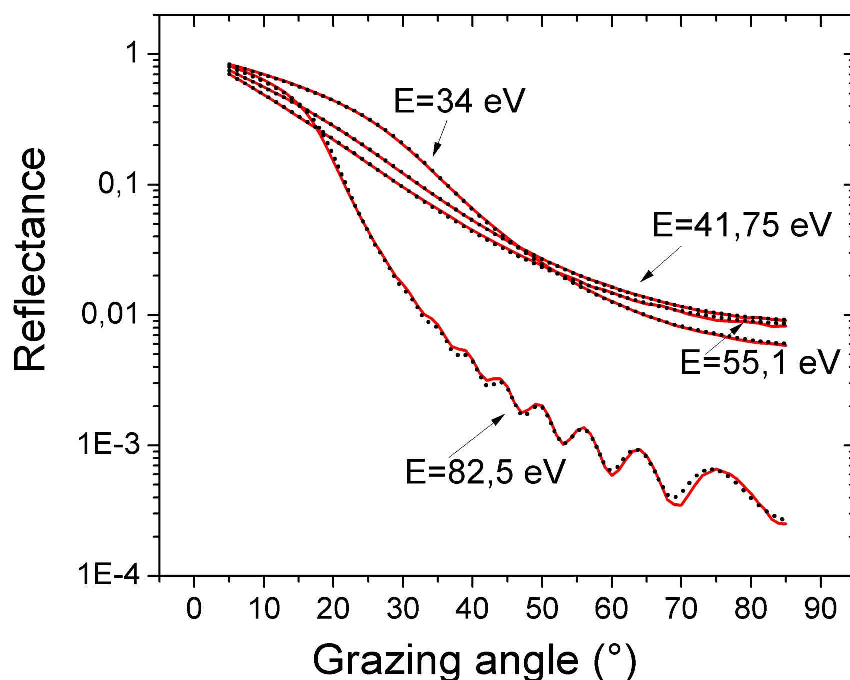


**Figure 5.11:** Reflectance curves (dotted lines) measured at energies E=34 eV, 41.75 eV, 55.1 eV and 82.5eV, and their respective best fit curves (continuous lines) for sample Eb3.

The optical constants obtained for all the samples show good agreement. Generally, the difference is 2% for the real and imaginary part, with a maximum difference of 6%. Table 5.2 shows the mean value of the optical constants obtained from the three samples with the estimated uncertainty given by their standard deviation. They are plotted in Figure 5.12 and 5.14 as dots, along with a close up of the Ti L edge region in Figure 5.13 and 5.15. They are compared with values computed from atomic scattering factors provided by Henke *et al.* [50] available at the Center for X-Ray Optics (CXRO) database [65]. For the sake of comparison with our measurements, the calculations were performed assuming a density of 3.7g/cm$^3$(presented as continuous lines on the figures).

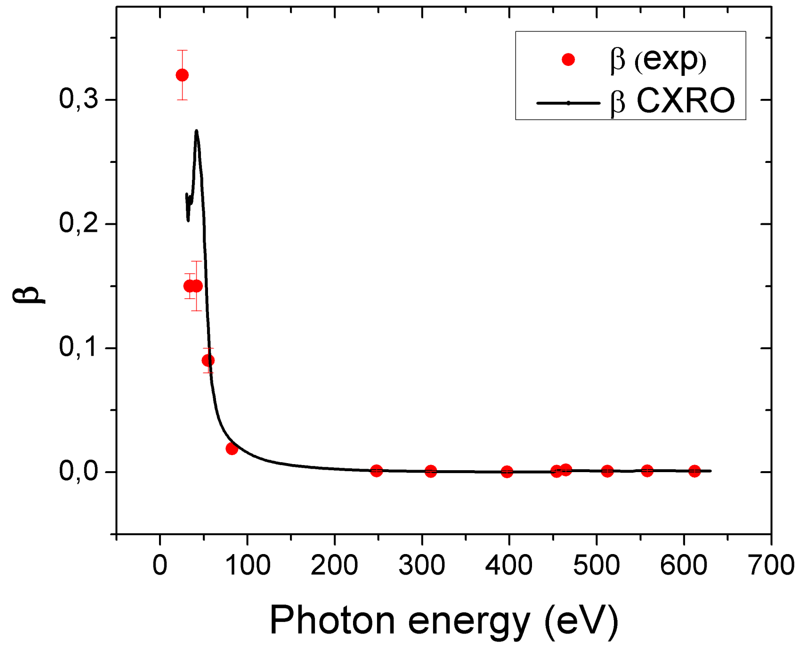


**Figure 5.12:** $TiO_2$ measured values of $\beta$ versus photon energy (dots) along with values from CXRO [65] (continuous line).

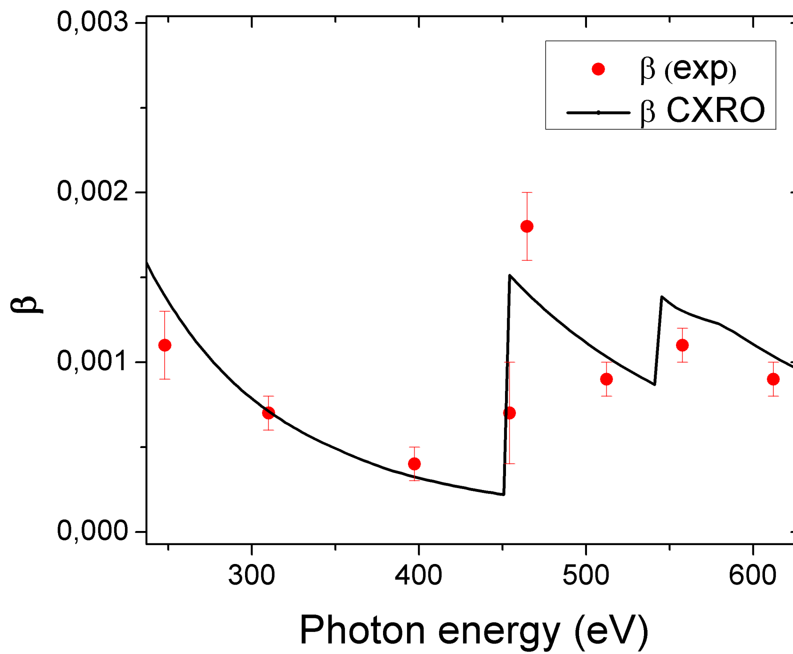


**Figure 5.13:** Close up of the Ti L edge zone. $TiO_2$ measured values of $\beta$ versus photon energy (dots) along with values from CXRO [65](continuous line).

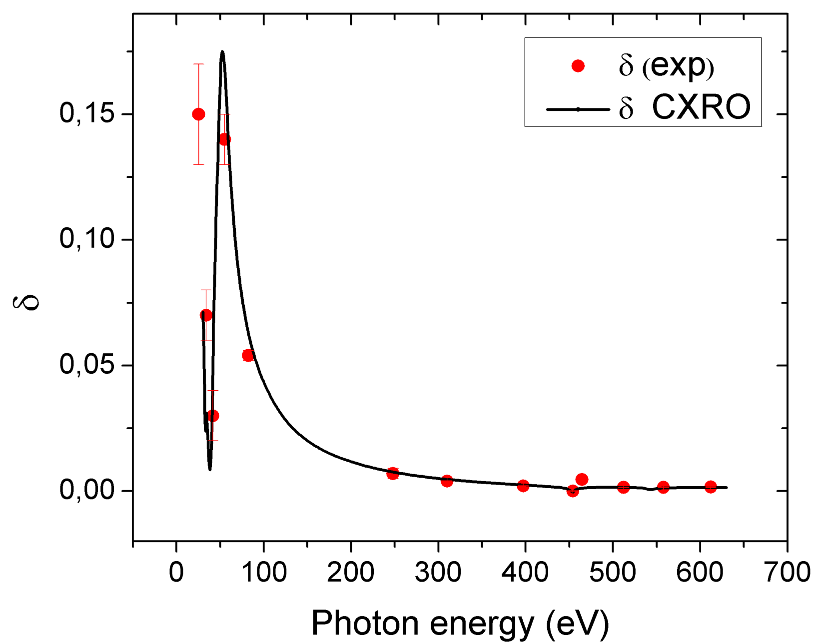


**Figure 5.14:** $TiO_2$ measured values of $\delta$ versus photon energy (dots) along with values from CXRO [65] (continuous line).

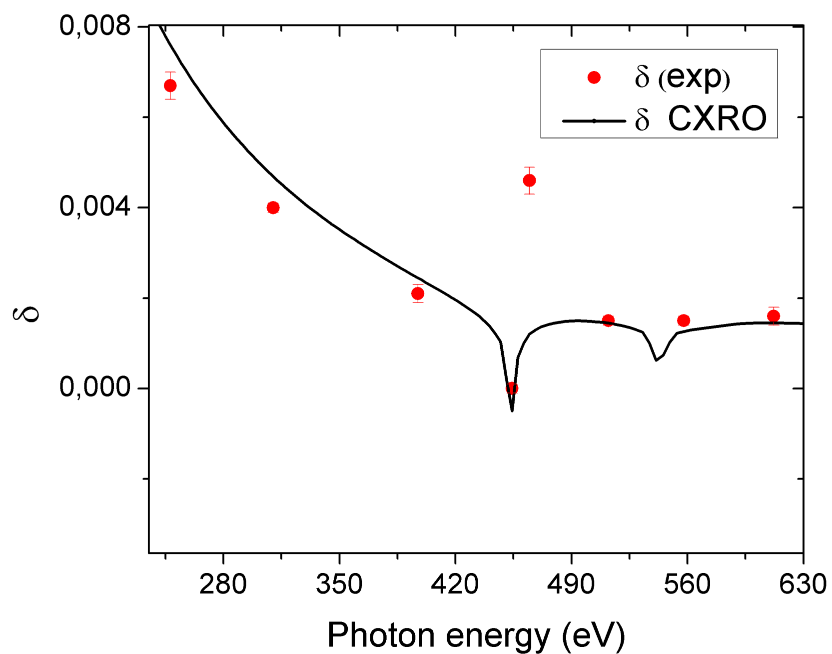


**Figure 5.15:** Close up of the Ti L edge zone. $TiO_2$ measured values of $\delta$ versus photon energy (dots) along with values from CXRO [65] (continuous line).

The accuracy in which the reflectance angle-dependent method can determine the optical constants has a dependency on the $\beta/\delta$ ratio value which is energy dependent [66]. This ratio relates to the shape of the reflectance curves; if $\beta/\delta$ is less than 1 the curves have a well-defined shoulder below a critical angle (see Figures 5.16). It can be calculated from $\theta_C = \sqrt{2\delta}$. This allows the fitting algorithm to be successful at working out $\beta$ and $\delta$ with little uncertainty. When $\beta/\delta$ approaches 1, the reflectance curves become exponential-like and the critical angle region is not distinguishable. For $\beta/\delta$ greater than 1 the optical constants uncertainty is not minimized.

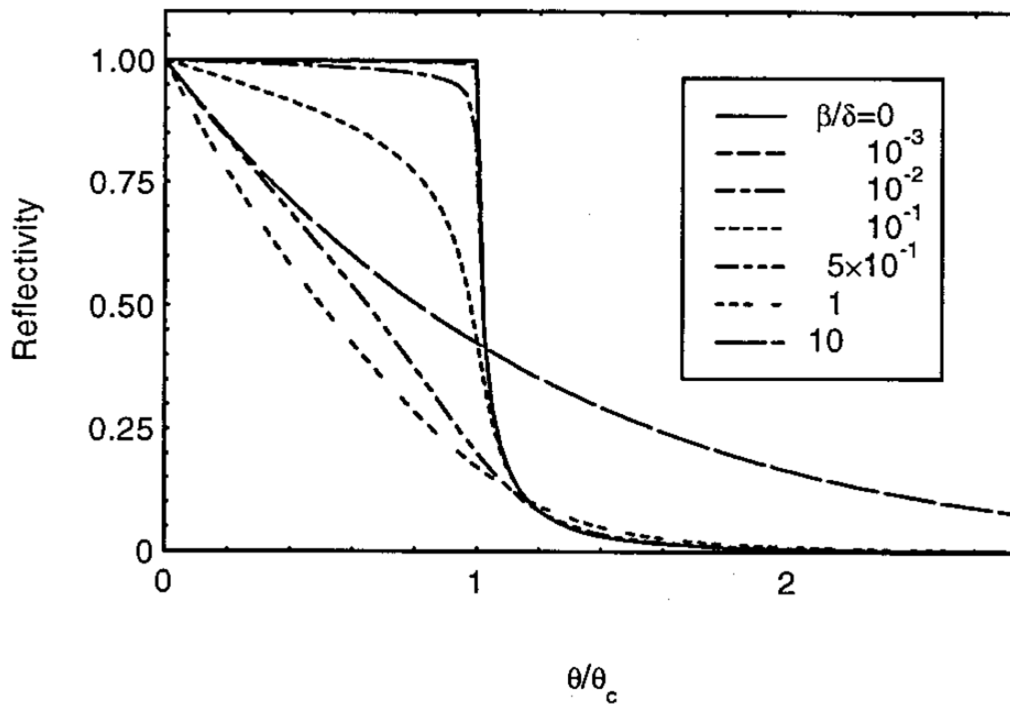


**Figure 5.16:** Calculated reflectance curves for s-polarized radiation. The grazing angle $\theta$ is normalized to the critical angle $\theta_C$ [66].

**Table 5.2:** Optical constants of $TiO_2$ derived from reflectance-vs-angle measurements, along with values computed from atomic scattering factors assuming the films density

| Energy (eV) | $\lambda$(nm) | $\delta$(exp)* | $\delta$ | $\beta$(exp)* | $\beta$ |
|---|---|---|---|---|---|
| 25.50 | 48.63 | 0.15(2) | n/a | 0.32(2) | n/a |
| 34.00 | 36.47 | 0.07(1) | 0.02 | 0.15(1) | 0.22 |
| 41.75 | 29.70 | 0.03(1) | 0.05 | 0.15(2) | 0.27 |
| 55.10 | 22.50 | 0.14(1) | 0.16 | 0.09(1) | 0.11 |
| 82.50 | 15.03 | 0.054(2) | 0.062 | 0.0019(1) | 0.024 |
| 248.00 | 5.00 | 0.0067(3) | 0.0076 | 0.0011(2) | 0.0013 |
| 310.00 | 4.00 | 0.0040(1) | 0.0046 | 0.0007(1) | 0.0007 |
| 379.30 | 3.12 | 0.0021(2) | 0.0024 | 0.0004(1) | 0.0003 |
| 454.20 | 2.73 | 0.0000(1) | 0.0000 | 0.0007(3) | 0.0015 |
| 464.64 | 2.67 | 0.0046(3) | 0.0011 | 0.0018(2) | 0.0014 |
| 512.25 | 2.42 | 0.0015(1) | 0.0014 | 0.0009(1) | 0.0011 |
| 557.70 | 2.22 | 0.0015(1) | 0.0012 | 0.0011(1) | 0.0013 |
| 612.00 | 2.03 | 0.0016(2) | 0.0014 | 0.0009(1) | 0.0011 |

*The estimated error in our experimental values of $\delta$ and $\beta$ are given in parentheses for the last significant digit.

### 5.5.2 Optical response near the soft X-ray absorption edge of $TiO_2$ and study of buried interlayers

Looking at Figure 5.13 and 5.15, the larger disagreement with the CRXO data is for E=464.64 eV. As stated in previous lines, the values computed by Henke *et al.* [50], are calculated by averaging the atomic scattering factors of each element present and weighting them depending on the stoichiometry of the compund. The calculation is based on a model where condensed matter is treated as a set of atoms not interacting with each other. This assumption is acceptable in energies far from absorption edges of the elements involved, but for energies surrounding these edges, the chemical bonds have a strong influence on the behaviour of matter and calculated values of the optical constants frequently disagree with experimental responses [50] [51] [52].
The reflectance measurement at E=454.2 eV is also done very near the Ti L3 edge, where an abrupt change of the optical constant is expected [50] and so the sensitivity to the atoms configuration or chemical environment is significantly enhanced. At this energy we encountered difficulties to arrive at a good fitting using the three-layer model. The reflectance at this particular near edge energy is very sensitive to interlayer formation on the interfaces [67] [68], hence the effect of the unavoidable interface formation due to the growth process had to be considered in the optical model.
As mentioned in previous paragraphs, we identified a carbon-like surface contamination layer with XPS, and its thickness was estimated to be $\approx$0.6 nm from reflectance measurements. Thus we could expect some intermixing and compound formation at

this first interface. On the other hand, a native $SiO_2$ oxide layer over the substrate was previously estimated to be $\approx 2$ nm thickness from reflectance measurements. Likewise, a second interlayer of Ti-O-Si mixed oxide formation could be expected between the $SiO_2$ layer and the $TiO_2$ deposited layer, other than the formation of a single oxide phase [69] [70].

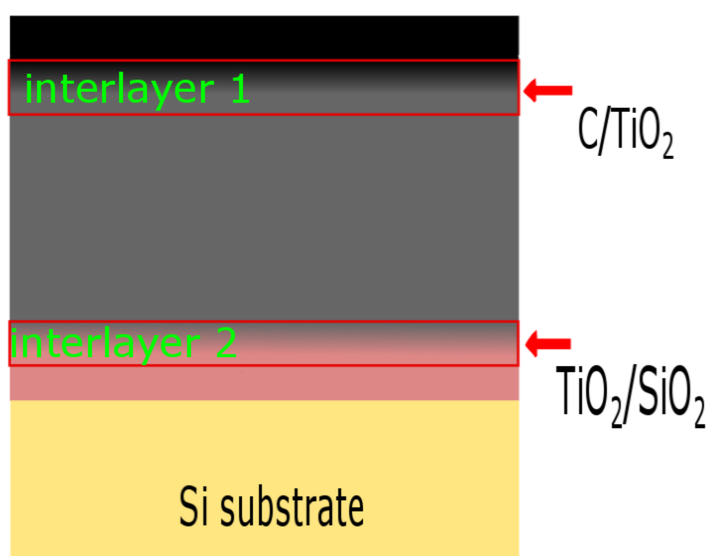


**Figure 5.17:** Schematic of the optical model introducing interlayers at the interfaces (not in scale).

By introducing interlayers at the interfaces in the optical model, schematically shown in Figure 5.17, the fittings presented an obvious improvement, resulting in a satisfactory fit for the reflectance measurement at E=454.2 eV for all three samples. Figure 5.18 shows the fits performed with the three-layer model ($C/TiO_2/SiO_2/Si$) and the optimization achieved by inserting interlayers into the optical model ($C/int1/TiO_2/int2/SiO_2/Si$) for the three samples. The optical constants of the interlayers remained free during the fits since we were not able to determine their composition *a priori*. Considering that the edge of an interlayer is, in general, quite indefinite, i.e. not sharp, a thickness approximation was estimated by evaluating interlayer thickness values that allowed convergence of the fittings for the three samples. We introduced a 0.4 nm interlayer between the contamination layer and the TiO2 layer (int1), and a second 1 nm interlayer between $TiO_2$ and $SiO_2$ (int2).

At this specific energy, we performed two fitting procedures for every sample. First, the whole angle range was considered during the fits, and second, the angle range was split into two ranges ($\Delta\theta_1 = 5 - 11.25^o$ and $\Delta\theta_2 = 11.25 - 20^o$) performing the fittings by parts. This last procedure was done to evaluate the reflectance at smaller grazing angles where there is better signal-to-noise ratio. Both procedures delivered similar results, so an average was reported (Table 5.2) along with the standard deviation as the uncertainty.

From the calculations, a negligibly small delta value (1.175 $E^{-38}$) for the $TiO_2$ layer was obtained at E=454.2 eV, which could imply that reflectance is mainly driven by the contamination layer and buried interface for $TiO_2$ in particular at low grazing angles. At larger grazing angles some contribution comes from the substrate as is shown by the change of periodicity of reflectance *versus* the thickness of the samples in Figure 5.18. The thicker sample (Eb3) produced a beta value for the $TiO_2$ layer approximately 45% lower than the other two thinner samples (Eb1 and Eb2) only at 454.2 eV. It is relevant to say that for energies near the absorption edge, calculations based on a defined optical model become more sensitive to inaccuracies in the input parameters. This could be a possible cause of discrepancies among the results if one sample was more accurately modeled than the others.

For the interlayer at the C/$TiO_2$ interface (int1), we obtained optical constants ($\delta$, $\beta$) = (7.6 $E^{-03}$, 9.6 $E^{-07}$), by taking an average from the three samples. The int1 $\beta$ values provided by each sample are very low and present a large variance between them. Thus, a great uncertainty can be associated to the average reported value ($E^{-05}$). The $\beta$ value of int1 is four orders lower than beta of carbon, $TiO_2$ or titanium. On the other hand, the $\delta$ value of int1 falls between $TiO_2$ and carbon, but much closer to carbon. A thickness of 0.4 nm for int1 is consistent with the conclusion that the optical constants are closer to those of carbon, and this could mean the presence of some carbon contamination mostly concentrated on the uppermost top layer of int1. This suggests a slight mixing/migration of $TiO_2$ into the contamination layer.

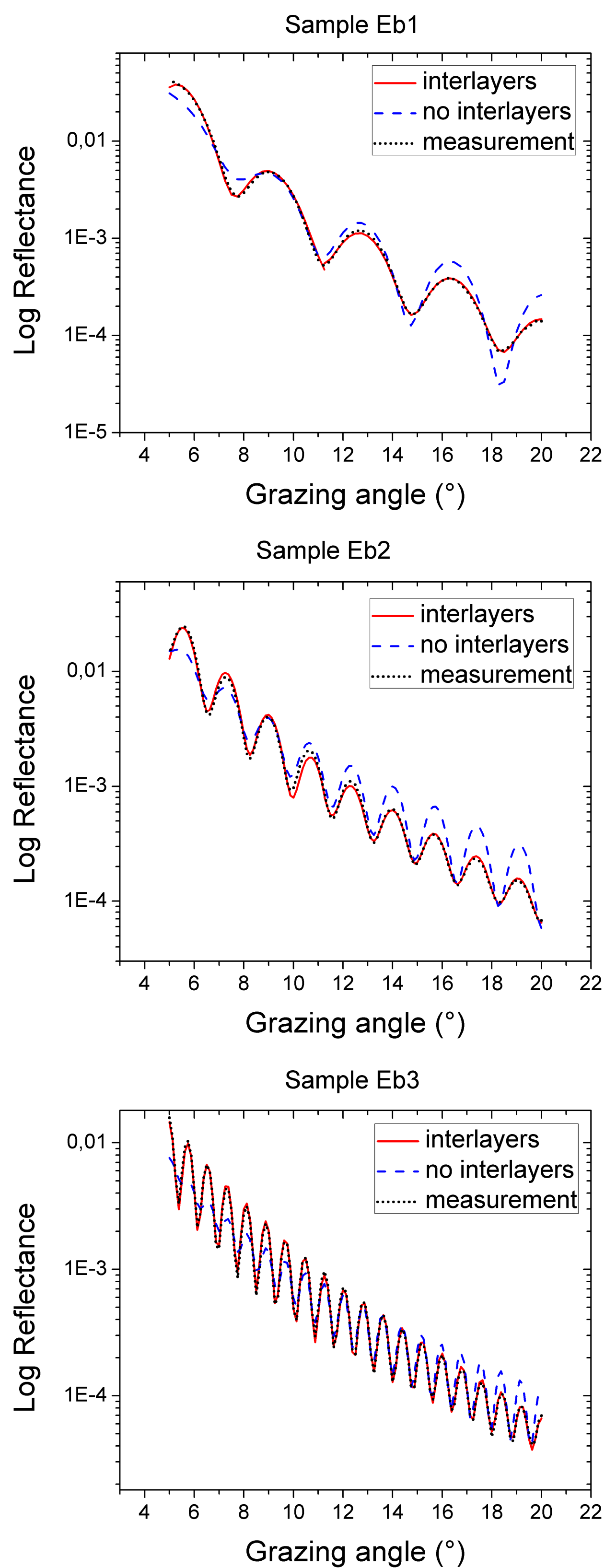


**Figure 5.18:** Fits of reflectance profile measured at E=454.2 eV (dotted line), without including interlayers into the optical model (dashed line), and the optimization achieved inserting interlayers in the optical model (continues line). For (a) sample Eb1, (b) sample Eb2 and (c) sample Eb3.

In the case of the interlayer at the $TiO_2/SiO_2$ interface (int2), we obtained optical constants ($\delta$, $\beta$) = (1.2 $E^{-03}$, 1.8 $E^{-03}$), by taking an average from the three samples. These fall between the optical constant values of Ti and $SiO_2$, but it is not straightforward to say if they are closer to one or the other. This could indicate a mixing between $TiO_2$ and $SiO_2$. Previous publications [69] [71] [70] also suggest that a silicate of the type $TiSi_xO_y$ could take place at this kind of interlayer. If we think in a substrate to surface direction, the oxygen atoms are associated mainly to Si atoms at the growth stage of the film closer to the substrate, while at the next growth state of the film the oxygen atoms are best described to be coordinated in a $TiSi_xO_y$ compound with values of x and y that aredepth dependent, until the final growth stage where $TiO_2$ is stoichiometrically achieved [69]. A thickness of 1 nm for int2 is consistent with the results that show an intermixing between $TiO_2$ and $SiO_2$.
The model that incorporates interlayers was only applied to report the optical constants of $TiO_2$ at a single energy (E=454.2eV) which is particularly sensitive to interlayer thickness values. The model including the interlayers was also implemented at the other energies where we measured reflectance as a way to check and confirm its reliability, obtaining consistent results with the three-layer model. The values obtained for $TiO_2$ optical constants with both models at each energy have only a small variation, well within the estimated uncertainty of 10%.

# Chapter 6

# Soft X-ray reflectometry with a laser produced plasma source

## 6.1 Introduction

Performing measurements at a synchrotron facility like ELETTRA has obvious advantages such as stability, flux, high brilliance, broad energy range and tunable monochromatic radiation source, beam collimation, and more. Unfortunately, there are limitations when it comes to accessibility of large scale facilities. Factors such as expensive booking and tight beamtime schedules generally constrains the reach of the experiment. Thus, the advantages of performing characterisations on a compact table top laboratory reflectometer can sometimes be a considerable advantage.

The research described here is focused on producing grazing incidence reflectometer that works in the soft X-ray spectral range ($\lambda \approx$ 1-20 nm), based on a laser produced plasma (LPP) source. The reflectometer is intended to be simple, relatively low cost and to provide reasonably fast and accurate reflectance measurements. The purpose of the work was initially to implement the spectral reflectometer as a characterisation tool with the multilayer samples we have produced, to demonstrate function and provide a proof of concept demonstration.

In this chapter we first mention the basic concepts of a laser-produced plasma and a transmission grating, followed by an outline of the experimental set up, the acquisition method and the characterisation results obtained with the reflectometer.

## 6.2 Basic concepts and parameters

### 6.2.1 Laser-produced plasma (LPP)

The reflectometer described in this chapter is based on a laser-produced plasma (LPP) source. This type of sources is an appealing alternative to the synchrotron radiation source since it is compact, of relatively low cost and still provides high brightness.

A small volume hot dense plasma is generated when a high power laser pulse is focused onto the surface of a target material. In Figure 6.1, a picture of a LPP generated in our experimental chamber as the light source for the reflectometer is shown.

This plasma consists of particles at very high energies (100eV to several keV) that generate EUV and soft X-ray radiation in particle-particle interactions. The conditions during such plasmas are far from equilibrium and as a consequence they are short-lived. The high temperature conditions imply high particle velocities that make the plasma expand and cool down rapidly. These hot dense plasmas are highly ionized, thus the emitted radiation consists of a broad continuum and narrow line emissions. The first one due to free-electron-ion interactions (mixed free–bound and free–free bremsstrahlung radiation) and the second to bound–bound transitions in the atoms (ions) [1].

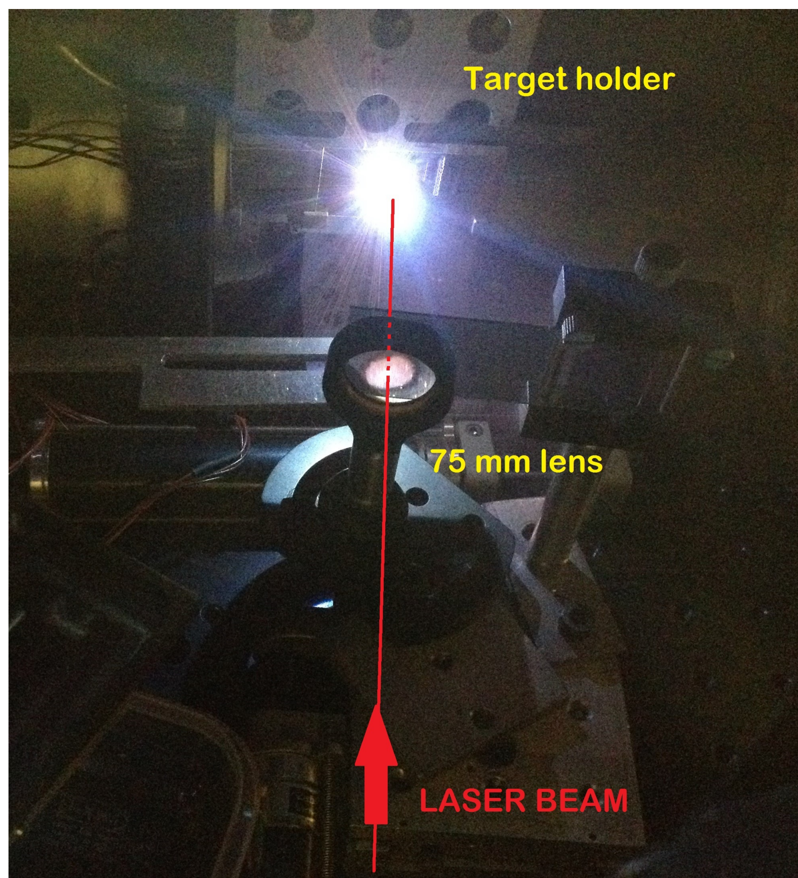


**Figure 6.1:** LPP generated in our experimental chamber as the light source for the reflectometer.

The absorption of the incident laser radiation highly depends on the electron density ($n_e$) in the plasma. During the initial picoseconds of the laser pulse striking the target, free electrons are created, afterwards, the plasma begins to form and is rapidly heated by bremsstrahlung absorption, i.e. the incoming photons energy is ceded to the free electrons increasing their kinetic energy. As this heating continues, more free electrons are generated and the density gradient of electrons arises.
The electron density is related to the natural plasma frequency at which electrons tend to oscillate by Equation 6.1:

$$\omega_p = \left(\frac{e^2 n_e}{\epsilon_0 m_e}\right)^{1/2} \tag{6.1}$$

where $e$=1.6 x $10^{-19}C$ is the electron charge, $m_e$=9.1 x $10^{-31}kg$ the electron mass, and $\epsilon_0$=8.85 x $10^{-12}F/m$ is the permittivity of free space. For instance, for a common neodymium (Nd) laser of 1.06 $\mu$m wavelength, the laser-plasma interaction happens near the critical electron density, $n_c$ = 1 x $10^{21}$ e/cm$^3$ where the plasma frequency matches the laser light angular frequency, which is about 1.8 x $10^{15}$ rad/s.

The electron oscillation is induced by the incident electromagnetic waves (the incoming laser with frequency $\omega$) and these can only propagate in the plasma if $\omega > \omega_p$. The incoming electromagnetic wave is totally reflected when it reaches the critical electron density $n_c$ region, this is where $\omega = \omega_p$. The incoming wave is fully excluded from the region where $\omega < \omega_p$. In Figure 6.2 a plasma electron density gradient is schematically shown. The laser light is absorbed at the critical density region and below. Only a small (hot and dense) region of intense X-ray emission is created beyond the critical density region where energy has been transported by radiation and charged particles. Laser light at the critical surface ($n_c$) is reflected.

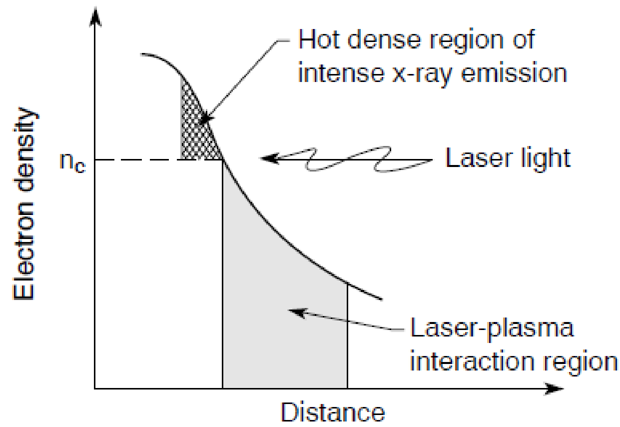


**Figure 6.2:** Schematic of an electron density gradient of a laser-produced plasma [1].

Another important parameter of plasmas is the Debye screening distance ($\lambda_D$), defined as:

$$\lambda_D = \left(\frac{\epsilon_0 \kappa_B T_e}{e^2 n_e}\right)^{1/2} = C\left(\frac{T_e}{n_e}\right)^{1/2} \tag{6.2}$$

where $\kappa_B$ is Boltzmann constant (8.6174 x $10^5$ eV/K) and $T_e$ is the electron temperature. When temperature is expressed in energy units ($\kappa_B T_e$), 100 eV corresponds to

1.16 x $10^6$ kelvin (K). Beyond this screening distance, individual charges are more likely to be screened by other neighbouring and mobile charges. For example, for a 200 eV plasma at that $n_c$ , the Debye screening distance is about a few nm.
The Debye screening distance can be taken as the distance when the presence and effects of individual charges became evident, this is at distances less than or equal to $\lambda_D$ on a spatial scale. Beyond this distance the individual charges are screened and for longer distances charged particle interactions occur through collective motions.
Photon emission from a laser-produced plasma can be basically stated and summarized in three processes:
1)non-bound bremsstrahlug radiation as a result of free electrons interacting with highly charged particles resulting in continuum radiation.
2)recombination between charged particles and free electrons also resulting in continuum radiation (free-bound process).
3)line emission from the bound-bound electron transitions within the excited ions.
The final emitted spectrum from a laser-produced plasma has rather complex composition with contribution from these processes. By varying the target material and the temperature of the laser-produced plasma the emission spectrum of the source can be tuned depending on its application [72].

### 6.2.2 Transmission grating

In this section we will introduce the grating operating principles and outline the basic parameters that characterise it. The background presented here is based on the literature avaliable in reference [73].
The primary function of a grating is to disperse incoming light into specific angles. Monochromatic light incident on a grating surface will be diffracted into discrete directions. The grating can be described as an optical system with a periodic structure or a collection of grooves equally separated by a distance $d$. These grooves can be pictured as being small slit-shaped sources of diffracted light, the light diffracted from each groove will recombine to form a set of diffracted wave fronts. For a given spacing $d$ between each of these grooves, there is a unique set of discrete angles in which the diffracted light from every groove is in phase with that coming from any other groove producing constructive interference.

Gratings can be either transmissive or reflective. The physics that describe them is the same, the difference relies on the fact that for transmission gratings the diffracted radiation lies on the opposite side of the grating with respect to the incident light, while for reflection gratings, the diffracted and incident light are on the same side of the grating.
The geometry of how an incident light is diffracted by a transmissive and a reflective grating is schematically shown in Figure 6.3. Incident light with wavelength $\lambda$ reaches the grating surface at an angle $\alpha$ and is diffracted by the $d$-spaced grooves grating along

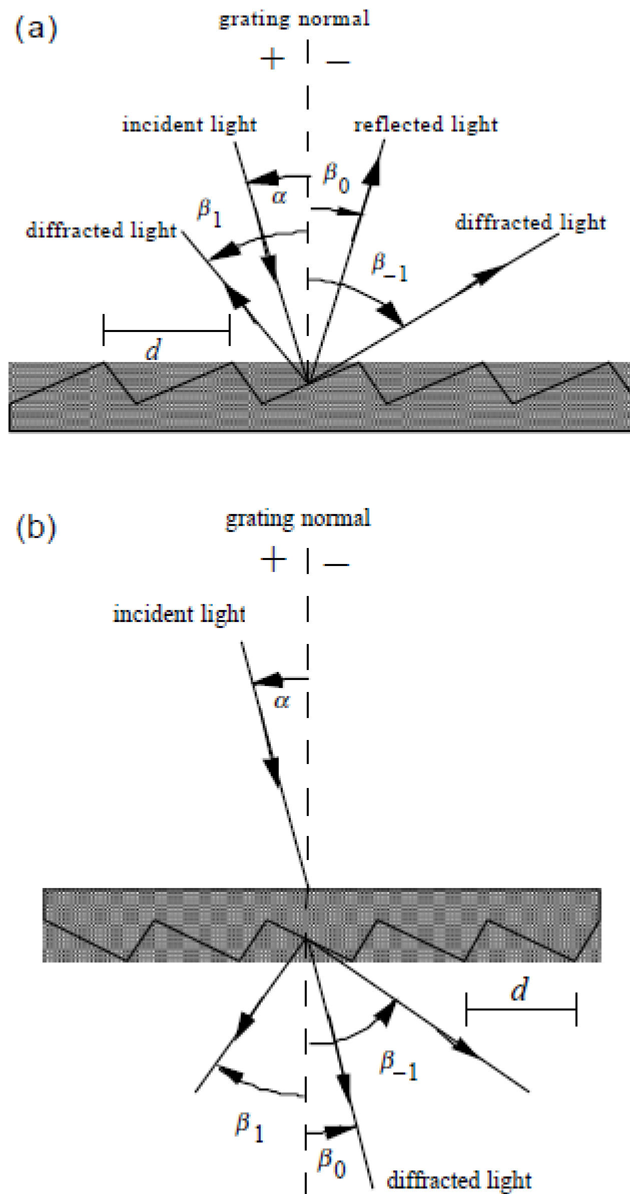


**Figure 6.3:** Geometry of the diffraction by (a) a plane reflection grating and (b) a plane transmission grating [73].

a set of angles $\beta_m$, measured from the grating normal.
The angular locations of the principal maxima of the diffracted light are expressed by the *grating equation* 6.3:

$$m\lambda = d(sin\alpha + sin\beta) \tag{6.3}$$

where $m$ is the *diffraction order* and is an integer. In Figure 6.4 we see that the geometrical path difference between the light coming from two adjacent grooves is equal to $d\ sin\alpha + d\ sin\beta$. From the principle of constructive interference we know that when

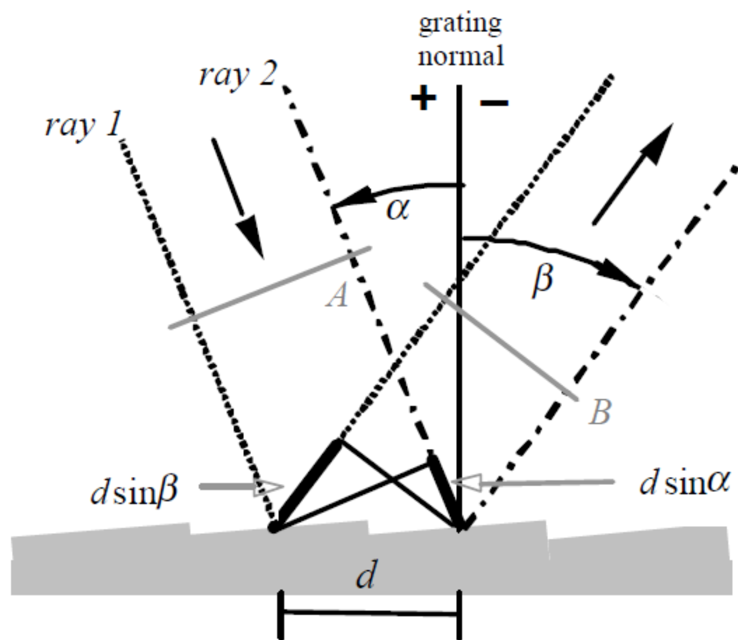


**Figure 6.4:** Geometry of the diffraction and path difference for planar wavefronts [73].

this path difference is equal to the wavelength $\lambda$ of light (or an integer multiple), the light diffracted from these adjacent grooves is in phase and produces constructive interference.
The *angular dispersion* D of a grating is a measure of the angular or spatial separation between the diffracted light of different wavelengths, i.e. the spectral range per unit angle. For incoming light with wavelengths $\lambda$ and $\lambda + \Delta\lambda$, the angular spread $\Delta\beta$ of an $m$ order spectrum is obtained by differentiating Equation 6.3, resulting in:

$$D = \frac{\mathrm{d}\beta}{\mathrm{d}\lambda} = \frac{m}{d.cos\beta} \tag{6.4}$$

The grating's ability to separate or distinguish adjacent spectral lines with average wavelength $\lambda$ is measured by the dimensionless quantity known as its resolving power R:

$$\mathsf{R} = \frac{\lambda}{\Delta\lambda} \tag{6.5}$$

where $\Delta\lambda$ is the smallest resolvable wavelength difference. The resolution limit is established using the Rayleigh criterion, i.e. two wavelengths are resolved when the maximum of one lies at the first minimum of the other. To obtain the expression for the grating resolving power, we use Figure 6.5. Here xy represents the grating transmission plane, being N the number of grooves illuminated and we are considering a normal incidence beam of light with two slightly different wavelengths $\lambda$ and $\lambda + \Delta\lambda$.

These two wavelengths are diffracted by the grating at angles $\beta$ and $\beta + \Delta\beta$. $P_1$ and $P_2$, represent the position of m$^{th}$ order primary spectral maximum of both wavelengths, respectively. The two m$^{th}$ order maxima lines can be resolved if $P_2$ falls in the first minimum of wavelength $\lambda$.

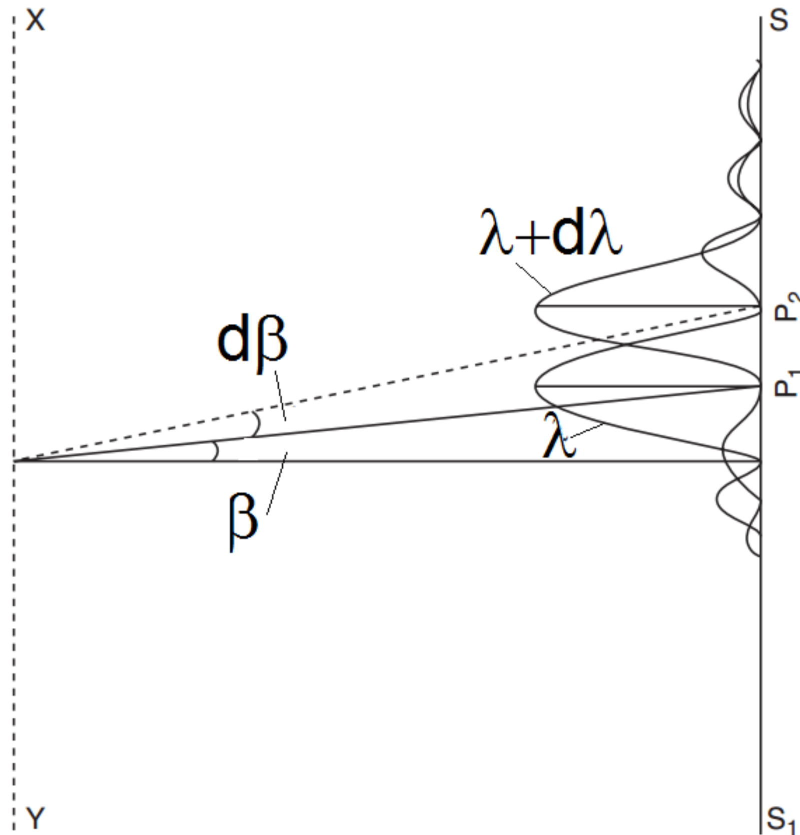


**Figure 6.5:** Schematic of two slightly different wavelengths dispersed by the grating [74].

From geometrical and light diffraction considerations, we know that the first maximum of wavelength $\lambda$ at diffraction angle $\beta$ occurs when,

$$d \sin \beta = m\lambda \tag{6.6}$$

is satisfied, while the equation for the first minimum of wavelength $\lambda$ at the angle $\beta + \Delta\beta$ is,

$$Nd\ \sin(\beta + \Delta\beta) = (mN + 1)\lambda \tag{6.7}$$

On the other hand, the principal maximum for wavelength $(\lambda + \Delta\lambda)$ in the direction

$(\beta + \Delta\beta)$ is,

$$d\ \sin(\beta + \Delta\beta) = m(\lambda + \Delta\lambda) \tag{6.8}$$

If we multiply the last equation by N,

$$Nd\ \sin(\beta + \Delta\beta) = Nm(\lambda + \Delta\lambda) \tag{6.9}$$

The left hand side of Equation 6.7 and 6.9 are the same so we can obtain:

$$\begin{aligned}(mN + 1)\lambda = mN(\lambda + \Delta\lambda) \\ mN\lambda + \lambda = mN\lambda + mN\Delta\lambda \\ \lambda = mN\Delta\lambda \\ \frac{\lambda}{\Delta\lambda} = mN\end{aligned} \tag{6.10}$$

Equation 6.10 expresses the theoretical resolving power as R=mN for a grating. It is then straightforward to say that the resolving power is directly proportional to the diffraction order of the spectrum and the number of grooves iluminated on the grating [74].

In practice, the theoretical resolving power is usually diminished since it depends not only on the incident ($\alpha$) and the diffracted ($\beta$) angles, but also on the uniformity of the distance $d$ between the grooves, the quality of the optics, the slit width and detector. The ability of a system to resolve two different wavelengths, is also conditioned by the dimensions and locations of the slits involved, the detector, aberrations in the images and possible magnifications. This minimum wavelength difference $\Delta\lambda$ between two spectrum lines that can be unambiguously distinguished is called the resolution of the system.

## 6.3 Reflectometer set-up

In this section the reflectometer set up is described. There are four important parts or sections of the set up: the laser, the target holder, the sample holder stage and grating, and the detector system. A schematic diagram of the experimental set-up of the reflectometer is shown in Figure 6.6.

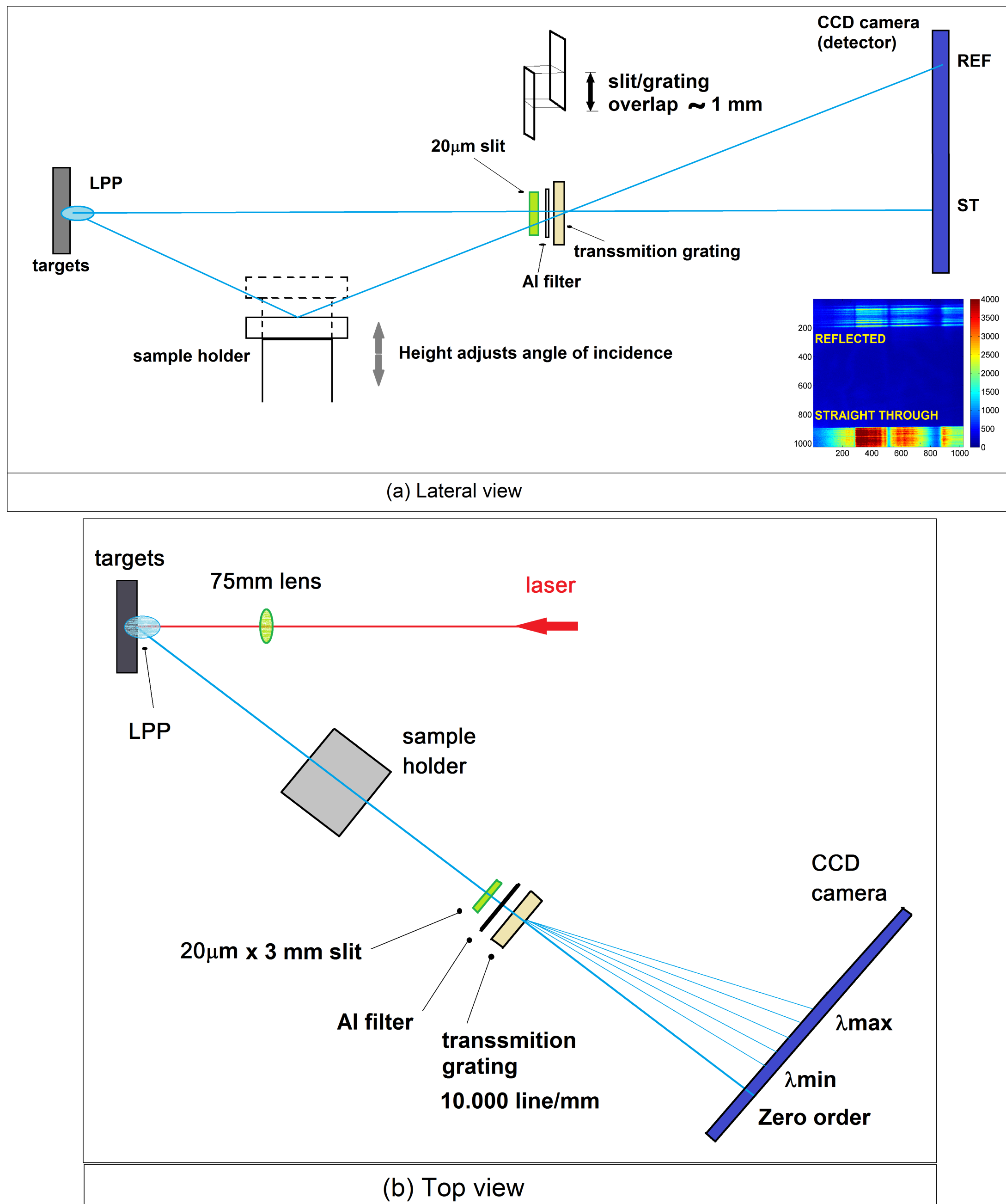


**Figure 6.6:** Schematic diagram of the experimental set-up of the reflectometer. (a) Lateral and (b) Top view.

The experimental arrangement consists of a Continuum Surelite III Q-switched neodymium-doped yttrium aluminium garnet (Nd:YAG) laser, with a central wavelength of 1064 nm, maximum output energy of 760 mJ and a temporal pulse length of 7 ns. The beam is redirected into the experimental chamber through an arrangement of external multilayer mirrors and onto a solid target. The laser is focused with a 75 mm focal length plano-convex lens located inside the chamber and impacts on a relatively high Z solid target material, generating a broadband soft X-ray emission. This is what is called a laser produced plasma (LPP) source, as explained in Section 6.2.1 and shown

in Figure 6.1.
The target holder has the capacity to contain five different targets in the form of a 2.5 x 2.5 $cm^2$ square surface, with 0.1 cm thickness. Two actuators give horizontal and vertical mechanical movement to the target holder, allowing in this way to select over which square (material) the incoming laser beam will impact and thus the spectrum of the LPP source. The beam always arrives perpendicular to the target surface.
The sample holder is placed in the center of the experimental chamber. This is connected to another actuator which is computer controlled to select a fixed grazing incidence angle, with adjustable tilt.
The light reflected on the sample surface and the light coming from the source (straight through), go through a 20$\mu$m x 3 mm vertical slit, followed by an aluminium filter, both placed immediately before a free standing 10 lines/$\mu$m transmission grating which serves as the wavelength disperser. The filter is an 80 nm thick aluminium layer deposited on a 150 nm $SiN_3$ membrane, suppressing unwanted scattered visible light radiation. There is a slit-grating overlap of $\approx 1$ mm.
Finally a charge coupled device (CCD) camera Princeton Instruments (back-thinned, Model N$^o$7404-0001) works as the soft X-ray detector system. The CCD chip consists of a 1024 x 1024 pixel array, with 13.5 x 13.5 $\mu$m pixel size. The detector is located to ensure that the captured spectra are entirely from the first and higher diffraction orders of the grating and exclude zero order (m=0) radiation. A computer is used for collecting and processing the data. WinSpec32 software is used to interface with the controller and operate the CCD. The source-grating and grating-detector distances are both 450 mm.
The very intense infra-red (IR) radiation originating from the scattered laser beam inside the chamber was baffled out with dark vacuum-resistant plastic covers, placed around the slit and grating, and on internal parts of the experimental chamber along the light path. The baffles significantly contributed in controlling the background noise of the measurements, as otherwise a blotchy, spatially consistent, but overall intensity variable background dramatically reduced the signal quality. The background noise prior to insertion of the baffles in the chamber is shown further on in Section 6.7 in Figure 6.14 ("Limitations and lessons learned") .
An inside view of the experimental chamber is shown in Figure 6.7. The equipment employed, shown in Figure 6.8, is a stainless steel cylindrical chamber with a vacuum system composed of a rotary pump and a turbo molecular pump, that allowed us to work at pressures of the order of $10^{-5}$–$10^{-6}$mbar.

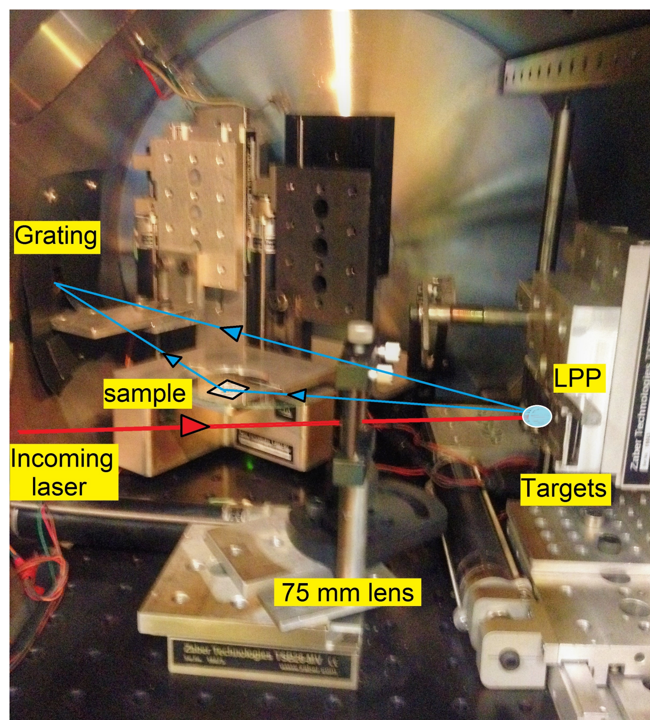


**Figure 6.7:** Inside view of the experimental chamber of the soft X-ray reflectometer at UCD.

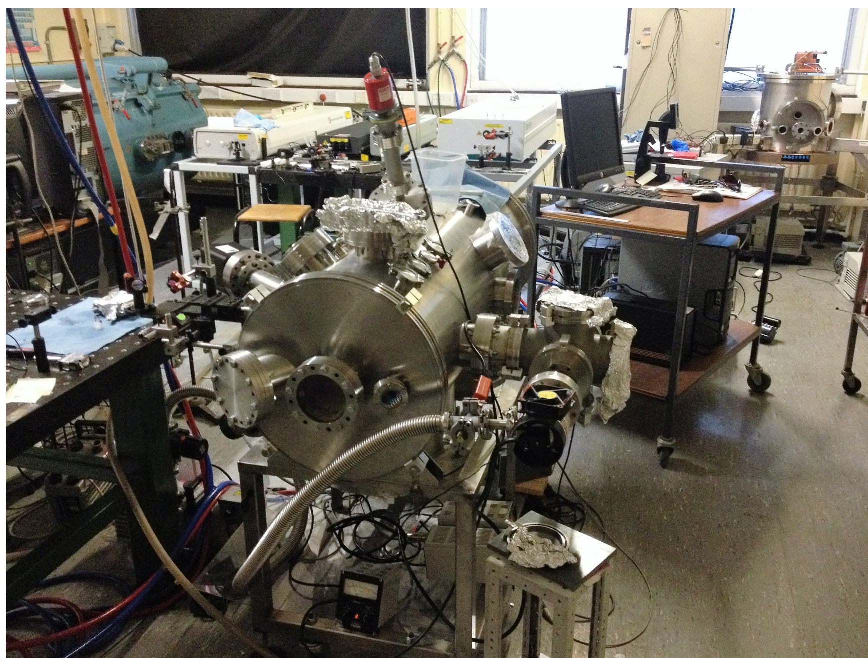

**Figure 6.8:** Experimental chamber of the soft X-ray reflectometer at UCD.

## 6.4 Measurement acquisition

The measurements are performed by keeping the laser position fixed and focused onto a solid target surface. After each laser pulse the target is moved to make sure the laser always hits a new spot on the surface at the following shot. The reflectance is taken by constantly moving the target in distance steps $\geq$100$\mu$m in the x and y directions, scanning in this way the selected material surface and producing the plasma. The constant scanning movement prevents the generation of holes in the target or excessive ablation, ensuring reasonably constant target conditions.
The emission is collected by the transmission grating with a 20$\mu$m slit as an entrance aperture and then recoded by the CCD camera detector. Our acquisition was typically over 20 seconds so we cooled the CCD to -10$^o$C.
In this manner, we collected at the same time, the emission coming from the plasma itself going straight through the grating and the emission reflected from the sample surface located in the sample holder. The straight trough (ST) and reflected (REF) spectra appear in the bottom and on the top section of the detector, respectively, as shown in Figure 6.9.

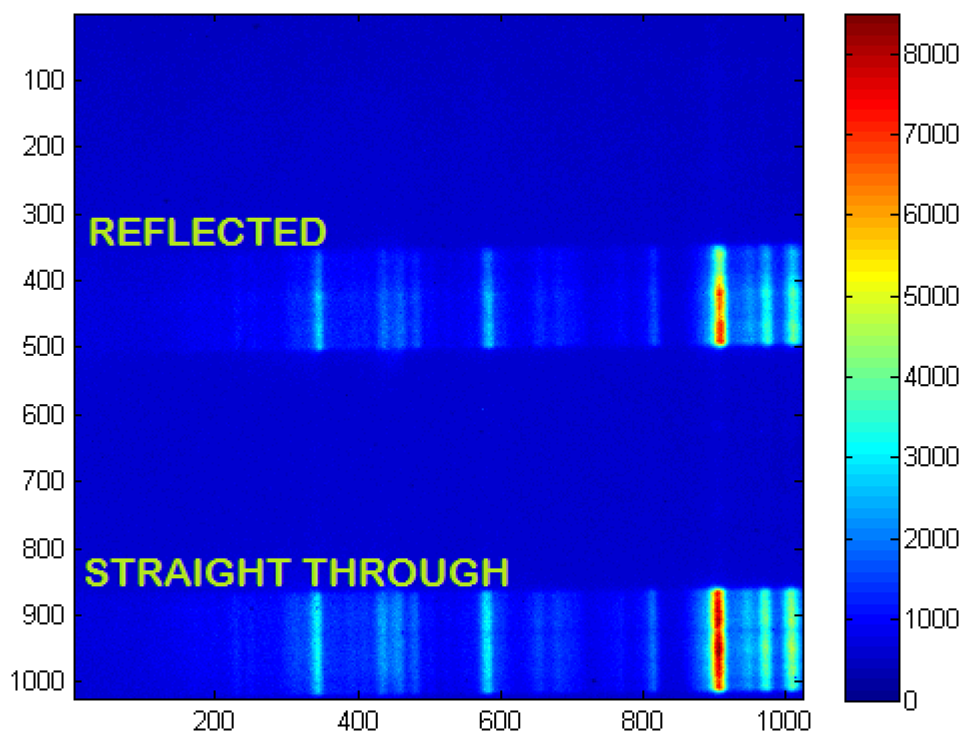


**Figure 6.9:** Measurement acquisition image. Straight through and reflected spectrum of an RBSN source target.

The angle of reflection of the light from the plasma source striking the sample is

fixed for each acquired spectrum image. This fixed grazing incidence angle can be varied through a range of approximately 0.5-3$^o$ by moving up and down the position of the sample holder. In this set-up, this angular range was limited by the detector size and distance.

Taking simultaneously the direct and the reflected emission is an advantage since we are able to register and therefore take into account instabilities of the source when taking the ratio of the spectra. This also makes the measurements faster than if we had to record the direct and reflected emission separately like in a more conventional way (e.g. with a synchrotron).

With a MATLAB code (see Appendix B) we are able to extract and analyse the data collected, obtaining not only the source target spectrum but also that of the reflected light from the sample under study. By accounting for the background noise on each spectrum, and then taking the ratio between the reflected signal over the straight through signal $S_{REF}/S_{ST}$, we obtain the reflectance of the sample.

## 6.5 Wavelength calibration

To validate the spectra acquired with any spectrometer, a wavelength calibration is needed.

The CCD detector measures the spectrum emitted by the source over a range of wavelengths subtended by the size of the CCD chip. This range is established by the grating orientation, that sets the wavelength of the incident light that reaches the central pixel of the CCD detector [75]. In this work, the selected range was $\lambda$=1.5-5 nm, a range where there is reasonable grating efficiency, source emission, and many materials possess absorption edges (see Figure 6.10). This includes also the "water window" range $\lambda$=2.3-4.4 nm, which is of interest for biological imaging.

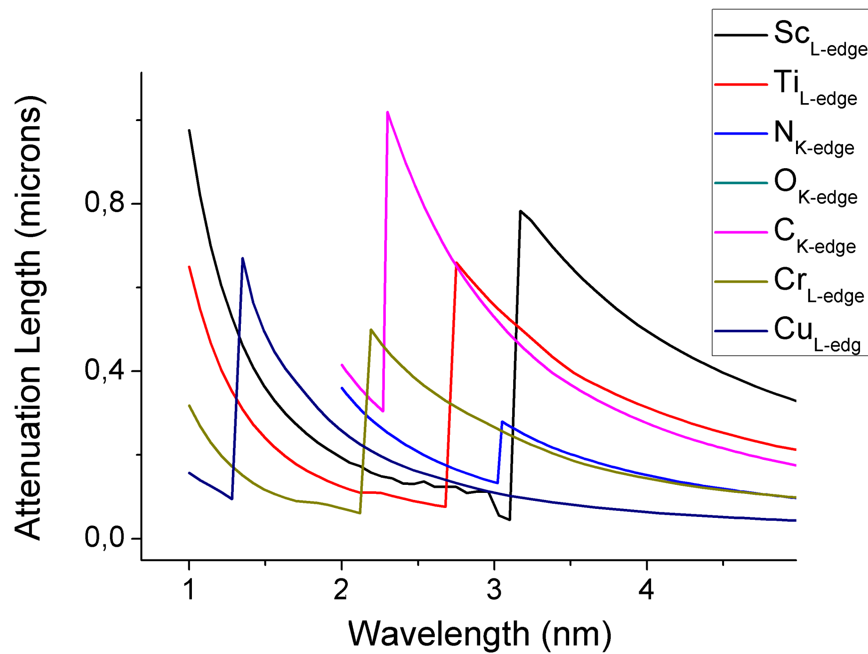


**Figure 6.10:** Attenuation length (1/e drop off)of several materials showing the absorption edges in the Soft X-rays spectral range.

The calibration of the spectral reflectometer is performed by measuring a spectrum with known wavelengths and recognizable peaks in the region of interest. Then, the known wavelength values are assigned to the correspondent pixels of the detector where the known peaks are manifested. The rest of the range is determined by curve fitting.
Comparing the measured spectra of the various materials with the known values establishes a wavelength calibration of our spectral reflectometer [75].
In our work we chose the spectrum of a Reaction Bonded Silicon Nitride (RBSN) target for the purpose of wavelength calibration, due to its well defined emission peaks (due to Si, N ions) and wavelength reference values previously obtained from the National Institute of Standars and Technology (NIST) database [76]. We were also able to compare our spectra with RBSN spectra taken with an already calibrated grazing incidence spectrometer with a higher resolution ($\lambda/\Delta\lambda \approx$300).
Figure 6.11 shows with solid circles and a solid line, a plot of the known wavelength values *vs.* the pixel to which this wavelength value was assigned and its corresponding linear fit, respectively. In Figure 6.12, the deviations between the values of the fit and the known wavelength values are shown. It can be concluded from Figure 6.12 that the wavelength calibration is accurate to $\pm$0.015 nm.

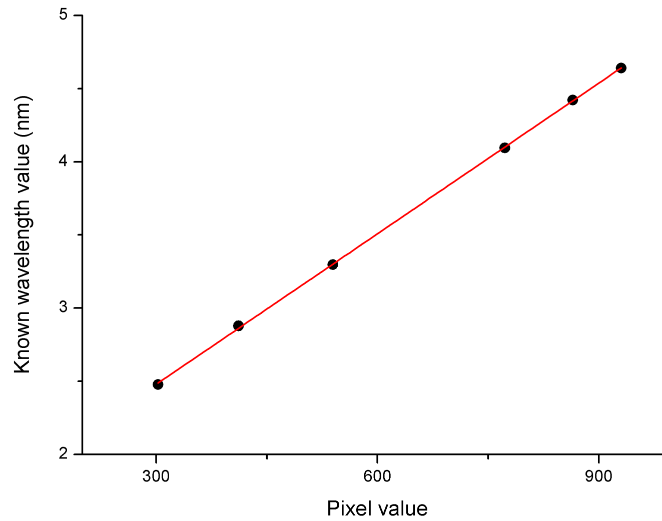


**Figure 6.11:** Plot of the known wavelength values of a RBSN source as a function of the pixel assigned, and its linear fit.

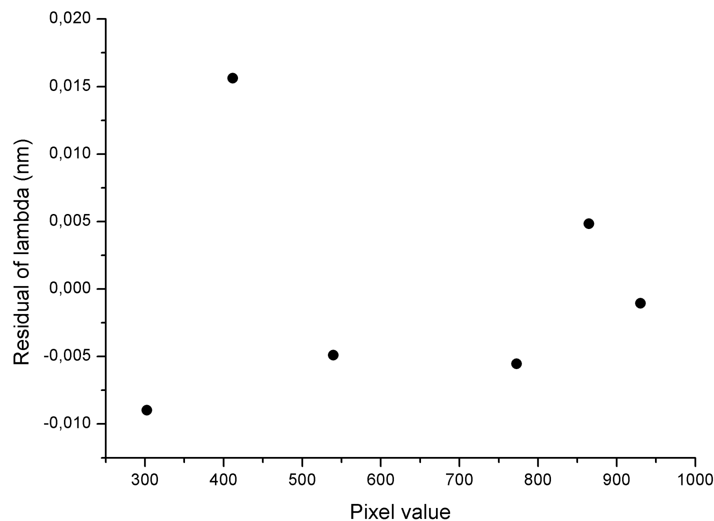


**Figure 6.12:** Plot of the difference between the known wavelengths and the best fit values as a function of pixel value.

## 6.6 Reflectometer spectral resolution

In principle, the technique has no limitations on the spectral range of operation. Within the spatial constraints of the vacuum chamber used in this work, our reflectometer operates in the 1-20 nm spectral range depending on the LPP source location and grating-to-CCD distance. Our spectra covered the 2-5 nm region, delimited by the size of the

CCD chip. The laser produced plasma source is approximately $\Delta S$= 45 $\mu$m in size. The light source size estimation is based on the measurements and calculations done mainly by Luning Liu in an internal UCD group study [77], where she measures the beam quality factor ($M^2$) of the laser used in this work to be $M^2$=3.5. The equation to calculate the laser beam waist radius $W_o$ is:

$$W_o = \frac{4\lambda}{\pi}\left(\frac{F}{D}\right)M^2 \tag{6.11}$$

where $\lambda$ is the laser wavelength (1.06 $\mu$m), F the focal length of the lens used to focus the laser (75 mm) and D the diameter of the unfocused laser (8 mm). With these parameters we estimated a source size of approximately $\Delta S$= 45 $\mu$m.
As mentioned in Section 6.3, there is a A=20±2 $\mu$m slit aperture placed directly before a 10 lines/$\mu$m transmission grating, and a CCD camera as a detector. The source-to-grating distance is $L_1$=450 mm and the grating-to-detector distance is $L_2$=450 mm. The sample holder is in the middle of the path from the source to the grating, i.e. the distance between source and sample is 225 mm. In the work reported here, the grazing incidence angle at which the light strikes the samples is $2^o$, but this could be easily varied between $0.5^o$ and $3^o$ . A schematic diagram with the dimensions and dispositions of the set-up is shown in Figure 6.13.

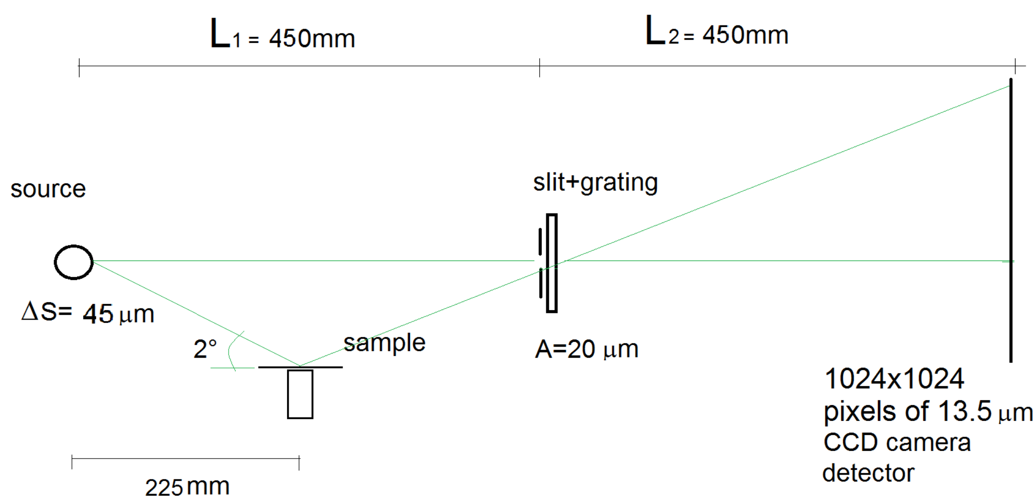


**Figure 6.13:** Schematic diagram with dimensions and dispositions of the set up (not in scale).

To describe the operating principle of the reflectometer, observe that the arrangement is in principle exactly the same as a transmission grating spectrograph in normal incidence geometry, which is indeed a simple optical arrangement. The soft X-ray source projects a shadow of the grating section delimited by the 20 $\mu$m slit, onto the detector plane [78]. The light going through the grating is diffracted into the zeroth and

higher orders, as stated by the grating Equation 6.3 described in Section 6.2.2 resulting in:

$$m\lambda = d(\sin\alpha + \sin\beta) \tag{6.12}$$

where $d$ is period of the grating and $m$ an integer assigning the order. The grating period gives a theoretical cut-off $d = \lambda$, thereby setting a maximum wavelength that can be detected, but in reality this is limited by the size of the detector chip along the dispersion axis. On the other hand, the minimum detectable wavelength is given by the spectral resolution and overlap with the zero order.
Spectral resolution depends mainly on two factors: the ideal dispersive resolution of the grating $\Delta\lambda_D$ and the geometrical resolution $\Delta\lambda_G$ which accounts for spectral blurring caused by a finite source size ($\Delta S$) and the slit aperture A. The theoretical definition of a grating's resolving power is given by $R = \frac{\lambda}{\Delta\lambda} = Nm$, N being the total number of illuminated grooves in the grating. Thus, the dispersive resolution here is governed by the number of grooves that fit in the slit aperture, and is given by:

$$\Delta\lambda_D = \frac{\lambda}{Nm} = \frac{\lambda\, d}{mA} \tag{6.13}$$

On the other hand the geometrical resolution is given by:

$$\Delta\lambda_G = \left(\frac{d}{m}\right)\left[\frac{(\Delta S + A)}{L_1} + \frac{A}{L_2}\right] \tag{6.14}$$

Thus, the overall spectral resolution accounts for these two factors and is given by [79] :

$$\Delta\lambda = \sqrt{\left[\frac{d\lambda}{mA}\right]^2 + \left[\left(\frac{d}{m}\right)\left[\frac{(\Delta S + A)}{L_1} + \frac{A}{L_2}\right]\right]^2} \tag{6.15}$$

If we keep the total distance D=$L_1$+$L_2$ constant, the variables $L_1$ and $L_2$ can be changed to obtain an optimum spectral resolution. For a fixed D, we differentiate Equation 6.15 with respect to $L_1$ to obtained the best value:

$$L_1(opt) = \frac{D\, c}{(1 + c)} \tag{6.16}$$

where $c = \left[\frac{(\Delta S + A)}{A}\right]^{1/2}$. The distance $L_1$ is independent of the wavelength. Furthermore, the total distance D is constrained by considering the intensity at the detector and the spectral resolution. Replacing $L_1$ in Equation 6.15 with $L_1$(opt) we get the new expression for the spectral resolution:

$$\Delta\lambda = \sqrt{\left[\frac{d\lambda}{mA}\right]^2 + \left[\frac{d(1+c)[\Delta S + (1+c)A]}{(mcD)}\right]^2} \tag{6.17}$$

From Equation 6.17 we observe that spectral resolution is improved by increasing D, and for higher D values, Equation 6.17 tends to $\Delta\lambda \cong \frac{\lambda}{m}\frac{d}{A}$, where diffraction starts to govern. The intensity decreases in proportion to the distance from the source to the detector plane as $1/D^2$, and the optimum value of D can be found as a compromise between intensity and spectral resolution. Another possibility to optimize the resolution for the set up is by setting $\Delta\lambda_D = \Delta\lambda_G$ [78].
In our work, we also encountered laboratory room space constraints and setup restrictions, limiting our choice of the distances between the optical elements. Thus, we were only able to consider the optimum theoretical conditions to a certain extent. This resulted in some spectral resolution loss for our reflectometer. In our setup, a value of D=900 mm was used to ensure high spectral resolution and appreciable intensity, accounting for the previously mentioned variables.
If we take into account the dispersion and geometrical limits using Equation 6.15, a theoretical value of the spectral resolution can be calculated for our setup. In Table 6.1 are shown for comparison the theoretical ($\Delta\lambda_{th}$) and experimental ($\Delta\lambda_{exp}$) spectral resolution of our reflectometer for different wavelengths. The experimental FWHM values reported in Table 6.1 were taken from the Reaction Bonded Silicon Nitride (RBSN) spectrum obtained with our spectral reflectometer.

**Table 6.1:** Theoretical and experimental spectral resolution of our reflectometer for different wavelengths

| Wavelength (nm) | Theoretical $\Delta\lambda_{th}(nm)(FWHM)$ | Experimental $\Delta\lambda_{exp}(nm)(FWHM)$ |
|---|---|---|
| 4.39 | 0.056 | 0.047 |
| 3.28 | 0.053 | 0.042 |
| 2.46 | 0.052 | 0.041 |

## 6.7 Reflectometer limitations and lessons learned

It is important to emphasize that the results presented in this work are a consequence of measurements taken on a very crude and prototype-like system with known noise problems that could relatively easy be remedied in a bespoke vacuum chamber set-up. The CCD used here was 20 years old and quite dirty so that signal-to-noise was adversely affected, a newer CCD camera would greatly improve the system.
The very intense infra-red (IR) radiation originating from the scattered laser beam inside the chamber was baffled out with dark vacuum-resistant plastic covers, placed around the slit and grating, and on internal parts of the experimental chamber along the light path. The baffles significantly contributed in controlling the background noise

of the measurements but was not completely eradicated. The background noise presented a blotchy spatially consistent but overall intensity variable structure. This was the response to the scattered IR radiation and it was inherent to the camera, making the pattern unalterable. The "structured" noise affected the signal quality, and the reflectance results since straight through and reflected spectral information is extracted from two different sections on the CCD chip (bottom and top, respectively). The background noise prior to insertion of the baffles in the chamber is shown in Figure 6.14.

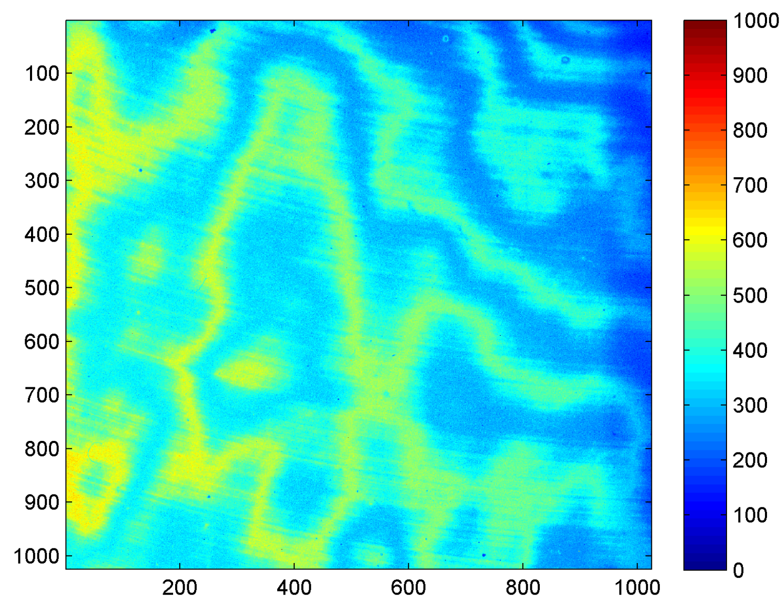


**Figure 6.14:** Background noise prior to insertion of the baffles in the reflectometer. The noise presents a spatial structure of variable intensity as an inherent response of the CCD to the scattered IR radiation.

The measurements were also taken before any of our debris mitigation work was begun.

The spectral resolution could also be dramatically improved by a larger source-to-CCD distance and improved grating. The spectral resolution was also affected by the source size; but no systematic study was done to optimize this aspect of the reflectometer. The spatial stability of the source was not very consistent due to the design of the target holder and it has also contributed to a deterioration of the overall spectral resolution.

The setup dimensions also fixed certain limitations in the angular range of action, and wavelength spectral range of operation.

Thus, the results indicate early stage potential rather than final results.

## 6.8 Target materials

We have acquired the spectra of seven different materials in order to identify a material that would qualify as a target source for the LPP reflectometer. This means a material that can produce a sufficiently continuous and bright emission spectra over the wavelength range under study, so that we are able to observe absorption edges and interesting features that may emerge during the reflectance measurements [80].
Plasmas of each material have different brightness in different regions of the spectrum, so by investigating different targets we can identify the more efficient to be used as the source in our reflectometer. The correct choice of target used as the LPP source will make more evident certain features under study, in spectral regions where they have more brightness.
In this research we separately investigated reaction bonded silicon nitride (RBSN), zirconium (Zr), tungsten (W), silver (Ag), titanium (Ti), vanadium (V) and tantalum (Ta) as target materials. Their respective spectra are shown in Figure 6.15, the purity of all targets was approximately 99.9%. Due to its broad and practically line-free continuum spectrum, we selected W as the source target material for the LPP used in our measurements because of its broad spectra and availability. The size of the source ($\Delta S$) was measured to be approximately 45 $\mu$m, with a laser energy going into the chamber of $\approx$ 550 mJ at $\lambda$= 1064 nm and with the laser beam focused onto the target surface with a 75 mm focal length plano-convex lens.

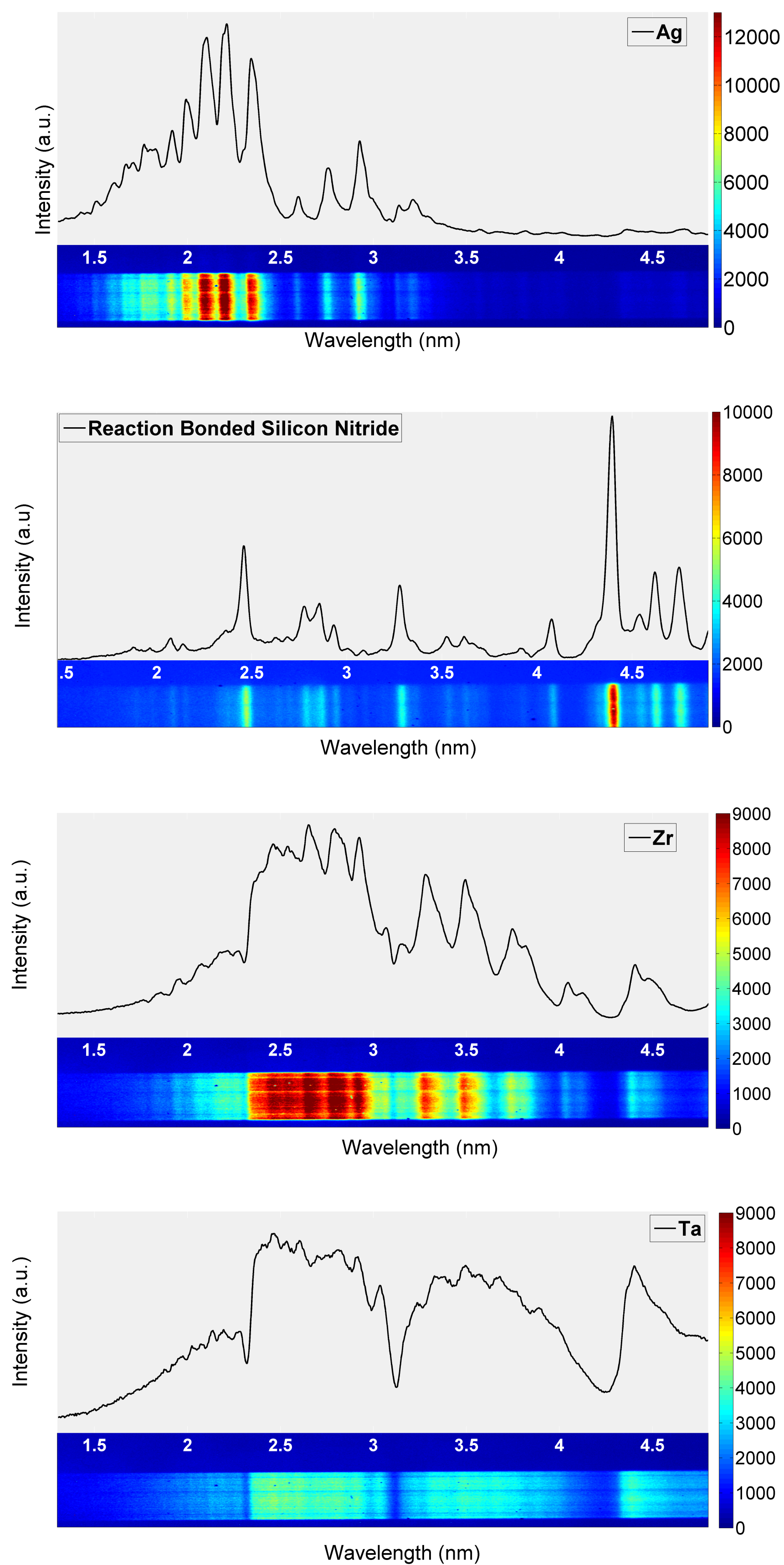


**Figure 6.15:** Direct unreflected spectra from different target materials.

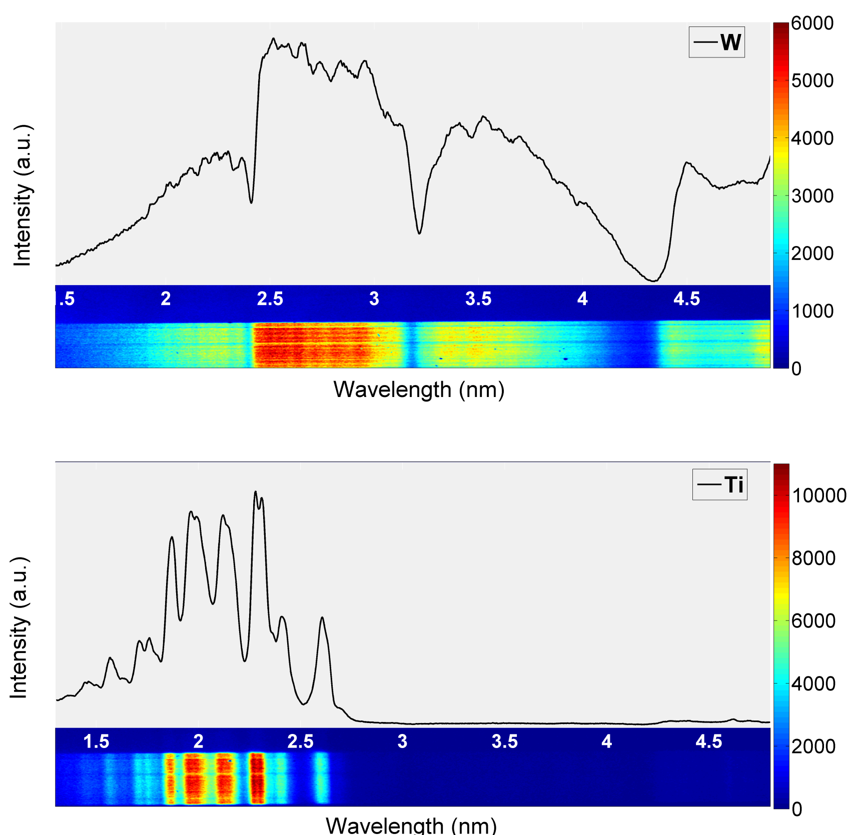


**Figure 6.15:** Direct unreflected spectra from different target materials (cont.)

## 6.9 Results and discussion

### 6.9.1 Reflectometer debris analysis and sensitivity to capping layer thickness change.

In order to generate a LPP source, a target material is ablated and evaporated. This process generates unavoidable debris that in the configuration used here could eventually contaminate the sample under study by debris deposition on the sample surface. Generally, to produce a bright enough source and a satisfactory signal-to-noise ratio that would work for reflectance measurements in our reflectometer, we need 200-300 shots with approximately 550 mJ/shot for every measurement acquisition. To evaluate how this would influence the reflectance results, we performed an experiment in order to test how "dirty" our setup was.

In this experiment, we shot a Ti target over 30000 times in total, taking reflectance measurements every 3000 shots. We chose Ti because of its absorption edge evident at E= 453.8 eV ($\lambda$= 2.74 nm) in the spectral region under investigation (2-4.5 nm). The experiment would have been ideally performed on W, which was the choice of source target material; but W does not present any absorption edge in the wavelength range under

study thus making difficult the detection of change in reflectance.
We also measured the thickness of the resulting deposited debris layer with AFM, and evaluated how the Ti absorption edge increased in depth with increasing number of shots and layer thickness. The sample under investigation was a 5x5 $cm^2$ clean polished silicon substrate.

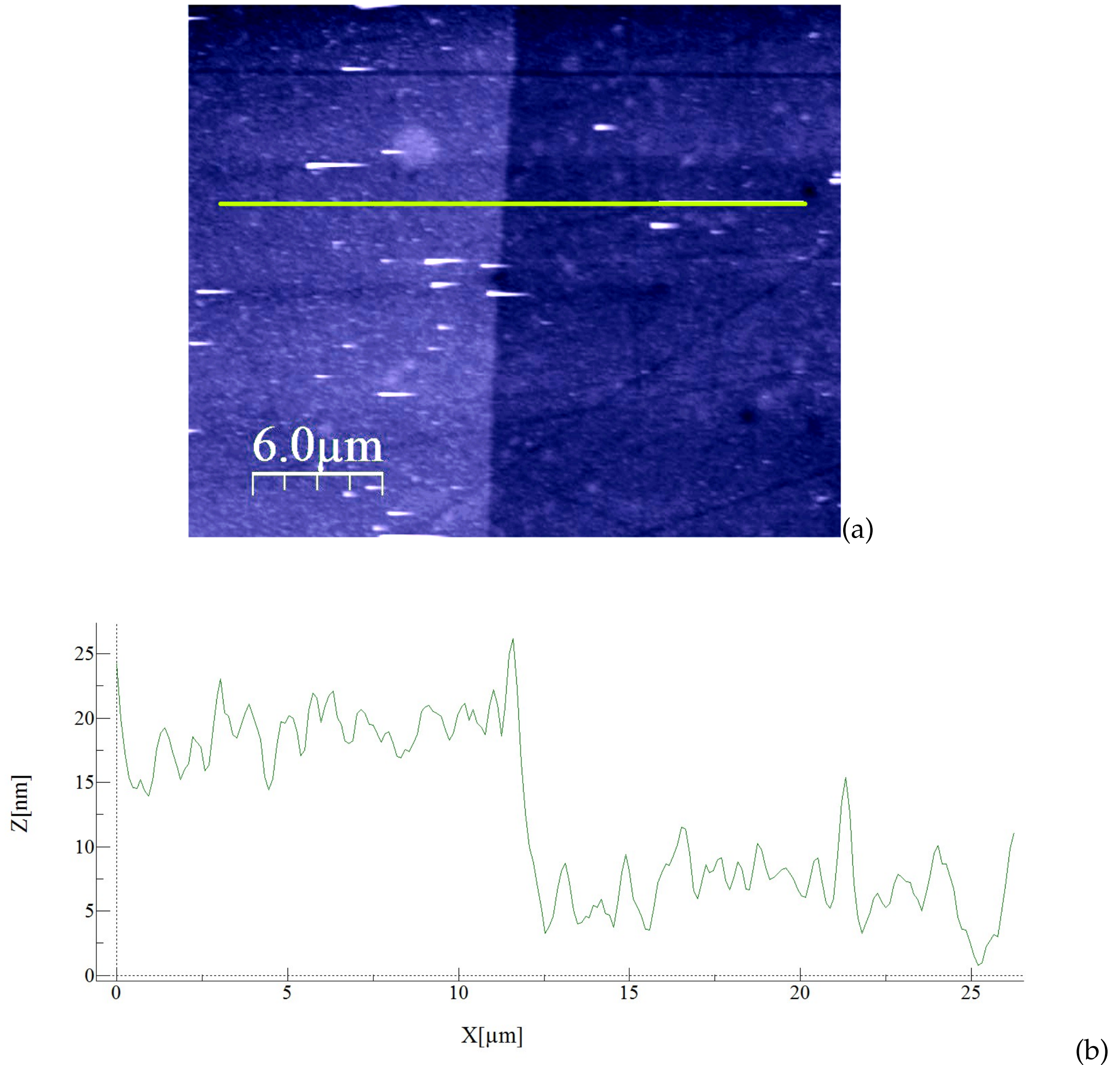


**Figure 6.16:** (a) AFM measurement of the step hight between the substrate original surface and the capping layer after debris exposure. (b) Profile of the step across the green line.

In Figure 6.16, the AFM measurement performed on a step between the substrate original surface and the final deposition layer surface is shown, and clearly displays a step hight of approximately 15 nm after ≈24000 shots with 550 mJ on the Ti target. The sharp step was achieved by masking part of the substrate with a permanent marker, thereby avoiding deposition on that particular zone. After deposition, the permanent marker mask is removed with acetone, leaving a clear, sharp and measurable step.

This test showed not only an estimation of the contamination on the samples during the measurements, but also how sensitive the spectral reflectometer is to changes in the capping layer thickness of the sample. In Figure 6.17, the reflectance measurements during debris exposure on the sample is shown. Each set of data was taken at every 3000 shots on the Ti target.

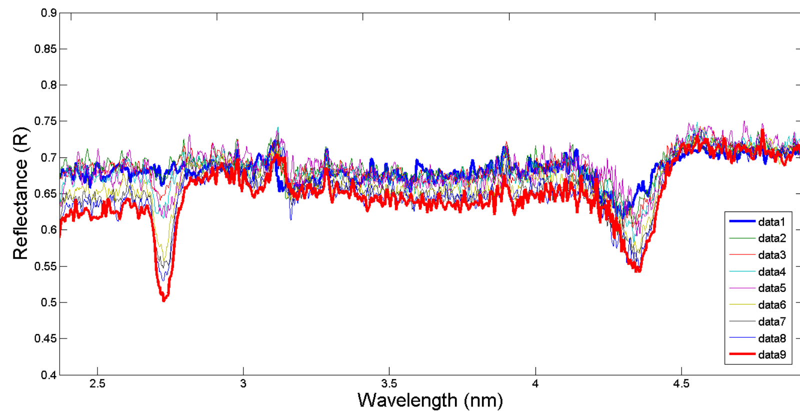


(a)

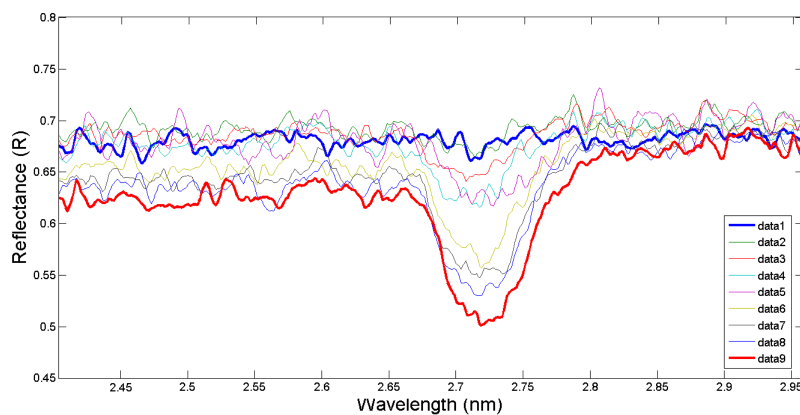


(b)

**Figure 6.17:** (a)Reflectance measurements during debris exposure.(b) Ti edge close up.

From Figure 6.17(b), it can be observed that the Ti edge becomes evident in between "data2" and "data3", this means that after ≈4000 shots (at 550 mJ) of debris exposure the reflectance measurements became sensitive to the deposited material. Furthermore, since the final deposited layer thickness was measured to be of 15 nm, assuming a linear deposition behaviour of thickness *vs.* shots, this could suggest that the reflectometer is sensitive to a Ti thickness layer (deposited in "data2") of ≈2 nm.
In principle, we can say that even though the setup is not perfect and contamination could eventually alter and damage the sample, the amount of shots needed to take a reflectance measurement with this setup is only ≈300, suggesting that under these conditions, the reflectance results presented here are not affected by debris contamination.

### 6.9.2 Debris mitigation

As a continuation of the experiment described in Section 6.9.1, we introduced new elements in the set up with the final purpose of mitigating the debris generated by the LPP source, to improve the system as it is. These results are of interest more generally in the mitigation of debris in slab target laser plasma X-ray sources.

First, we introduced a 300x300 mm simple plastic shield in the chamber, located between the LPP source and the sample position in order to baffle some fraction of the debris originating during the generation of the light source. The shield had a 2 mm width by 20 mm long slit that allowed light to reach the sample surface and the grating. Second, we introduced as a complement for the baffle shield, a set of neodymium permanent magnets close to the target surface, and immediately after the LPP. The new set up is schematically shown in Figure 6.18.

The influence of a magnetic field on the LPP is a topic that has been studied by many authors, reporting that in comparison with the free expansion of the plume into vacuum, the presence of a magnetic field generates a magnetic trap that reduces the plume expansion velocity and deflects and confines the ions [81] [82] [83]. Thus, the shield and the magnetic field, were introduced with the intention of deflecting and intercepting charged ions (debris) produced during the generation of the light source, thus reducing the amount of debris reaching the sample surface.

In the present work, an ion distribution study with and without a magnetic field was not carried out. We performed a simple theoretical calculation (See Appendix A) to estimate some of the important parameters to predict the deflection of the plume direction with respect to the target normal and thus to the shield slit position.

To do so, we assumed a minimum magnetic field of 0.05 T [83], uniform along the plume expansion direction. The target surface is placed at a distance of $\approx$ 1 mm from the magnets edges. The ions propagating from the source and crossing through the magnetic field volume zone (1.5x2.5x1.1 $cm^3$), are subjected to the influence of the magnetic field and so to the corresponding Lorentz force. This is $F_L$=$|\overline{\mathbf{F}_L}|$=$|q||\overline{\mathbf{v}}X\overline{\mathbf{B}}|$=$|q|vB\sin\theta$, where $q$ is the charge, $v$ the velocity of the ion, $B$ the magnetic field of the neodymium magnets and $\theta$ the angle between $\overline{\mathbf{v}}$ and $\overline{\mathbf{B}}$. The velocity can be expressed as: $v_{ion} = \sqrt{\frac{2.E_{ion}}{m_{ion}}}$. For singly charged Ti ions of energy 10 keV we calculated a lateral deflection of 0.737 mm at the shield with respect to the slit position. We assumed this would be enough to reduce the amount of ionic debris going trough the slit, thus reducing contamination.

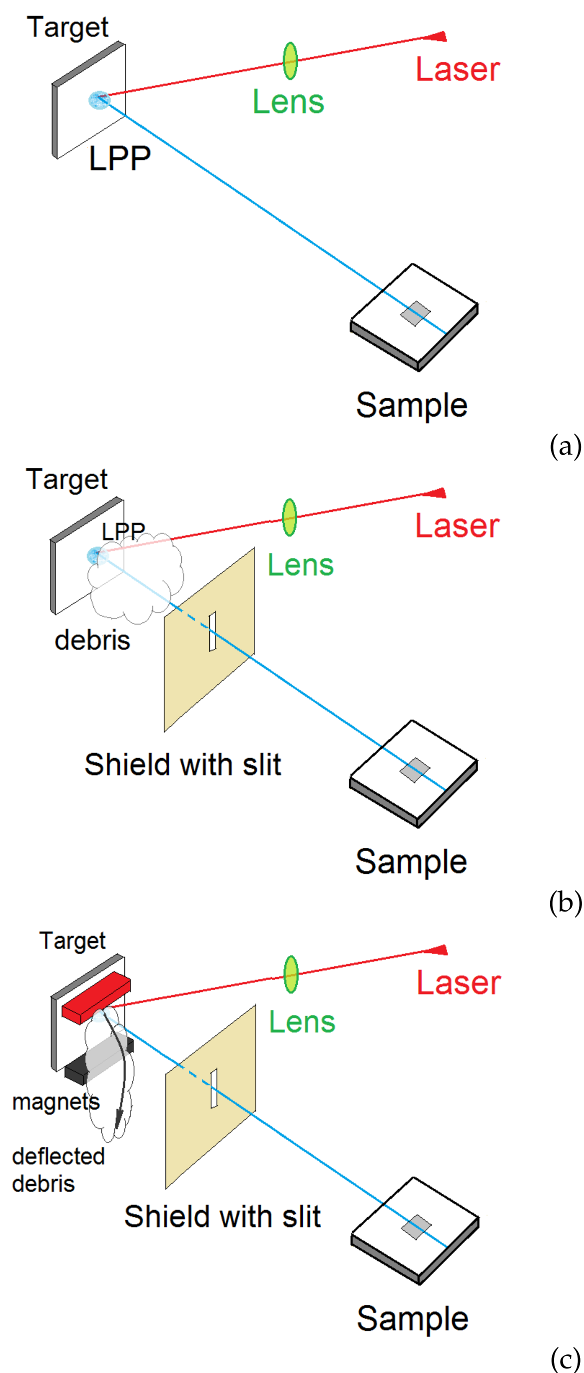


**Figure 6.18:** Set-up to mitigate debris, (a) without shield (i.e.original set-up) (b) with the shield incorporated and (c) with the shield and a set of neodymium permanent magnets in place.

To test if the presence of the shield and the magnetic field made any debris reduction, we performed AFM and spectral reflectance measurements on the Si samples, at each of the experiment setups shown in Figure 6.18 (a) original setup, (b) with the shield incorporated and (c) with the shield and in the presence of the magnetic field. With AFM, we determined a Ti deposited layer thickness of 15 nm in 6.18 (a), and 4 nm in 6.18 (b). It was very difficult to measure the thickness layer produced in 6.18 (b) and

nearly impossible in 6.18 (c). AFM measurements gave us a good calibration point in 6.18 (a) but was not as sensitive as our reflectometer in this case.

By studying the spectral reflectance, we successfully observed how the Ti edge changed in the different conditions. From Figure 6.19, we can qualitatively determine a reduction of the Ti absorption edge depth from the original setup through the incorporation of the shield and magnetic field, indicating a reduction of the amount of Ti deposited on the sample. The Ti absorption edge depth was reduced in the presence of the shield and the magnetic field, demonstrating a clear and significant debris mitigation under the new setup conditions.

This same experiment was performed a second time, under the same conditions but increasing the amount of debris generated by raising the amount of shots on the Ti target. The results obtained were consistent with the first set.

The magnets were mounted on an aluminium core keeping the poles separated by 1.1 cm from each other. Even with this modest magnetic field, the ion deflection was sufficient to reduce the debris. As a future suggestion, by reducing the distance between the poles we can increase the magnetic field by one order of magnitude (or more) and thus the influence over the ions, generating an even more effective debris mitigation.

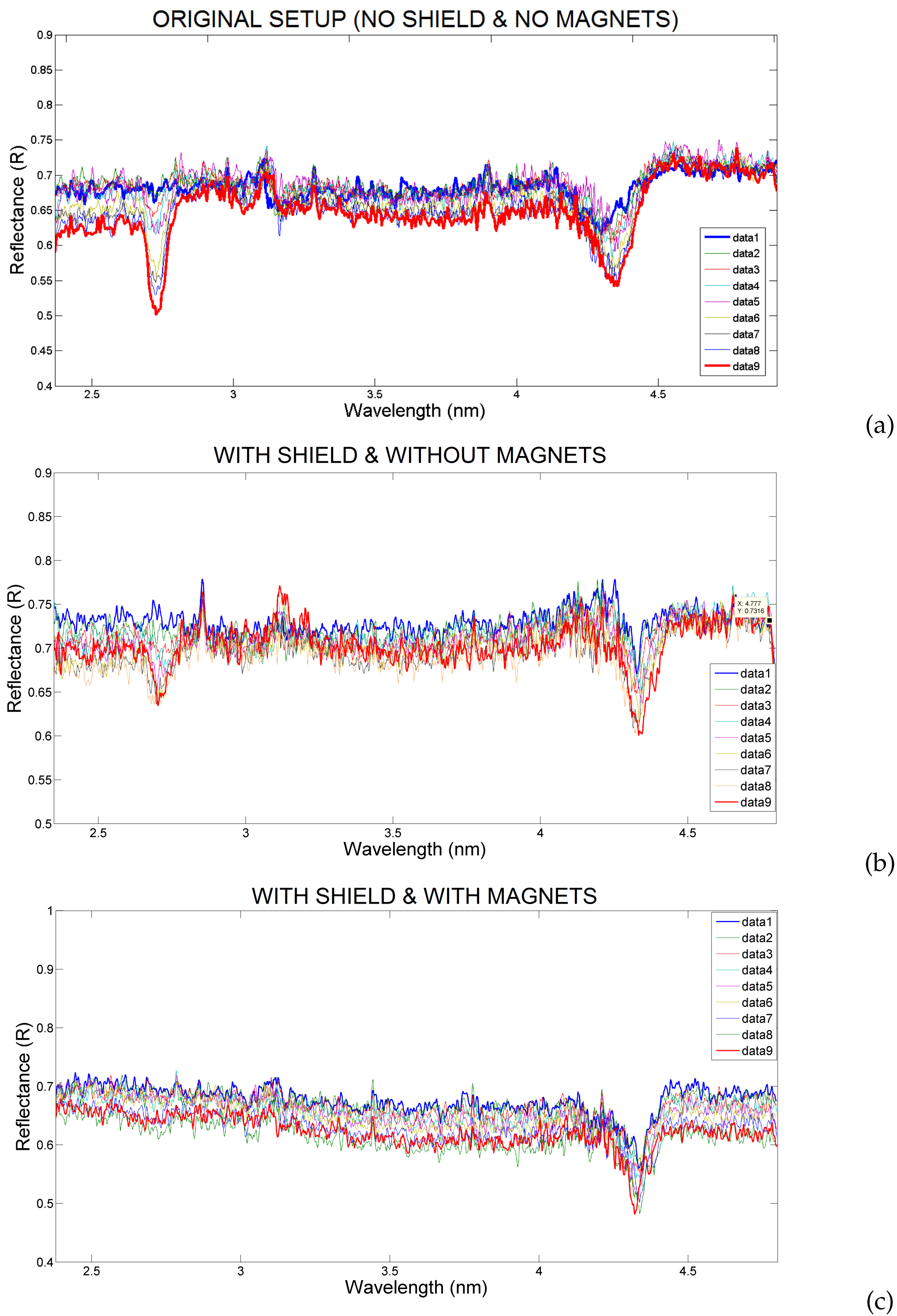


**Figure 6.19:** Reflectance results taken every 3000 shots at 550 mJ each, (a) with the original setup (absence of shield and magnets), (b) in the presence of the baffle shield and (c) in the presence of both shield and set of neodymium permanent magnets.

### 6.9.3 The importance of the reference spectra

It is a known fact and is well demonstrated in Section 6.9.1 and 6.9.2, that one major issue is the difficulty of designing a debris-free LPP source. The debris not only can contaminate the sample but also and sometimes more importantly can damage optical devices present in the setup under use.

In our case, the setup is very simple and the grating seems to be well protected from debris contamination behind an Al filter, and far from the LPP source. Nonetheless, the 75 mm lens used to focus the laser beam on the targets is located only ≈75 mm away from the source and very much in the way of the plasma plume generated. In order to preserve this optic from debris contamination, we placed a microscope glass slide as a protection cover. This is a changeable piece, but the vacuum needs to be broken to access it. This means that the glass remains under constant debris exposure during one long experiment.

When performing the debris experiment described in Section 6.18, we realized how the debris deposited on the glass affected the intensity of both beams (Straight through (ST) and Reflected (REF)) reaching the detector. As shown in Figure 6.20(a) and 6.20(b), the more debris covering the glass the more the intensity of both beams dropped off each time a reflectance measurement was taken. We generated debris shooting the Ti target 3000 times and took a reflectance measurement by performing 300 shots with W as the source. This cycle (3000 Ti shots + 300 W shots) was repeated several times.

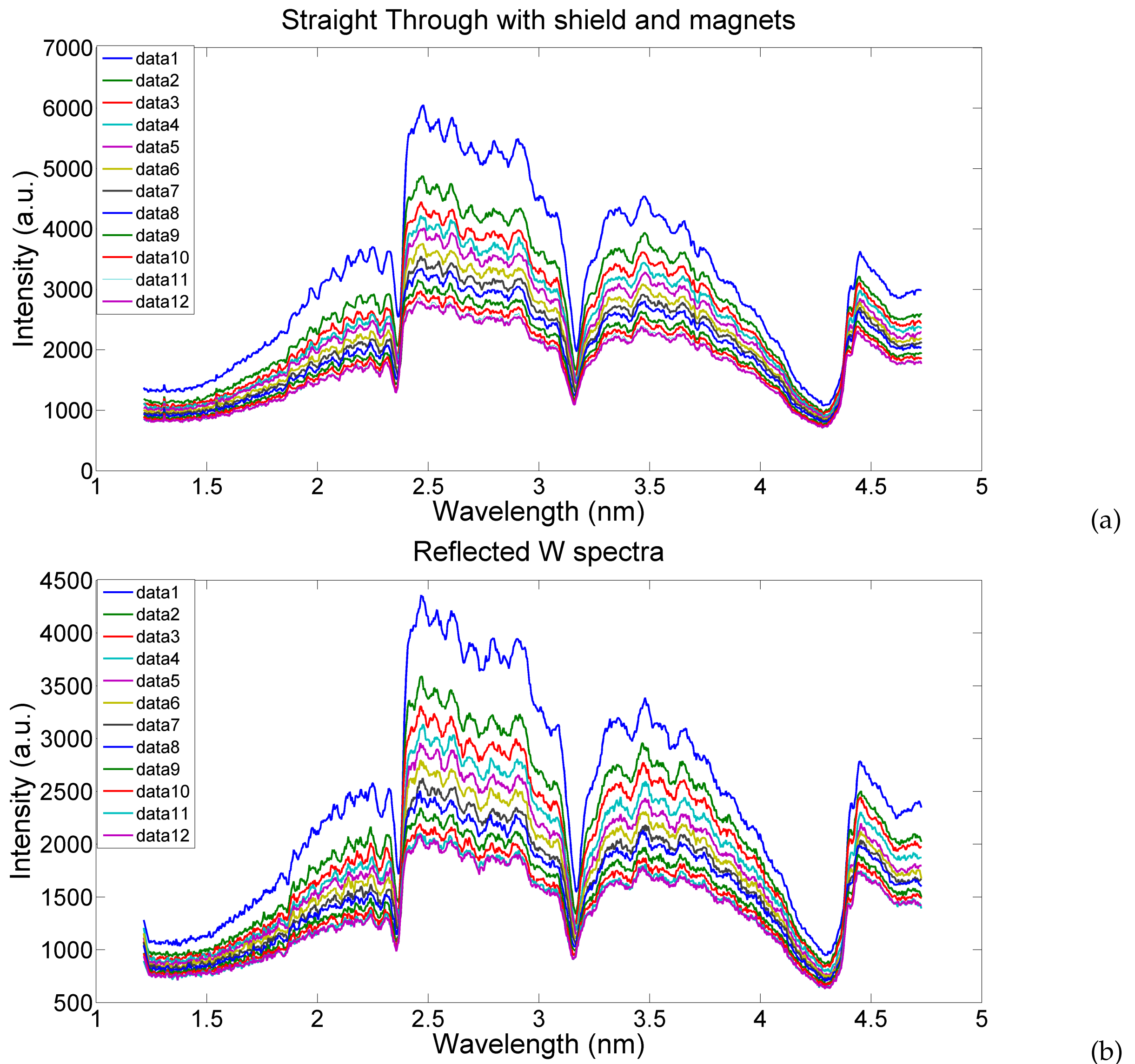


**Figure 6.20:** (a)Straight through and (b)Reflected beam intensity spectra drop off due to optics contamination after each cycle of 3000 shots at 550 mJ/shot on Ti target. Reflectance source target: W.

In Figure 6.21, the tendency of both beam intensities to drop off at several wavelengths is shown, the curves have been normalised to the highest point to make the interpretation easier. In both cases the behaviour is quite regular.

In conclusion, this demonstrates the importance and necessity of having a reference beam or straight through spectra acquired under the exactly same conditions as the reflected spectra. Otherwise it would be difficult to say what the spectral intensity of the plasma was for the set of 300 W shots used to make the measurements.

In this way, we are also accounting for fluctuations in the spectra due to fluctuations in the output of the laser and in the target purity, flatness, *etc.*, which indeed are parameters less easy to account for in the absence of the reference beam.

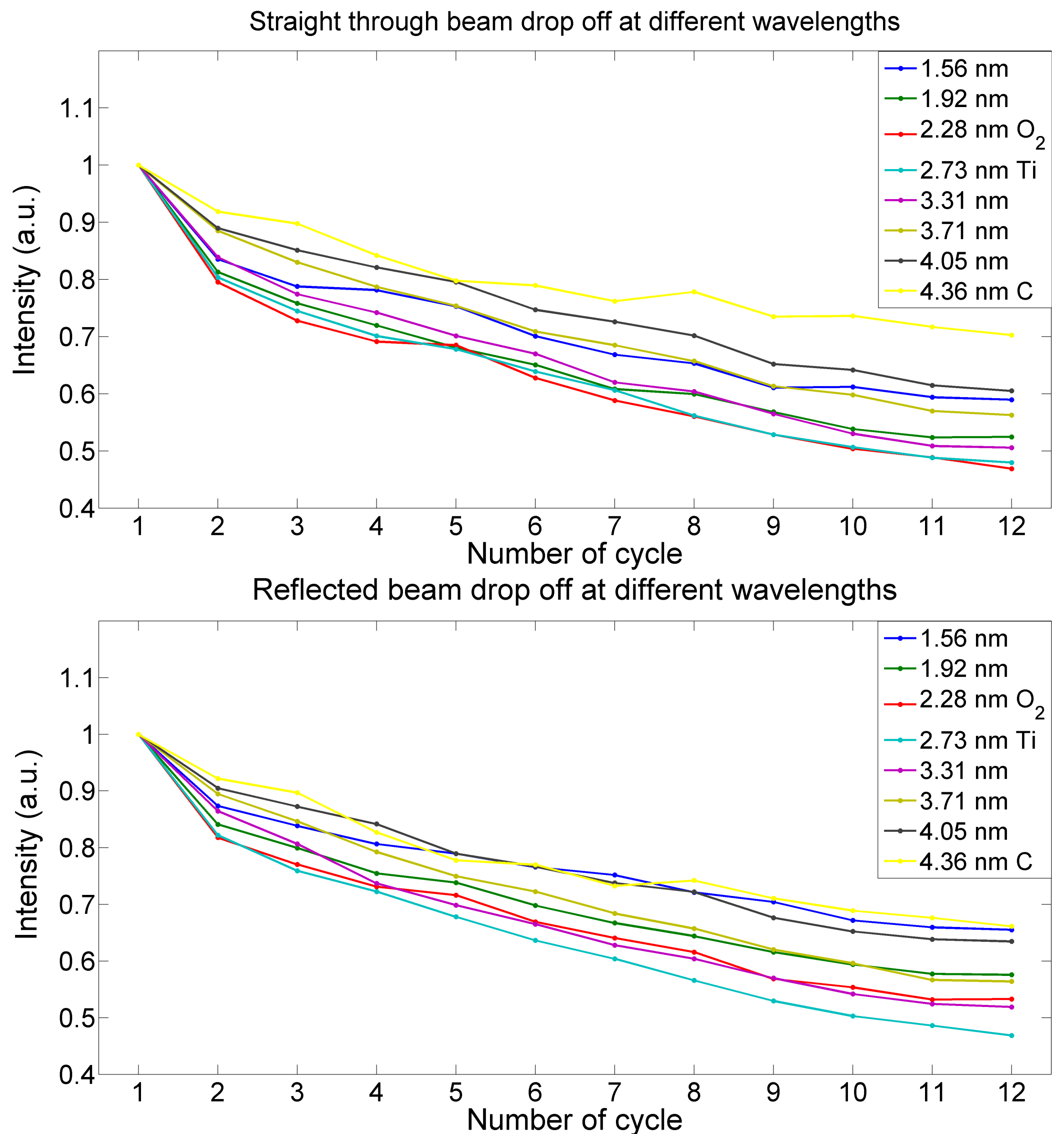


**Figure 6.21:** (a)Straight through and (b)Reflected beam intensity drop off tendency due to optics contamination after each cycle of 3000 shots at 550 mJ/shot on Ti target. All curves are normalised to the highest point. Reflectance source target: W.

### 6.9.4 Reflectometer spatial resolution

The spatial resolution of the reflectometer was tested in a simple experiment. For this task, we masked a 5x5 cm Si substrate with stripes of different widths using a permanent marker, as shown in Figure 6.22. The purpose was to determine which of these spatial separations would the spectral reflectometer resolve.

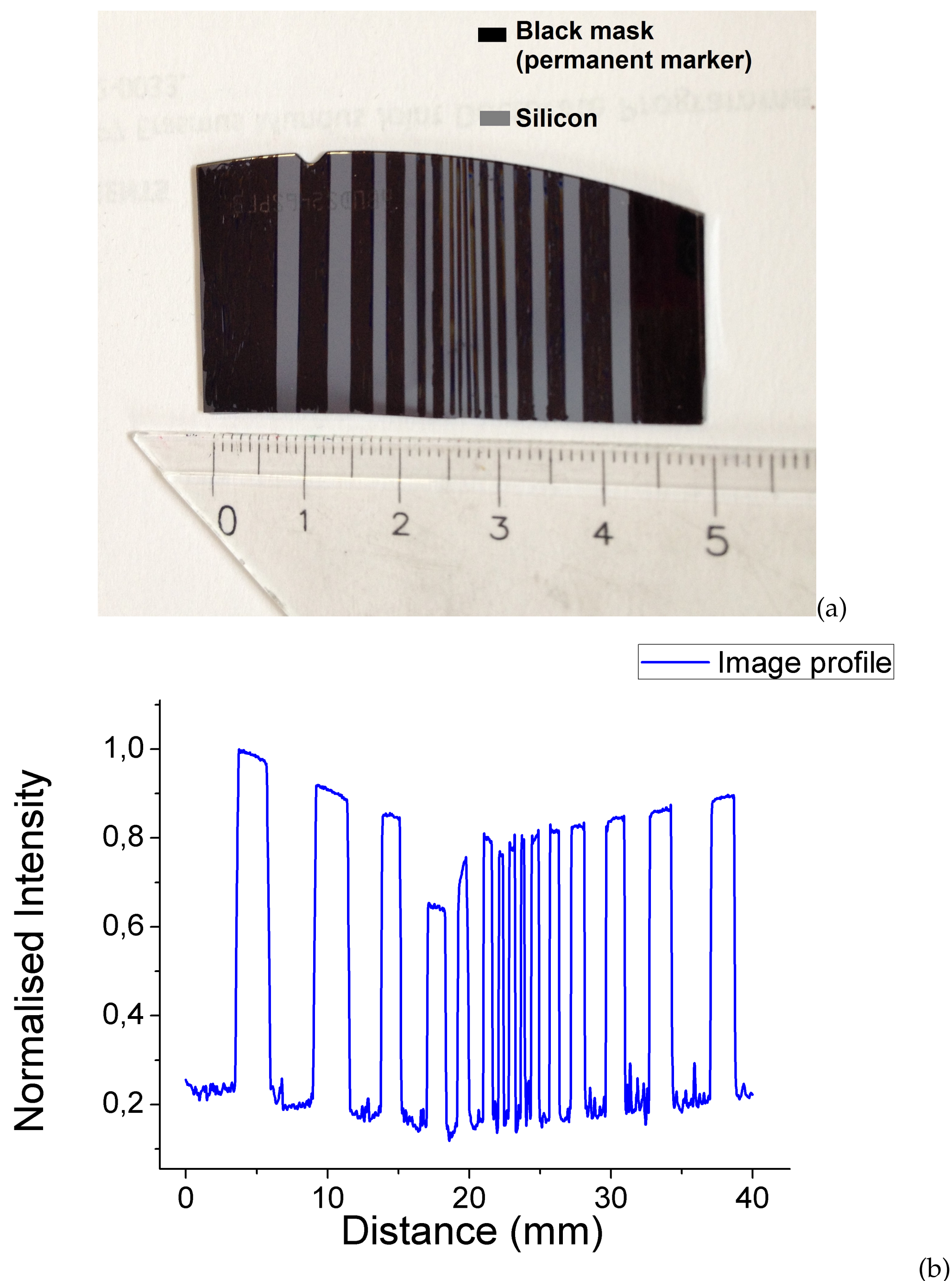


**Figure 6.22:** (a) Photograph of the masked sample and (b) its extracted profile.

From the borders to the center of the sample, two stripes of width 2 mm, two of width 1.5 mm, two of width 1 mm and three in the center of width 0.5 mm were left unmasked. These Si spaces (mask-free) reflect light, while the masked ones do not.
A schematic of the experiment is shown in Figure 6.23. The sample was placed in the holder with the stripes perpendicular to the optical path direction. From the dimensions of this setup at 2$^{o}$ grazing incidence angle, we estimated the area of the sample mapped by the reflectometer to be $\approx$ 20 mm in the direction parallel to the optic path.

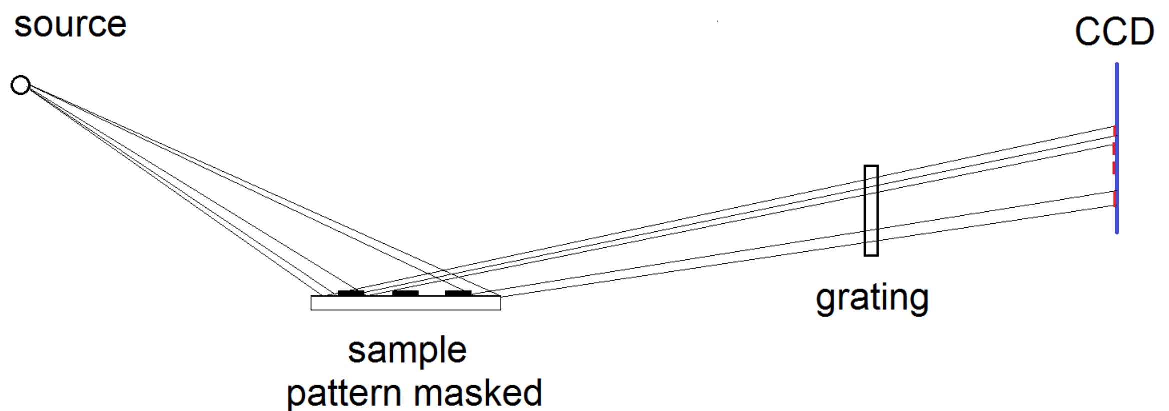


**Figure 6.23:** Schematic of the experiment to determine spatial resolution.

The image obtained with the reflectometer is shown in Figure 6.24 (a). To compare the measured and actual separations between the stripes we extracted a profile from both images, the reflected response on the CCD (Figure 6.24(a) top section) and the actual photograph of the masked sample (Figure 6.22(a)). The scale of the sample image was set using the ruler placed in the picture as a reference, while the scale of the reflected light profile was set only approximately by making basic geometrical considerations and trigonometry calculations. Knowing the source-detector (900 mm) distance and the angle of grazing incidence ($2^o$), the number of pixels illuminated by reflectance on the CCD can be correlated with the length (mm) of the illuminated area on the sample. The distance ratios between the peak separations on both profiles were calculated and compared, making sure the peaks of the sample image were correctly overlapped with the corresponding peaks of the spectrum image.

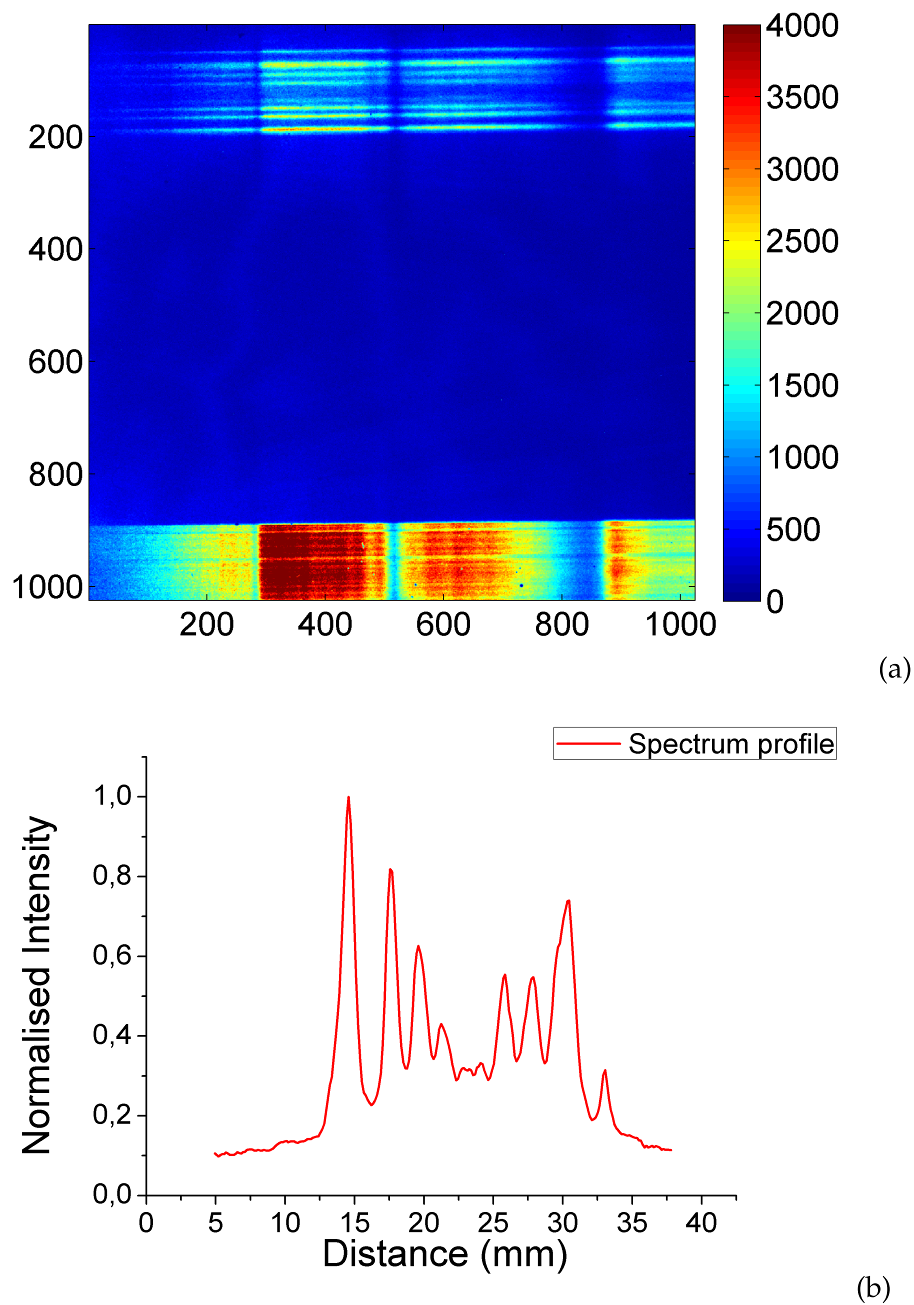


**Figure 6.24:** (a) Image obtained with the spectral reflectometer of the masked sample. (b) Extracted vertical profile of the reflected light (top section of image (a)).

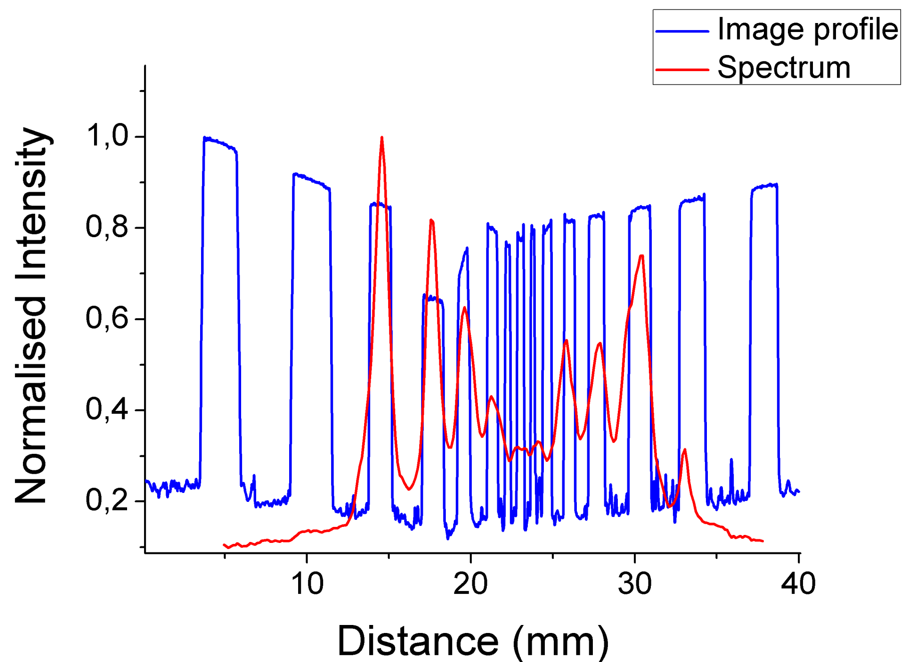


**Figure 6.25:** Profile obtained from the image of the sample overlapped with the vertical profile of the reflected light on the spectrum image.

In Figure 6.25, the two profiles are overlapped to determine which free-mask silicon stripes were mapped and resolved by the reflectometer. As observed, the two external Si stripes of 2 mm on each side were not mapped by the reflectometer and no signal shows for those stripes on the spectrum profile. The following 1.5 mm and 1 mm stripes are easily resolved, while the lines in the center part, of 0.5 mm thick, are not distinguished.

By measuring the full width at half maximum (FWHM) of the thinnest distinguishable stripe on the profile taken from the actual photo of the sample, we can say that the spatial resolution in the direction parallel to the optical path is approximately 1 mm, while in the direction perpendicular to the optical path, we can resolve approximately 20 $\mu$m as a result of the slit and source size.

The spatial resolution is an interesting aspect of the spectral reflectometer, especially when considering it useful to investigate samples that present non-uniform surfaces, and having the potential to identify features on different locations of the sample.

The reflectivity of the sample was also measured on the sections free of masking. The result is shown in Figure 6.26, were the carbon edge is clearly detected. This shows that the reflectometer could potentially give both spatial and spectral information for the sample under study.

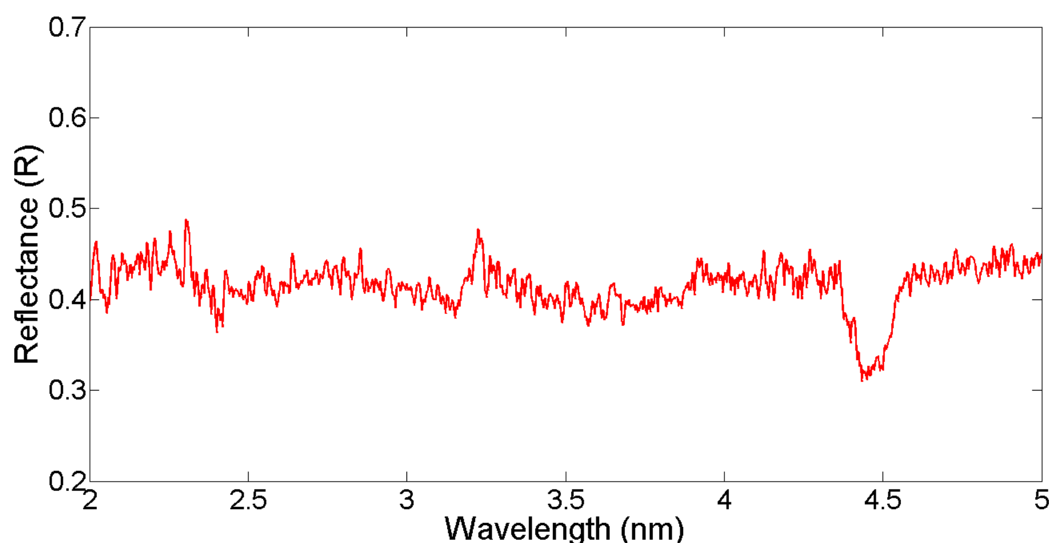


**Figure 6.26:** reflectance measurement of the masked sample. Showing the C absorption edge.

### 6.9.5 Testing the reflectometer: Bilayer samples.

The samples described in Subsection 3.4.3, were fabricated in Padova (Section 3.4) for the purpose of testing the potential uses of our reflectometer. Several layered samples with different elements in their different layers were prepared with e-beam deposition, mainly aiming to detect characteristic absorption edges of each element present in the sample.

We fabricated eight bilayer samples depositing Ti over Cr on a Si-substrate, and $TiO_2$ over Sc on a Si-substrate, varying the top and bottom layer thickness for each sample. Since all of them have had contact with air, in the IMD simulations we assumed a 1 nm C layer on the surface of every sample, and oxidation on the deposited layers.

From the The Center for X-Ray Optics (CXRO) webpage database [65], we calculated the penetration depth of radiation for the wavelength range in which we are working. For instance, for a 2° grazing incidence angle, radiation in the range 1.5-5 nm can penetrate $\sim$ 4 nm of Ti at $1/e$ drop off, except for energies closer to the Ti edge (2.73 nm) where the penetration depth increases up to 50 nm. This suggests that under our working conditions, we should be able to obtain information on the top layer, and in some cases, on the bottom layer too. It is important to notice that the information on the thickness of the deposited layers is only approximate and they are not rigorously characterised, uncertainty in the layer thickness is expected to be of the order of one nanometre.

The materials comprising the samples were chosen based on their relevance to soft X-ray and EUV applications. They are widely used as coating materials for optical devices, such as multilayer mirrors with high reflectivity output [17] [16] [20] [22] [23].

They also present absorption edges in the soft X-ray region accessible to the reflectometer.

### Sample M1

Sample M1 consisted of a 5 nm Ti layer over a 5nm Cr layer, on a Si-substrate.
Figure 6.27 shows the reflectance measured at the ELETTRA synchrotron in compared with the reflectance obtained in our reflectometer, both at 2° grazing incidence angle. The first measurement was performed approximately a year before the second one, with the set-up and experimental procedure as described in Section 5.3. The high spectral resolution achieved at the synchrotron makes well defined absorption edges easy to detect. On the other hand, even though our reflectometer has a lower resolution, we are able to detect all of the absorption edges associated with the elements present in the sample, that is O (K 1s=543.1 eV), Ti ($L_3$ $2p_{3/2}$=453.8 eV), Cr ($L_3$ $2p_{3/2}$=574.1 eV) and C (K 1s=284.2 eV) [1].

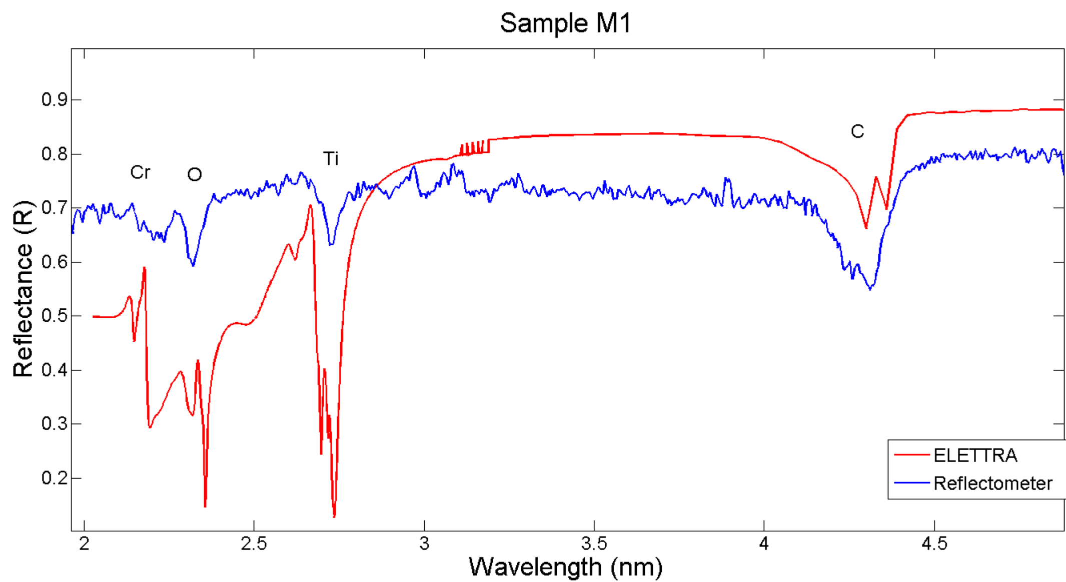


**Figure 6.27:** Reflectance of sample M1 measured at ELETTRA synchrotron and with our reflectometer.

In order to obtain the information in depth of sample M1, we performed an angular dependence reflectance study. The set-up only allows an angular variation over a small range below the critical angle of Ti ($\theta_C = \sqrt{2} \approx 2.7°$). The reflectance results at different grazing incidence angles, going from 2° to 1.35° with a step size of 0.16°, are shown in Figure 6.28. For comparison and represented as the red curve, we added the reflectance simulated with IMD of 1 nm of C over 5 nm of $TiO_2$ over 5 nm of $Cr_2O_3$ on a Si-substrate, at 2° grazing incidence. IMD permits to specify the instrumental spectral resolution that is to be simulated. Thus, for the sake of comparison, all IMD reflectance

curves are convolved assuming the reflectometer spectral resolution. Furthermore, all the IMD simulated curves were aligned with our measurements at the Ti absorption edge as it produced a common reference in all the measurements. In Appendix C, an example of how to simulate the reflectance of a bilayer sample and the important inputs in IMD are shown.

By changing the grazing incidence angle, what we are actually doing is a depth probe of the sample. In Figure 6.28, the reflectance of the sample measured at different grazing incidence angles show a clear angular dependence of the absorption edge "*depth*" (by "*depth*" here we mean 1-R) for the different elements in the different layers. This angular dependence is depicted in Figure 6.29. For the smallest grazing incidence angle, almost every edge disappear except for the shallow ones obtained for C and Ti. In this case, the information from the most superficial layer is obtained. With a greater angle of incidence, the edges of the rest of the elements become evident. This variation of the absorption edges shows a difference in penetration depth sensitivity for the different angles of illumination.

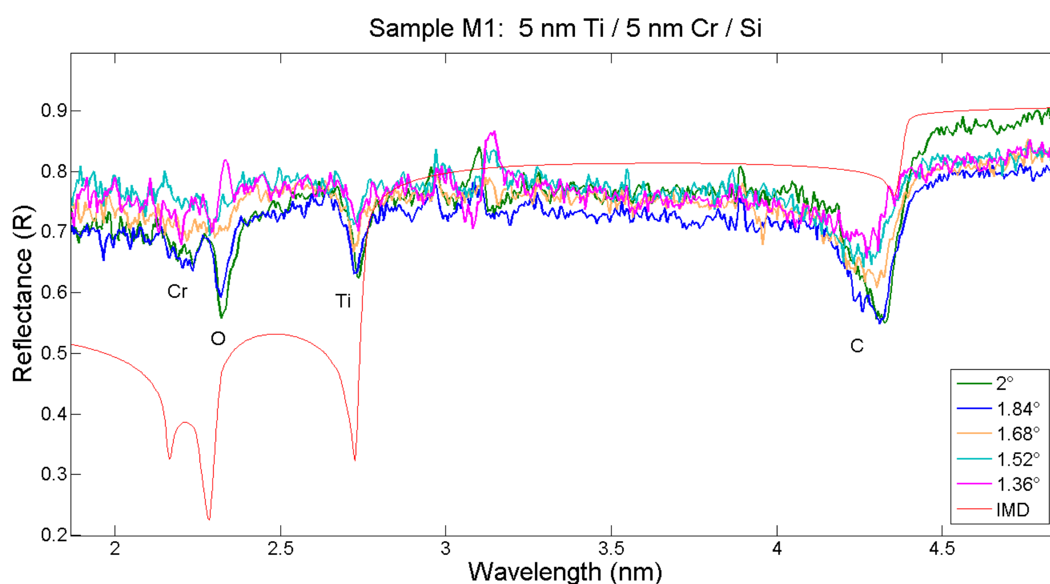


**Figure 6.28:** Reflectance of sample M1 measured at different incident angles. IMD simulation is calculated at 2° grazing incidence angle.

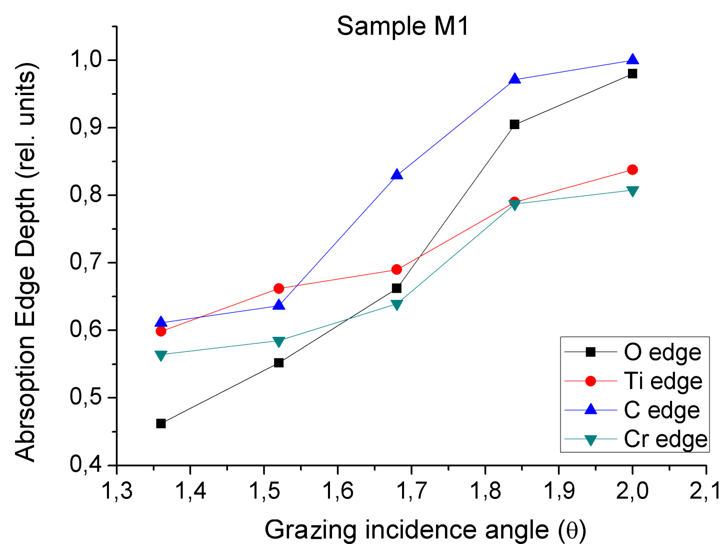


**Figure 6.29:** The angular dependence of the absorption edge "depth" for the different elements in the layers of the sample. Values are normalised with respect to edge of C at 2° grazing incidence angle.

### Sample M2

Sample M2 consisted of a 5 nm Ti layer over a 2 nm Cr layer, on a Si-substrate.
On this sample we performed a reflectance measurement at a 2° grazing incidence angle, to detect the elements present in the sample. As shown in Figure 6.30, Ti and C are clearly present, with little O and almost no Cr is detected. As a qualitative comparison we added the reflectance simulated with IMD for 1 nm C over 5nm $TiO_2$ over 2 nm $Cr_2O_3$ on a Si-substrate, convolved assuming the reflectometer spectral resolution.

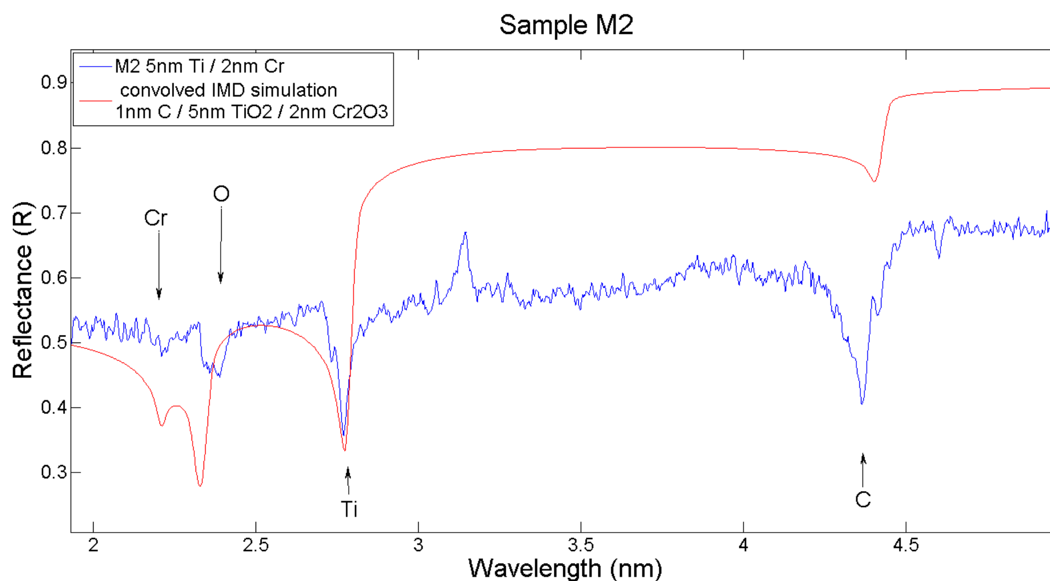


**Figure 6.30:** Reflectance of sample M2 and IMD simulation at 2$^o$ grazing incidence angle.

### 6.9.6 Spatial sample scanning

At this stage of the work, we introduced an extra actuator on the sample holder, which allowed horizontal movement in the direction perpendicular to the optical path. This provided an opportunity to introduce up to three samples in the chamber to measure reflectance, without interrupting vacuum. As a consequence, we were also able to measure reflectance at different surface zones of the same sample, by moving the holder in small distance steps. By performing these "spatial rasters", we expected to obtain information on the uniformity of the sample surface. In Figure 6.31, we present the results of reflectance measurement taken at a fixed grazing incidence angle ($\theta$=2°) at five different positions of M2 the sample, mapping the surface in steps of $\Delta x$=1 mm. All the curves are very consistent, backing up the hypothesis that the thin films deposition was uniform.

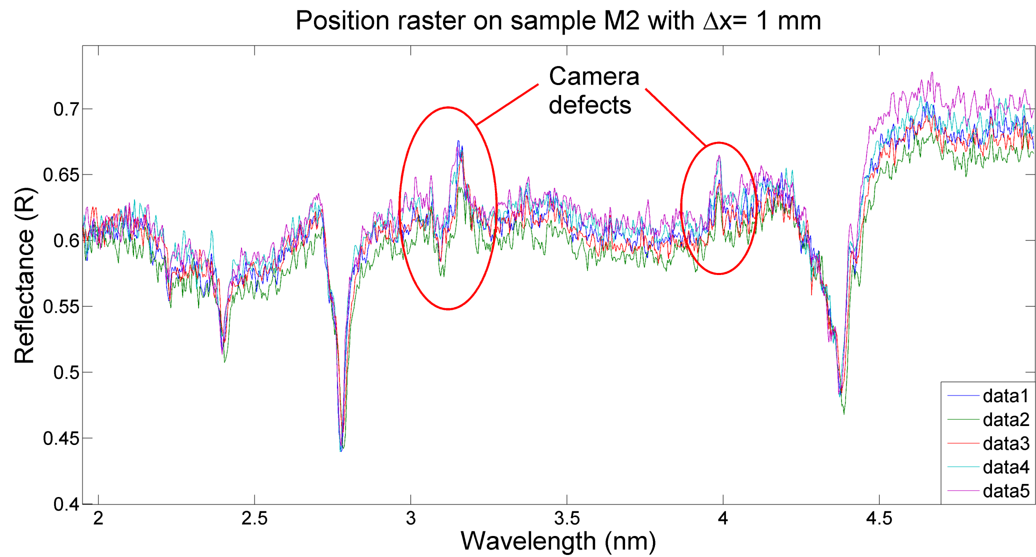


**Figure 6.31:** Reflectance of sample M2 making a position raster with a size step of 1 mm.

### Sample M3

Sample description: 3 nm Ti layer over a 5nm Cr layer, on a Si-substrate. In Figure 6.32 we qualitatively compare our reflectance measurement with a simulation performed with IMD, assuming a 1 nm C layer over a 3 nm $TiO_2$ layer over a 5 nm $Cr_2O_3$ layer at 2° grazing incidence and convolved assuming the reflectometer spectral resolution. The absorption edges of O, Cr, Ti and C were identified. It is important to notice, that for all the bilayer samples analysis, the comparison with IMD simulations is only qualitative in terms of reflectance and absorption edges presence. To make a quantitative comparison a more extensive knowledge of thickness, chemical composition and optical constants of the layers would be required, which was not the aim at this point in the work, and thus such studies were not performed for these particular samples. The setup limitations described in Section 6.7 (low spectral resolution and source intensity, spatial/mechanical and angular limitations) play also an important role in limitating the feasibility of a quantitative study.

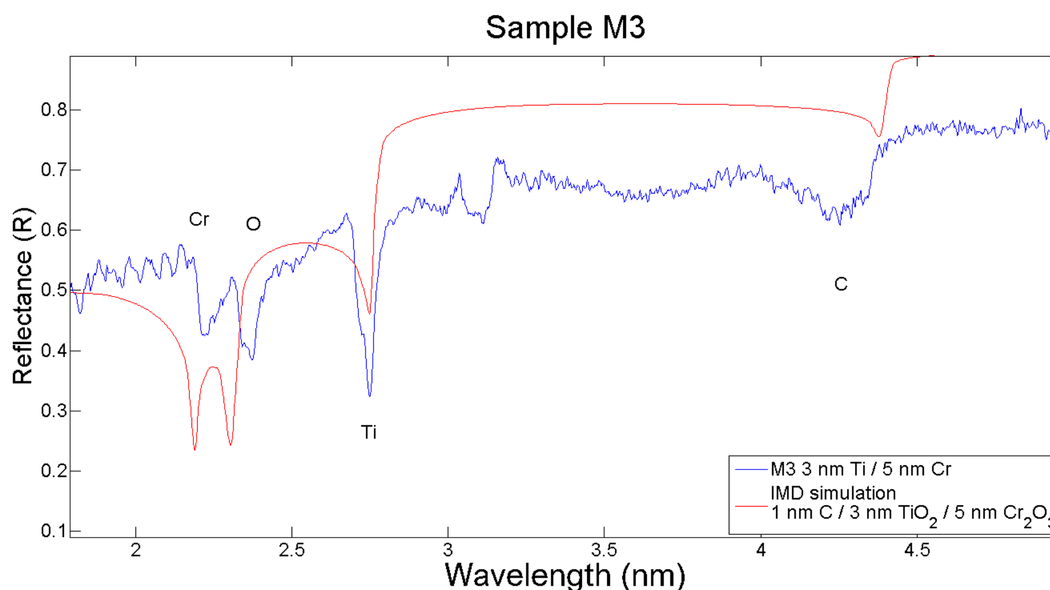


**Figure 6.32:** Reflectance of sample M3 and IMD simulation at a $2^o$ grazing incidence angle.

In Figure 6.33, we compare the results for samples M2 and M3 and observe how reflectance and the presence of absorption edges are affected by varying the top and the bottom layer thickness. The most obvious difference between the two profiles is the depth of Ti edge. Considering the penetration depth of the incident radiation, the results are consistent with the fact that for M2, Ti is the element mostly being probed since it is present in the top layer and its thickness is greater than for M3, where radiation barely reaches the Cr bottom layer. For the reflectance of sample M3, the absorption edges associated to Ti and Cr are both present, suggesting that the thinner top layer has been penetrated and radiation reaches the bottom layer. This variations of the absorption edges show a sensitivity to the different thickness values of the top layer.
Again, it is worth emphasising that this setup has low resolution and spectra are noisy, and with some minor redesign much higher sensitivity could be achieved.

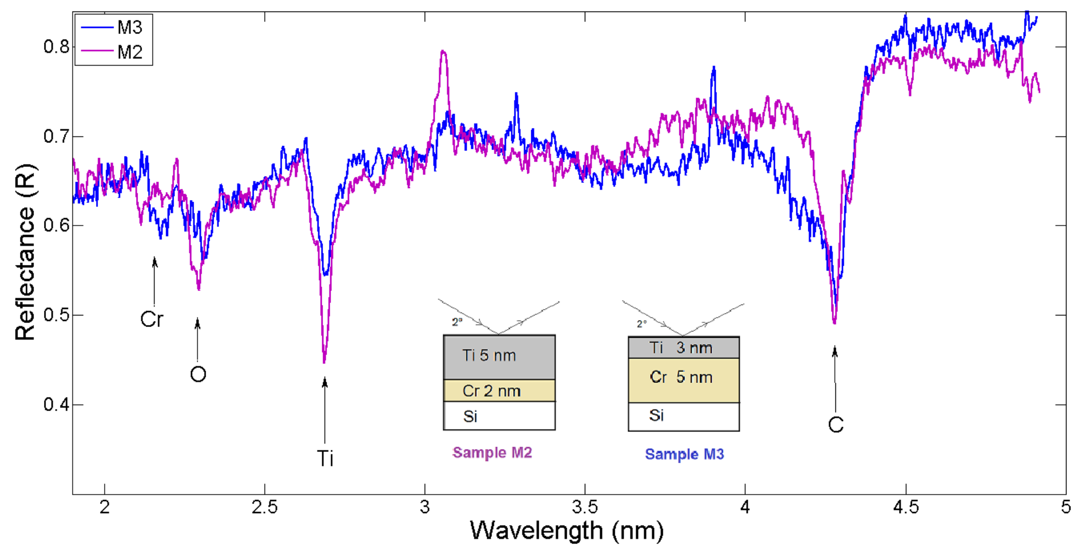


**Figure 6.33:** reflectance of sample M3 and M2.

### Sample M4

Sample description: 3 nm Ti layer over a 2nm Cr layer, on a Si-substrate. In Figure 6.34 our reflectance measurement along with a simulation performed with IMD, are shown, assuming a 1 nm C layer over a 3 nm $TiO_2$ layer over a 2 nm $Cr_2O_3$ layer at 2° grazing incidence and convolved assuming the reflectometer spectral resolution. The absorption edges of O, Cr, Ti and C are clearly identified.

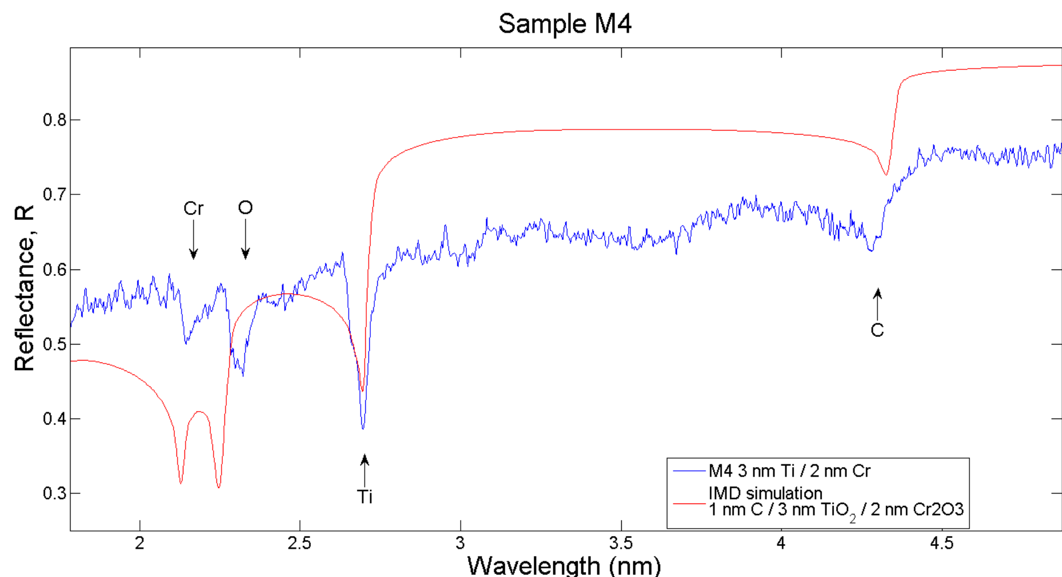


**Figure 6.34:** Reflectance of sample M4 and IMD simulation at a $2^o$ grazing incidence angle.

### Sample M5

Sample M5 consisted of a 5 nm $TiO_2$ layer over a 5 nm Sc layer, on a Si-substrate.
On this sample we performed a reflectance measurement at 2° grazing incidence angle, to detect the elements present. As shown in Figure 6.35, O, Ti, and C absorption edges are clearly detected in the sample, while Sc ($L_3$ $2p_{3/2}$=398.7 eV) [1] is present also but less evident. As a qualitative comparison we added the reflectance simulated with IMD of 1 nm C over 5 nm $TiO_2$ over 5 nm Sc on a Si-substrate, at 2° grazing incidence and convolved assuming the reflectometer spectral resolution.
In Figure 6.36, we present the results of reflectance measurement taken at a fixed incidence angle ($\theta$=2°) at four different positions of the sample, mapping the surface in steps of $\Delta x$=1 mm. All of the curves are very consistent, once more backing up the hypothesis that the thin film deposition was uniform.

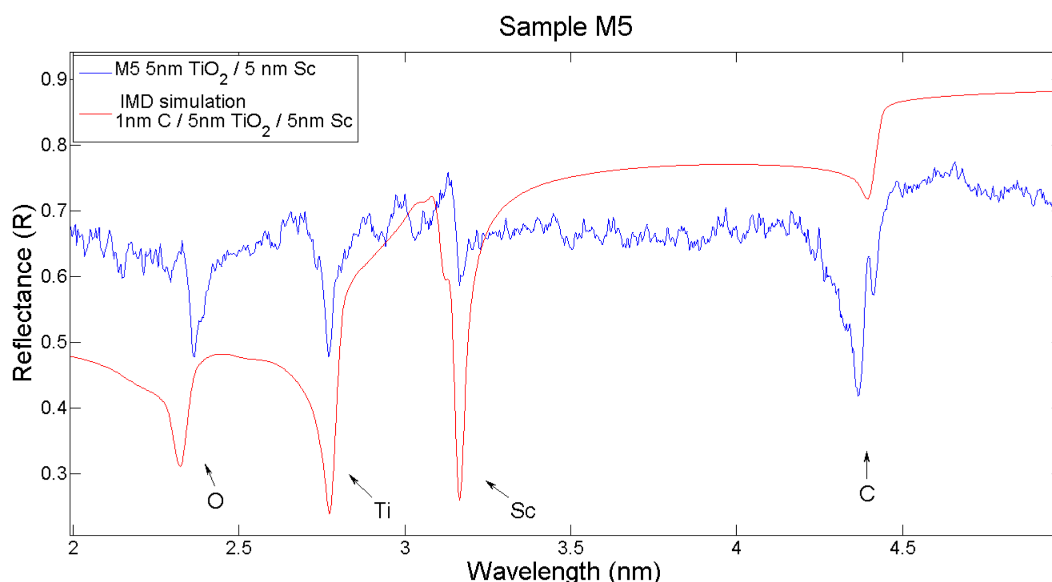


**Figure 6.35:** Reflectance of sample M5 and IMD simulation at a 2° grazing incidence angle.

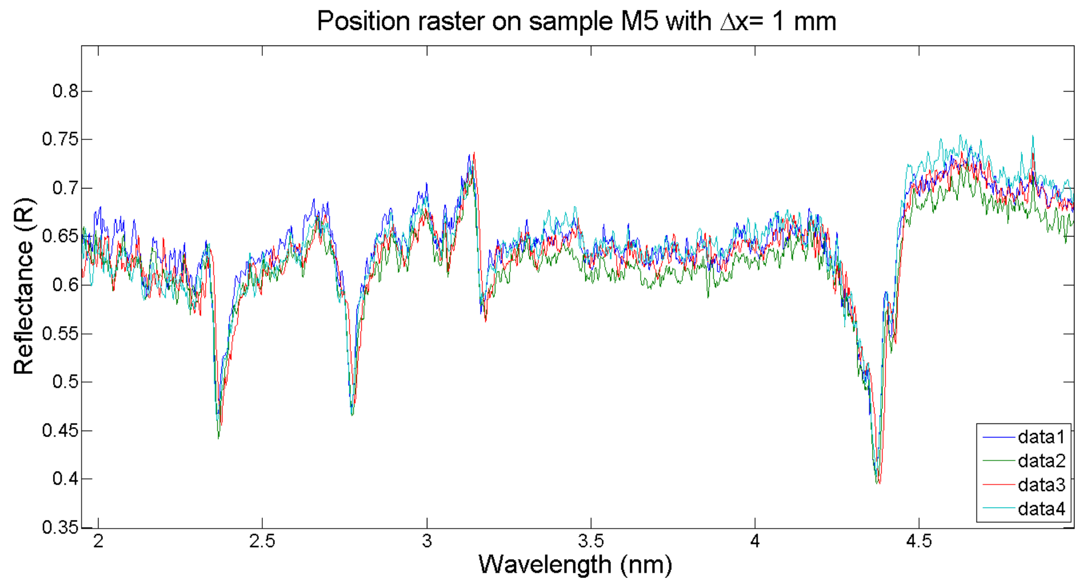


**Figure 6.36:** Reflectance of sample M5.

### Sample M6

Sample M6 consisted of a 38 nm $TiO_2$ layer over a 55 nm Sc layer, on a Si-substrate.
On this sample we performed a reflectance measurement at 2° grazing incidence angle, to detect the elements present. As shown in Figure 6.37, O, Ti, and C absorption edges are clearly detected, while the absorption edge associated to Sc is not seen. As a qualitative comparison we include the reflectance simulated with IMD of 1 nm C over 38 nm $TiO_2$ over 55 nm Sc on Si-substrate, for a 2° grazing incidence measurement and convolved assuming the reflectometer spectral resolution.
The $TiO_2$ top layer is evidently too thick to be penetrated by the radiation, thus it is consistent with the reflectance results not showing a Sc edge, whilst C, Ti and O can be clearly identify as elements in the sample.

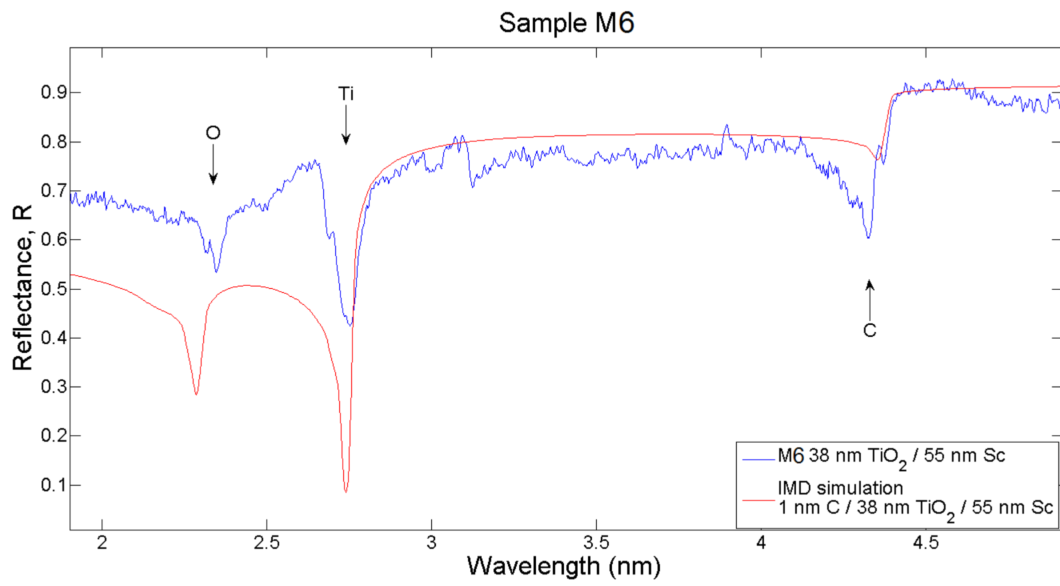


**Figure 6.37:** Reflectance of sample M6 and IMD simulation at a 2$^o$ grazing incidence angle.

# Chapter 7

# Concluding remarks

In this work, we measured angle-dependent reflectance in the 25.5- to 612-eV energy range, of amorphous $TiO_2$ thin films of different thicknesses deposited with e-beam evaporation technique. The experimental reflectance profiles were fitted to simulated profiles based on a well-defined optical model, by means of a genetic algorithm applied to a least-square curve fitting method. To the best of our knowledge, we have obtained the first experimental values for $\delta$ and $\beta$ of amorphous $TiO_2$ over this energy range. The surface roughness, thickness, and chemical composition of the samples were independently analysed. Overall, we were able to obtain successful fittings at all energies, deriving the optical constants with an uncertainty of 10%. The real structure of the sample was modeled with an additional native oxide layer on top of the substrate and a surface contamination layer. By assuming an approximated optical model, we introduced systematic errors in the calculations. A study of buried interlayers formed due to the growth process was carried on based on the optical response near the soft X-ray absorption edge of $TiO_2$. The data presented here provide an important contribution by presenting a well-characterised set of photon energies, for $TiO_2$ thin films, which is of considerable industrial and academic interest, granting as well, a foundation for a future study with higher energy sampling frequency around the absorption edges.
We tested and further developed a table-top spectral reflectometer used as a thin film characterisation technique. The work was focused on producing a self-referencing grazing incidence reflectometer based on a laser produced plasma (LPP) source working in the soft X-rays spectral range. Several bilayer samples of Cr, Ti,$TiO_2$ and Sc were produced to test the reflectometer. Chemical composition, depth probe and spatial scanning studies were performed on the samples. The reflectometer was relatively simple to use, providing a fast and reasonably accurate reflectance measurement. As already mentioned in previous chapters, the reflectometer was a very crude and prototype-like system with known noise problems, thus, the results indicate early stage potential rather than final results. Nonetheless, we were able to show the potential of the spectral reflectometer as a characterisation tool with the multilayer samples and to demonstrate function and provide a proof of concept demonstration.

# Appendix A

## Ion magnetic deflection

In this appendix, we performed a simple theoretical calculation to estimate some of the important parameters to predict the deflection of the plume direction with respect to the target normal and thus to the shield slit position in the presence of a magnetic field (Section 6.9.2). To do so, we assumed a minimum magnetic field of 0.05 T, uniform along the plume expansion direction. The target surface is placed at a distance of $\approx$ 1 mm from the magnets edges. The ions propagating from the source and crossing through the magnetic field volume zone (1.5x2.5x1.1 $cm^3$), are subjected to the influence of the magnetic field and so to the corresponding Lorentz force. This is $F_L$=$|\overline{\mathbf{F}_L}|$=$|q||\overline{\mathbf{v}}X\overline{\mathbf{B}}|$=$|q|vB\sin\theta$, where $q$ is the charge, $v$ the velocity of the ion, $B$ the magnetic field of the neodymium magnets and $\theta$ the angle between $\overline{\mathbf{v}}$ and $\overline{\mathbf{B}}$. The velocity can be expressed as: $v_{ion} = \sqrt{\frac{2.E_{ion}}{m_{ion}}}$. For singly charged Ti ions of energy 10 KeV we calculated a lateral deflection of 0.737 mm from the shield's slit position.

$$k_b := 1.380658 \cdot 10^{-23} \cdot \frac{joule}{K}$$

$$AMU \equiv 1.6605402 \cdot 10^{-27} \cdot kg$$

$$h := 6.6260755 \cdot 10^{-34} \cdot joule \cdot sec$$

$$me := 9.1093897 \cdot 10^{-31} \cdot kg$$

$$\varepsilon o := 8.854187817 \cdot 10^{-12} \cdot farad \cdot m^{-1}$$

$$q_e \equiv 1.60217733 \cdot 10^{-19} \cdot coul$$

$$nm := 10^{-9} m$$

$$\mu m := 10^{-6} m$$

$$ns := 10^{-9} sec$$

$$mJ := 10^{-3} J$$

$$mW := 10^{-3} W$$

$$eV \equiv q_e \cdot volt$$

$$keV \equiv 10^3 eV$$

$$v_{ion} := \sqrt{\frac{2 \cdot E_{ion}}{m_{ion}}} \qquad v_{ion} = 1.965 \times 10^7 \frac{cm}{sec}$$

$$F_{ion} := q_e \cdot v_{ion} \cdot B_{neodymium} \qquad F_{ion} = 1.574 \times 10^{-15} N$$

$$a_{ion} := \frac{F_{ion}}{m_{ion}} \qquad a_{ion} = 1.895 \times 10^{10} m\, s^{-2}$$

$$MagnetSize := 15mm$$

$$TransitTime := \frac{MagnetSize}{v_{ion}} \qquad TransitTime = 76.354\, ns$$

$$Deflection := \frac{1}{2} a_{ion} \cdot TransitTime^2 \qquad Deflection = 0.055\, mm$$

$$DeflectionAngle := atan\left(\frac{Deflection}{MagnetSize}\right) \qquad DeflectionAngle = 3.683 \times 10^{-3}$$

$$ShieldDistance := 200mm$$

$$DeflectionAtShield := DeflectionAngle \cdot ShieldDistance$$

$$DeflectionAtShield = 0.737\, mm$$

$$B_{neodymium} \equiv 0.05T \qquad m_{ion} \equiv 50AMU \qquad E_{ion} \equiv 10keV$$

$$v_{ion} = 1.965 \times 10^7 \frac{cm}{sec}$$

# Appendix B

## MATLAB code for spectra calibration and reflectance measurement

In this Appendix, the MATLAB code to extract and analyse the data collected is shown. It allows to obtain the source target spectrum and the reflected light spectrum from the sample under study and then to take the ratio between the reflected signal over the straight through signal $S_{REF}/S_{ST}$.

```
clear all;close all; clc
img=readSPE('img_1.SPE'); %Opens the CCD image

%BEGINS CALIBRATION SECTION
%select RBSN image p for calibration
p=1;
%Range selection from top to bottom where the ST and REF spectra appear
figure(1);imagesc(img(:,:,p),[0,13000])
[a, b] = ginput (4);
I=int16(b);
RBSN_sum=sum(img(I(3):I(4),:,p));
RBSN_sum_R=sum(img(I(1):I(2),:,p));
```

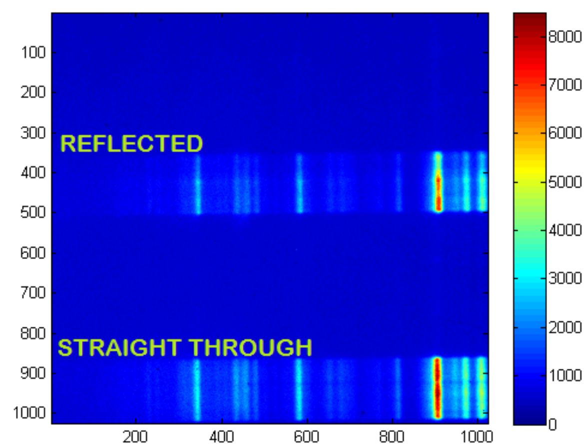

```
%Selects six points to calibrate the ST spectra
figure(2);plot(1:1024,RBSN_sum)
[c, d] = ginput (6);
ST= c;
save CalibST.txt ST -ASCII;
%Selects six points to calibrate the REF spectra
figure(3);plot(1:1024,RBSN_sum_R)
[e, f] = ginput (6);
REF= e;
save CalibREF.txt REF -ASCII;
```

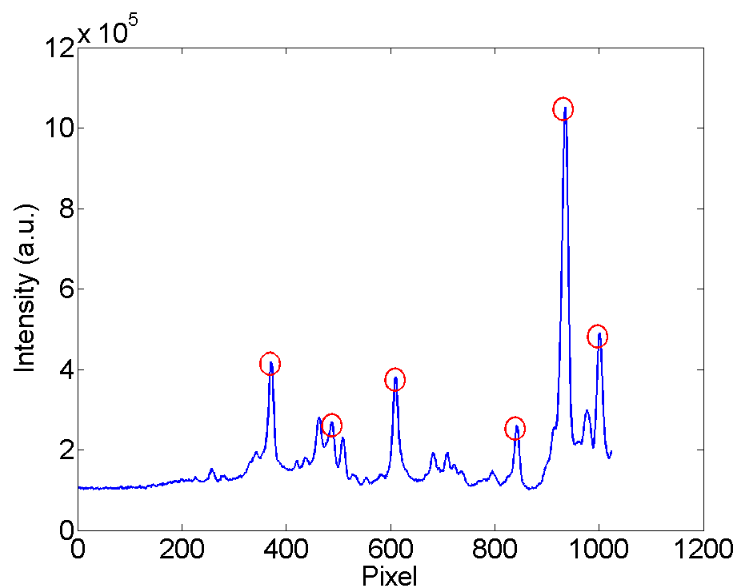


```
%Loads the six reference points and the previously selected
 points for calibration
cal=load('Calib.txt');
calST=load('CalibST.txt');
calREF=load('CalibREF.txt');

%Calibration by curve fitting
p=polyfit(calREF(:,1),cal(:,1),3);
p1=polyfit(calST(:,1),cal(:,1),3);
x=1:1024;
yREF=polyval(p,x);
yST=polyval(p1,x);
stepsize=0.0005;
x=min(yST):stepsize:max(yST);
RBSNS=interp1(yST,(RBSN_sum),x,'linear','extrap');
```

```
RBSNR=interp1(yREF,(RBSN_sum_R),x,'linear','extrap');
R_SN=RBSNR./RBSNS;
figure(4);plot(x,RBSNS,x,RBSNR)
figure(5);plot(x,R_SN)
%END OF CALIBRATION SECTION
```

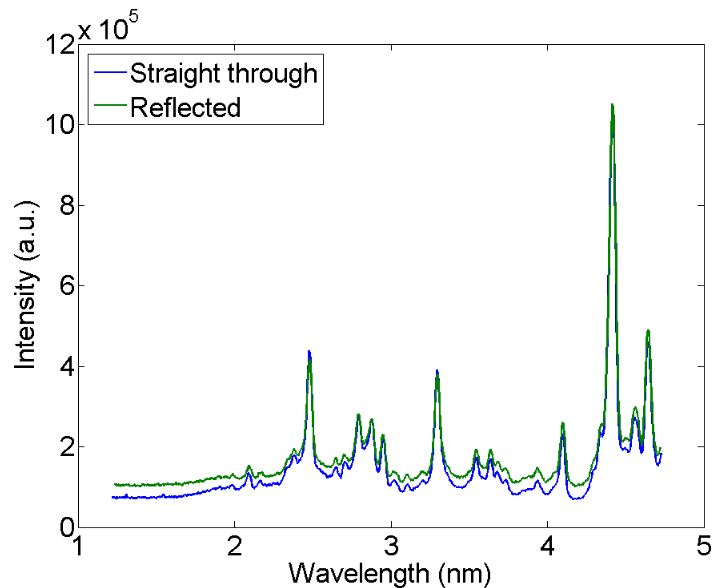


```
%REFLECTIVITY MEASUREMENT SECTION
%CCD image selection
d=2;

%range selection from top to bottom of REF and ST spectra
figure(6);imagesc(img(:,:,d),[0,10000])
[a, b] = getpts(figure(1));
I=int16(b);
rows_straight = I(4) -I(3);
rows_R = I(2)-I(1);
Target_sum=sum(img(I(3):I(4),:,d))/double(rows_straight);
Target_sum_R=sum(img(I(1):I(2),:,d))/double(rows_R);
```

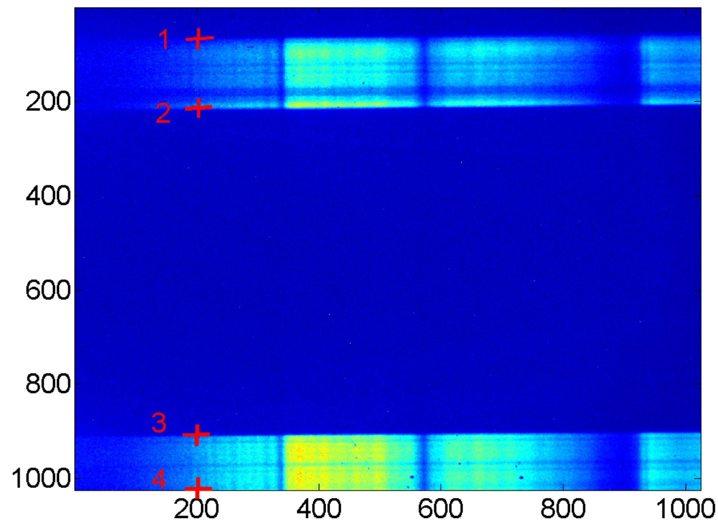


```
%reflectivity calculation by dividing ST over REF spectra
using previous calibration
TargetS=interp1(yST,(Target_sum),x,'linear','extrap');
TargetR=interp1(yREF,(Target_sum_R),x,'linear','extrap');
R_SN=TargetR./TargetS;
figure(7);plot(x,TargetS,x,TargetR)
figure(8);plot(x,R_SN)%,'color',color1)
%END OF REFLECTIVITY MEASUREMENT SECTION
```

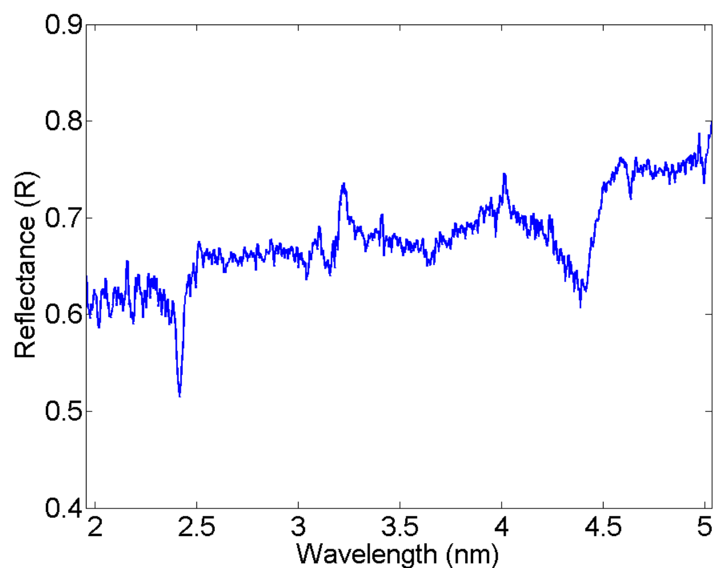

## Appendix C

# IMD Software for reflectance simulation

In this appendix, an example of how to simulate the reflectance of a bilayer sample (optical model) using the IMD software [55] is shown. The bilayer is composed by a 5 nm Ti layer over a 5 nm Cr layer on a Si-substrate. The reflectance is calculated for a $2^o$ grazing incidence angle in the 1.5-5 nm wavelength range. First we select the substrate material, then we add the "layer" by clicking on the "Add layer" button situated at the bottom of the Structure area (with the horizontal blue bar "layer" icon). The corresponding Layer window appears:

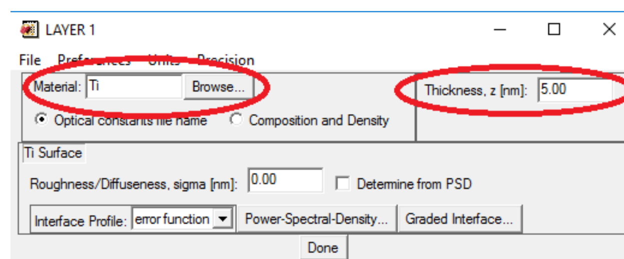


For this example we selected the material Ti and the thickness 5 nm for the top layer and Cr of 5 nm thickness for the bottom layer.
Next, as we want to compute the reflectance of the bilayer, we check the box labelled "Reflectance, Phase, Psi, Delta" in the main IMD window. Next, we click the "Independent variables" tab:

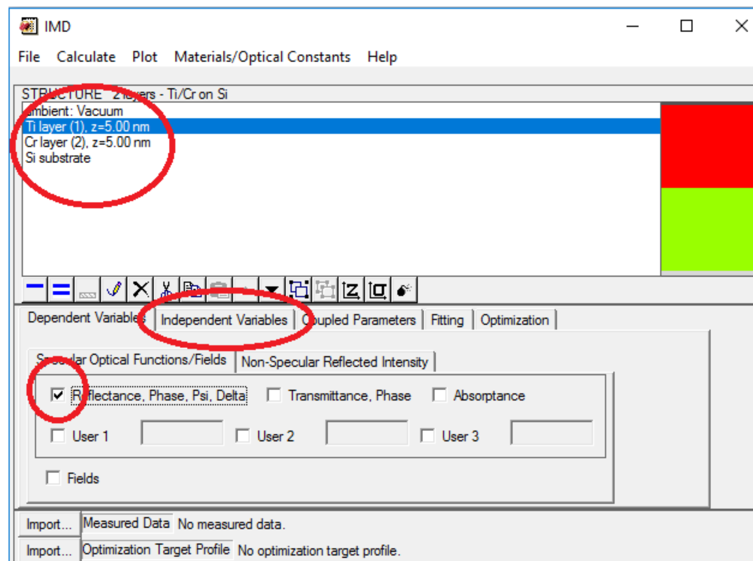


After clicking the "Independent variable" tab, we double-click the item "Wavelength, Lambda", to specify the range of wavelengths to compute for the reflectance and the instrumental spectral resolution ($\Delta\lambda$). In this example we selected 100 wavelength values from 1.5 nm to 5 nm with a resulting step size of 0.035 nm and $\Delta\lambda$=0.05.

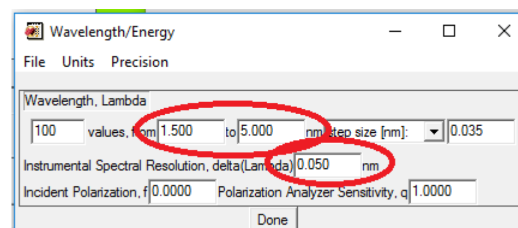


As the next step we enter the incidence angle value, for this example we selected $2^o$ grazing incidence.

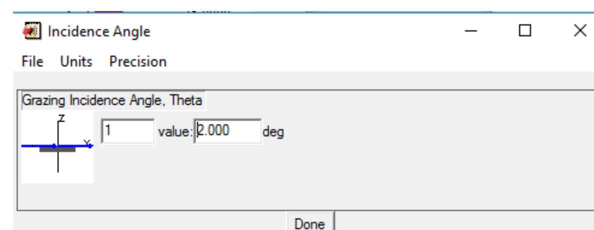


Finally, to perform the computation, we click on "Calculate" from the manu bar at the top part of the main IMD window and then "Specular Optical Functions/Fields". After the calculation is complete, the results appear in an IMDXPLOT window:

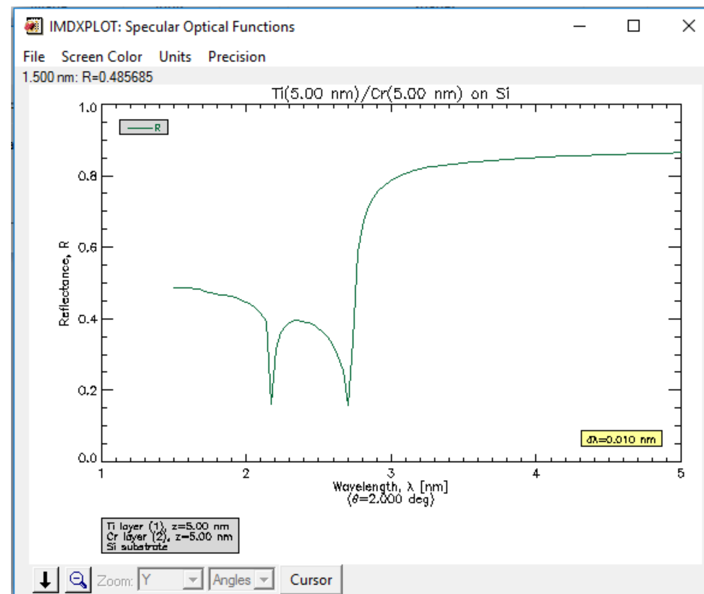
IMDXPLOT: Specular Optical Functions
File
Screen Color
Units
Precision
1.500 nm: R=0.485685
Ti(5.00 nm)/Cr(5.00 nm) on Si
R
Reflectance, R
1.0
0.8
0.6
0.4
0.2
0.0
1
2
3
4
5
Wavelength, λ [nm]
(θ=2.000 deg)
dλ=0.010 nm
Ti layer (1), z=5.00 nm
Cr layer (2), z=5.00 nm
Si substrate
Zoom:
Y
Angles
Cursor

## List of Figures


1.1 The electromagnetic spectrum shown from the infrared (IR) to the X-ray regions [1]. . . . 2

2.1 Incident plane wave in the interface between uniform and isotropic media $\mathbf{n}_1$ and $\mathbf{n}_2$ [26]. . . . 11
2.2 Multiple reflections in a thin layer of thickness d [26]. . . . 13
2.3 Schematic of the iterative process to obtain the reflectance and transmittance of multilayer structures [26]. . . . 15

3.1 Schematic of the electron beam gun unit [35]. . . . 19
3.2 Schematic of the evaporation from (a) a point source and (b) a surface source [33]. . . . 21
3.3 Calculated vapor clouds effusion from a source with different cosine exponents [33]. . . . 22
3.4 Film thickness uniformity for point and small surface sources. (Insert) Schematic of the geometry of evaporation onto a plane-parallel substrate [33]. . . . 23
3.5 E-beam chamber system at LUXOR laboratory. . . . 24
3.6 Tooling inside the e-beam chamber deposition. (1) QCM, (2) heater lamps, (3) rotating substrate holder, (4) shutter, (5) crucible holder and (6) e-beam gun unit. . . . 25
3.7 Samples of $TiO_2$ thin film deposited on Silicon (100) substrate . . . . 28

4.1 Stylus profilometer technique to measure film thickness . . . . 34
4.2 Schematic of the typical and main parts of a spectroscopic ellipsometer [43]. . . . 35
4.3 Basic configuration of an Atomic Force Microscope [45]. . . . 36
4.4 Atomic Force Microscope working modes . . . . 37
4.5 Schematic of the photoemission process that occurs on the XPS technique. The atom is photoionized after a 1s electron is ejected [47]. . . . 38
4.6 XPS electron spectra of a $TiO_2$ sample . . . . 39

5.1 Two dimensional AFM images of the TiO2 thin film surfaces of (a) sample Eb1, (b) sample Eb2 and (c) sample Eb3. . . . 43
5.2 XPS survey spectra from the $TiO_2$ samples. . . . 44

5.3 XPS high resolution energy scans of the samples on the (a) Ti 2p, (b) O 1s and (c) C 1s regions. The colored curves represent how the main peaks are deconvolved. . . . . . 45
5.4 Schematic layout of the beamline and its optics [21] . . . . . 47
5.5 Measurement process at BEAR. Acquisition of (a)the direct beam and its background and (b) the reflected beam and its background. . . . . . 49
5.6 Schematic of a multilayer structure of N layers, where the ith layer has thickness $d_i$ , interfacial roughness/diffuseness $\sigma_i$, and index of refraction $\mathbf{n}_i$. . . . . . 50
5.7 Reflectance measurement of sample Eb2 at E=310 eV with curve fittings considering a one-layer ($TiO_2$/Si), a two-layer ($TiO_2$/$SiO_2$/Si) and a three-layer model (C/$TiO_2$/$SiO_2$/Si). In the inset, the grazing angle range 8-14$^o$ is enhanced. . . . . . 52
5.8 Reflectance measurement of sample Eb2 at E=612 eV with curve fittings considering a one-layer ($TiO_2$/Si), a two-layer ($TiO_2$/$SiO_2$/Si) and a three-layer model (C/$TiO_2$/$SiO_2$/Si). In the inset, the grazing angle range 8-14$^o$ is enhanced. . . . . . 52
5.9 Schematic of the three-layer optical model (not in scale). . . . . . 53
5.10 Reflectance curves (dotted lines) measured at energies E=248 eV, 310 eV and 397.3eV, and their respective best fit curves (continuous lines) for sample Eb2. . . . . . 54
5.11 Reflectance curves (dotted lines) measured at energies E=34 eV, 41.75 eV, 55.1 eV and 82.5eV, and their respective best fit curves (continuous lines) for sample Eb3. . . . . . 55
5.12 $TiO_2$ measured values of $\beta$ versus photon energy (dots) along with values from CXRO [65] (continuous line). . . . . . 56
5.13 Close up of the Ti L edge zone. $TiO_2$ measured values of $\beta$ versus photon energy (dots) along with values from CXRO [65](continuous line). . . . . 56
5.14 $TiO_2$ measured values of $\delta$ versus photon energy (dots) along with values from CXRO [65] (continuous line). . . . . . 57
5.15 Close up of the Ti L edge zone. $TiO_2$ measured values of $\delta$ versus photon energy (dots) along with values from CXRO [65] (continuous line). . . . 57
5.16 Calculated reflectance curves for s-polarized radiation. The grazing angle $\theta$ is normalized to the critical angle $\theta_C$ [66]. . . . . . 58
5.17 Schematic of the optical model introducing interlayers at the interfaces (not in scale). . . . . . 60
5.18 Fits of reflectance profile measured at E=454.2 eV (dotted line), without including interlayers into the optical model (dashed line), and the optimization achieved inserting interlayers in the optical model (continues line). For (a) sample Eb1, (b) sample Eb2 and (c) sample Eb3. . . . . . 62

6.1 LPP generated in our experimental chamber as the light source for the reflectometer. . . . . . 66
6.2 Schematic of an electron density gradient of a laser-produced plasma [1]. 67
6.3 Geometry of the diffraction by (a) a plane reflection grating and (b) a plane transmission grating [73]. . . . . . 69
6.4 Geometry of the diffraction and path difference for planar wavefronts [73]. 70
6.5 Schematic of two slightly different wavelengths dispersed by the grating [74]. . . . . . 71
6.6 Schematic diagram of the experimental set-up of the reflectometer. (a) Lateral and (b) Top view. . . . . . 73
6.7 Inside view of the experimental chamber of the soft X-ray reflectometer at UCD. . . . . . 75
6.8 Experimental chamber of the soft X-ray reflectometer at UCD. . . . . . 75
6.9 Measurement acquisition image. Straight through and reflected spectrum of an RBSN source target. . . . . . 76
6.10 Attenuation length (1/e drop off)of several materials showing the absorption edges in the Soft X-rays spectral range. . . . . . 78
6.11 Plot of the known wavelength values of a RBSN source as a function of the pixel assigned, and its linear fit. . . . . . 79
6.12 Plot of the difference between the known wavelengths and the best fit values as a function of pixel value. . . . . . 79
6.13 Schematic diagram with dimensions and dispositions of the set up (not in scale). . . . . . 80
6.14 Background noise prior to insertion of the baffles in the reflectometer. The noise presents a spatial structure of variable intensity as an inherent response of the CCD to the scattered IR radiation. . . . . . 83
6.15 Direct unreflected spectra from different target materials. . . . . . 85
6.15 Direct unreflected spectra from different target materials (cont.) . . . . . 86
6.16 (a) AFM measurement of the step hight between the substrate original surface and the capping layer after debris exposure. (b) Profile of the step across the green line. . . . . . 87
6.17 (a)Reflectance measurements during debris exposure.(b) Ti edge close up. 88
6.18 Set-up to mitigate debris, (a) without shield (i.e.original set-up) (b) with the shield incorporated and (c) with the shield and a set of neodymium permanent magnets in place. . . . . . 90
6.19 Reflectance results taken every 3000 shots at 550 mJ each, (a) with the original setup (absence of shield and magnets), (b) in the presence of the baffle shield and (c) in the presence of both shield and set of neodymium permanent magnets. . . . . . 92

6.20 (a)Straight through and (b)Reflected beam intensity spectra drop off due to optics contamination after each cycle of 3000 shots at 550 mJ/shot on Ti target. Reflectance source target: W. . . . . . 94
6.21 (a)Straight through and (b)Reflected beam intensity drop off tendency due to optics contamination after each cycle of 3000 shots at 550 mJ/shot on Ti target. All curves are normalised to the highest point. Reflectance source target: W. . . . . . 95
6.22 (a) Photograph of the masked sample and (b) its extracted profile. . . . . 96
6.23 Schematic of the experiment to determine spatial resolution. . . . . . . . 97
6.24 (a) Image obtained with the spectral reflectometer of the masked sample. (b) Extracted vertical profile of the reflected light (top section of image (a)). 98
6.25 Profile obtained from the image of the sample overlapped with the vertical profile of the reflected light on the spectrum image. . . . . . 99
6.26 reflectance measurement of the masked sample. Showing the C absorption edge. . . . . . 100
6.27 Reflectance of sample M1 measured at ELETTRA synchrotron and with our reflectometer. . . . . . 101
6.28 Reflectance of sample M1 measured at different incident angles. IMD simulation is calculated at $2^{\circ}$ grazing incidence angle. . . . . . 102
6.29 The angular dependence of the absorption edge "depth" for the different elements in the layers of the sample. Values are normalised with respect to edge of C at $2^{\circ}$ grazing incidence angle. . . . . . 103
6.30 Reflectance of sample M2 and IMD simulation at $2^{o}$ grazing incidence angle. . . . . . 104
6.31 Reflectance of sample M2 making a position raster with a size step of 1 mm. . . . . . 105
6.32 Reflectance of sample M3 and IMD simulation at a $2^{o}$ grazing incidence angle. . . . . . 106
6.33 reflectance of sample M3 and M2. . . . . . 107
6.34 Reflectance of sample M4 and IMD simulation at a $2^{o}$ grazing incidence angle. . . . . . 107
6.35 Reflectance of sample M5 and IMD simulation at a $2^{o}$ grazing incidence angle. . . . . . 108
6.36 Reflectance of sample M5. . . . . . 109
6.37 Reflectance of sample M6 and IMD simulation at a $2^{o}$ grazing incidence angle. . . . . . 110

## List of Tables

3.1 Schematic of the Ti/Cr/Si bilayer samples structure . . . . . . . . . . . . . 28
3.2 Schematic of the $TiO_2$/Sc/Si bilayer samples structure . . . . . . . . . . . . 29

5.1 Film thickness and surface roughness values (SE=Spectroscopic Ellipsometry). . . . . . . . . . . . . . . . . . . . . . . . . . . . . . . . . . . . . 43
5.2 Optical constants of $TiO_2$ derived from reflectance-vs-angle measurements, along with values computed from atomic scattering factors assuming the films density . . . . . . . . . . . . . . . . . . . . . . . . . . . 59

6.1 Theoretical and experimental spectral resolution of our reflectometer for different wavelengths . . . . . . . . . . . . . . . . . . . . . . . . . . . 82

# Bibliography


[1] David Attwood. *Soft x-rays and extreme ultraviolet radiation: principles and applications*. Cambridge university press, 2007.

[2] Zdenek Knittl. *Optics of thin films: an optical multilayer theory*. Wiley, London, 1976.

[3] K. Seshan. *Handbook of Thin Film Deposition Processes and Techniques*. Materials Science and Process Technology. Elsevier Science, 2001.

[4] A. Piegari and F. Flory. *Optical Thin Films and Coatings: From Materials to Applications*. Woodhead Publishing Series in Electronic and Optical Materials. Elsevier Science, 2013.

[5] M.J.H. Kessels. *Soft X-ray multilayers mirrors*. PhD Thesis - University of Twente, Enschede, 1997.

[6] Naureen Ghafoor. *Multilayer X-ray mirrors*. 2008.

[7] G.P. Gallerano. The free electron laser: state of the art, developments and applications. *Nuclear Instruments and Methods in Physics Research Section A: Accelerators, Spectrometers, Detectors and Associated Equipment*, 340(1):11 – 16, 1994.

[8] G. A. Johansson, A. Holmberg, H. M. Hertz, and M. Berglund. Design and performance of a laser-plasma-based compact soft x-ray microscope. *Review of Scientific Instruments*, 73(3):1193–1197, 2002.

[9] Yoshiaki Horikawa, Koumei Nagai, and Yoshinori Iketaki. Soft x-ray reflectometry with a laser-produced plasma source. *Optical Engineering*, 33(5):1721—1725, 1994.

[10] K. Nakajima. Compact x-ray sources: Towards a table-top free-electron laser". *Nature Phys.*, 4(92), 2008.

[11] M. Peuker T. Wilhein H.M. Hertz M. Berglund, L. Rymell. Compact water-windows transmission x-ray microscopy. *J. of Mic.*, 197(286), 2000.

[12] C. Jian-Lin J. Chun-Shui, W. Zhang-Shan. Soft x-ray projection lithography technology. *High power laser and particle beams*, 12(559), 2000.

[13] Sertsu Mewael Giday. *PhD Thesis*. University of Padova, 2016.

[14] M.J.H. Kessels. *Interfaces in Soft X-ray multilayers mirrors*. PhD Thesis - University of Twente, Enschede, 1997.

[15] BJÖRN GÅLNANDER. *Thin Films and Deposition Processes Studied by Soft X-Ray Spectroscopy*. PhD Thesis - Universitatis Upsaliensis Uppsala, 2001., 2001.

[16] Saša Bajt, N.V. Edwards, and Theodore E. Madey. Properties of ultrathin films appropriate for optics capping layers exposed to high energy photon irradiation. *Surface Science Reports*, 63(2):73 – 99, 2008.

[17] Nadir S. Faradzhev, Boris V. Yakshinskiy, Elena Starodub, Theodore E. Madey, Shannon B. Hill, Steven Grantham, Thomas B. Lucatorto, Sergiy Yulin, Elio Vescovo, and Jeffrey W. Keister. Resonance effects in photoemission from tio2-capped mo/si multilayer mirrors for extreme ultraviolet applications. *Journal of Applied Physics*, 109(8), 2011.

[18] Y. Tanaka H. Kumagai-M. Chigane Y. Sanjo, M. Murata. Tio2/sapphire beam splitter for high-order harmonics. *Journal of Laser Micro/Nanoengineering*, 7(3):375–79, 2012.

[19] Hiroshi Kumagai, Koichi Toyoda, Katsutaro Kobayashi, Minoru Obara, and Yasuhiro Iimura. Titanium oxide/aluminum oxide multilayer reflectors for "water-window" wavelengths. *Applied Physics Letters*, 70(18), 1997.

[20] H Kumagai, Y Tanaka, Mm Murata, Y Masuda, and T Shinagawa. Novel tio2/zno multilayer mirrors at 'water-window'wavelengths fabricated by atomic layer epitaxy. *Journal of Physics: Condensed Matter*, 22(47):474008, 2010.

[21] ELETTRA Synchrotron. https://www.elettra.trieste.it/lightsources/elettra/elettra-beamlines/bear/beamline-description.html. 2016.

[22] Alexander Guggenmos, Stefan Radünz, Roman Rauhut, Michael Hofstetter, Sriram Venkatesan, Angela Wochnik, Eric M. Gullikson, Stefan Fischer, Bert Nickel, Christina Scheu, and Ulf Kleineberg. Ion polished cr/sc attosecond multilayer mirrors for high water window reflectivity. *Opt. Express*, 22(22):26526–26536, Nov 2014.

[23] Tadashi Hatano, Takeo Ejima, and Toshihide Tsuru. Cr/sc/mo multilayer for condenser optics in water window microscopes. *Journal of Electron Spectroscopy and Related Phenomena*, pages –, 2017.

[24] Regina Soufli. *Optical constants of materials in the EUV / soft x-ray region for multilayer mirror applications*. University of California at Berkeley, 1997.

[25] G.F. Knoll. *Radiation Detection and Measurement*. Wiley, New York, 2000, Third Edition.

[26] Mónica Fernández Perea. *Búsqueda y caracterización de nuevos materiales y su aplicación en recubrimientos ópticos para el FUV y EUV*. Universidad Complutense de Madrid, 2009.

[27] M Born and E Wolf. *Principles of Optics*. Cambridge University Press, 7 edition, 1999.

[28] P. Debye. Interferenz von röntgenstrahlen und wärmebewegung. *Annalen der Physik*, 348(1):49–92, 1913.

[29] Ivar Waller. Zur frage der einwirkung der wärmebewegung auf die interferenz von röntgenstrahlen. *Zeitschrift für Physik*, 17(1):398–408, 1923.

[30] L Nevot and P Croce. Caractérisation des surfaces par réflexion rasante de rayons x. application à l'étude du polissage de quelques verres silicates. *Revue de Physique appliquée*, 15(3):761–779, 1980.

[31] David L Windt. Imd—software for modeling the optical properties of multilayer films. *Computers in physics*, 12(4):360–370, 1998.

[32] P. Baumeister. *Optical Coating Technology*. SPIE Press monograph. SPIE Press, 2004.

[33] M. Ohring. *The Materials Science of Thin Films*. Referex Engineering. Academic Press, 1992.

[34] L. Holland. *Vacuum deposition of thin films*. Wiley, 1966.

[35] Wikipedia, the free encyclopedia. https://en.wikipedia.org/wiki/file:electron_beam_deposition_001.jpg. 2012.

[36] J. George. *Preparation of Thin Films*. Taylor & Francis, 1992.

[37] *IONVAC e-beam and Joule evaporation system, User's guide*. UNIPD, 2012.

[38] M. Zambolin. *Deposizione e Caratterizzazione di Film Sottili Realizzati via E-Beam Evaporation*. UNIPD, 2012.

[39] *INFICON Operating Manual - XTM2 Deposition Monitor*. INFICON, 2001.

[40] *KLA Tencor P-16+ Profilometer, User's guide*. 2009.

[41] Enric Garcia-Caurel, Antonello De Martino, Jean-Paul Gaston, and Li Yan. Application of spectroscopic ellipsometry and mueller ellipsometry to optical characterization. *Applied spectroscopy*, 67(1):1–21, 2013.

[42] H. Fujiwara. *Spectroscopic Ellipsometry: Principles and Applications*. Wiley, 2007.

[43] J. A. Woollam Co. https://www.jawoollam.com/wp-content/uploads/rae-ellipsometry-tutorial-button1.png. 2016.

[44] Inc J. A. Woollam Co. *Guide to Using WVASE Spectroscopic Ellipsometry Data Acquisition and Analysis Software*. 2012.

[45] PSIA Corp. *XE-100 High accuracy small sample SPM - User's Manual*. 2002.

[46] P.E.J. Flewitt and R.K. Wild. *Physical Methods for Materials Characterisation*. Graduate student series in materials science and engineering. Institute of Physics Pub., 1994.

[47] J.F. Watts and J. Wolstenholme. *An Introduction to Surface Analysis by XPS and AES*. Wiley, 2003.

[48] D. Briggs and J.T. Grant. *Surface Analysis by Auger and X-ray Photoelectron Spectroscopy*. SurfaceSpectra, 2003.

[49] E. Spiller. *Soft X-ray Optics*. SPIE Press monograph. SPIE Optical Engineering Press, 1994.

[50] B.L. Henke, E.M. Gullikson, and J.C. Davis. X-ray interactions: Photoabsorption, scattering, transmission, and reflection at e = 50-30,000 ev, z = 1-92. *Atomic Data and Nuclear Data Tables*, 54(2):181 – 342, 1993.

[51] Regina Soufli, Andrew L. Aquila, Farhad Salmassi, Mónica Fernández-Perea, and Eric M. Gullikson. Optical constants of magnetron-sputtered boron carbide thin films from photoabsorption data in the range 30 to 770 ev. *Appl. Opt.*, 47(25):4633–4639, Sep 2008.

[52] Amol Singh, Mohammed H. Modi, and G. S. Lodha. Optical properties of zirconium carbide in 60–200  Å wavelength region using x-ray reflectivity technique. *Appl. Opt.*, 54(2):253–258, Jan 2015.

[53] Edward D Palik. *Handbook of optical constants of solids*, volume 3. Academic press, 1998.

[54] PN Rao, Mohammed H Modi, and GS Lodha. Optical properties of indium phosphide in the 50–200 wavelength region using a reflectivity technique. *Applied optics*, 49(28):5378–5383, 2010.

[55] D. L. Windt. *IMD, Version 5, Installation and User's Manual*. 2013.

[56] Mohamed N Ghazzal, N Chaoui, Michel Genet, Eric M Gaigneaux, and D Robert. Effect of compressive stress inducing a band gap narrowing on the photoinduced activities of sol–gel tio 2 films. *Thin Solid Films*, 520(3):1147–1154, 2011.

[57] Yueming Li, Zhiguang Wang, and Xiao-Jun Lv. N-doped tio 2 nanotubes/n-doped graphene nanosheets composites as high performance anode materials in lithium-ion battery. *Journal of Materials Chemistry A*, 2(37):15473–15479, 2014.

[58] Zhang Sam Huang Weimin Fu Yongqing ., Du Hejun. Xps characterization of surface and interfacial structure of sputtered tini films on si substrate. *Materials Science and Engineering A, Structural Materials: Properties, Microstructure and Processing*, 403(1-2):25–35, 2005.

[59] Mohamed N Ghazzal, Robert Wojcieszak, Gijo Raj, and Eric M Gaigneaux. Study of mesoporous cds-quantum-dot-sensitized tio2 films by using x-ray photoelectron spectroscopy and afm. *Beilstein journal of nanotechnology*, 5(1):68–76, 2014.

[60] A Comisso, A Giglia, M Nardello, E Tessarolo, L Calvillo, MG Sertsu, G Granozzi, F Gerlin, L Brigo, and P Nicolosi. Characterization of tio2 thin films in the euv and soft x-ray region. In *SPIE Optics+ Optoelectronics*, pages 95100Z–95100Z. International Society for Optics and Photonics, 2015.

[61] S. Nannarone, F. Borgatti, A. DeLuisa, B. P. Doyle, G. C. Gazzadi, A. Giglia, P. Finetti, N. Mahne, L. Pasquali, M. Pedio, G. Selvaggi, G. Naletto, M. G. Pelizzo, and G. Tondello. The bear beamline at elettra. *AIP Conference Proceedings*, 705(1), 2004.

[62] J.D. Jackson. *Classical Electrodynamics*. Wiley, 1998.

[63] Elena O Filatova, Igor V Kozhevnikov, Andrey A Sokolov, Evgeniy V Ubyivovk, Sergey Yulin, Mihaela Gorgoi, and Franz Schäfers. Soft x-ray reflectometry, hard x-ray photoelectron spectroscopy and transmission electron microscopy investigations of the internal structure of tio2 (ti)/sio2/si stacks. *Science and Technology of Advanced Materials*, 2016.

[64] I. Diel, J. Friedrich, C. Kunz, S. Di Fonzo, B. R. Müller, and W. Jark. Optical constants of float glass, nickel, and carbon from soft-x-ray reflectivity measurements. *Appl. Opt.*, 36(25):6376–6382, Sep 1997.

[65] The Center for X-Ray Optics. http://www.cxro.lbl.gov/. 2010.

[66] Regina Soufli and Eric M. Gullikson. Reflectance measurements on clean surfaces for the determination of optical constants of silicon in the extreme ultraviolet–soft-x-ray region. *Appl. Opt.*, 36(22):5499–5507, Aug 1997.

[67] MG Sertsu, M Nardello, A Giglia, AJ Corso, C Maurizio, L Juschkin, and P Nicolosi. Analysis of buried interfaces in multilayer mirrors using grazing incidence extreme ultraviolet reflectometry near resonance edges. *Applied optics*, 54(35):10351–10358, 2015.

[68] MG Sertsu, A Giglia, S Brose, D Park, ZS Wang, J Mayer, L Juschkin, and P Nicolosi. Deposition and characterization of b4c/ceo2 multilayers at 6. x nm extreme ultraviolet wavelengths. *Journal of Applied Physics*, 119(9):095301, 2016.

[69] A. Sandell, M. P. Anderson, Y. Alfredsson, M. K.-J. Johansson, J. Schnadt, H. Rensmo, H. Siegbahn, and P. Uvdal. Titanium dioxide thin-film growth on silicon (111) by chemical vapor deposition of titanium(iv) isopropoxide. *Journal of Applied Physics*, 92(6), 2002.

[70] N Benito and C Palacio. Mixed ti–o–si oxide films formation by oxidation of titanium–silicon interfaces. *Applied Surface Science*, 301:436–441, 2014.

[71] Noelia Benito and Carlos Palacio. Growth of ti–o–si mixed oxides by reactive ion-beam mixing of ti/si interfaces. *Journal of Physics D: Applied Physics*, 47(1):015308, 2013.

[72] M. Berglund. *A Compact Soft X-ray Microscope Based on a Laser-Plasma Source, Ph.D. thesis*. Royal Institute of Technology (KTH), Stockholm, Sweden, 1999.

[73] Christopher A Palmer and Erwin G Loewen. *Diffraction grating handbook*. Newport Corporation Springfield, Ohio, USA, 2005.

[74] S. Mani Naidu. *Engineering Physics*. Dorling Kindersley (India) Pvt. Ltd., 2001.

[75] A. K. Gaigalas et al. Procedures for wavelength calibration and spectral response correction of ccd array spectrometers. *Journal of Research of the National Institute of Standards and Technology*, (114.4):215–218.

[76] NIST (US). http://physics.nist.gov/physrefdata/asd/lines$_{f}orm.html.2016.$

[77] Emma Sokell Tom McCormack Xinbing Wang Luning Liu, Padraig Dunne and Fergal O'Reilly. A simple technique for the measurement of laser propagation parameters. *Internal group research (not published) - Wuhan National Laboratory for Optoelectronics, Huazhong University of Science and Technology and School of Physics, University College Dublin*, 2016.

[78] Th Wilhein, S Rehbein, D Hambach, M Berglund, L Rymell, and HM Hertz. A slit grating spectrograph for quantitative soft x-ray spectroscopy. *Review of scientific instruments*, 70(3):1694–1699, 1999.

[79] S Sailaja, V Arora, S R Kumbhare, P A Naik, P D Gupta, D A Fedin, A A Rupasov, and A S Shikanov. A simple xuv transmission grating spectrograph with sub-ångström resolution for laser-plasma interaction studies. *Measurement Science and Technology*, 9(9):1462, 1998.

[80] J. M. Bridges, C. L. Cromer, and Thomas J. McIlrath. Investigation of a laser-produced plasma vuv light source. *Appl. Opt.*, 25(13):2208–2214, Jul 1986.

[81] S. S. Harilal, Beau O'Shay, and Mark S. Tillack. Debris mitigation in a laser-produced tin plume using a magnetic field. *Journal of Applied Physics*, 98(3):036102, 2005.

[82] H Lan, X B Wang, H Chen, D L Zuo, and P X Lu. Influence of a magnetic field on laser-produced sn plasma. *Plasma Sources Science and Technology*, 24(5):055012, 2015.

[83] S. S. Harilal, M. S. Tillack, B. O'Shay, C. V. Bindhu, and F. Najmabadi. Confinement and dynamics of laser-produced plasma expanding across a transverse magnetic field. *Phys. Rev. E*, 69:026413, Feb 2004.